MELT DETECTION AND ESTIMATION IN GREENLAND

USING TANDEM SEAWINDS AND QUIKSCAT

SCATTEROMETERS

by

Brandon R. Hicks

A thesis submitted to the faculty of

Brigham Young University

in partial fulfillment of the requirements for the degree of

Master of Science

Department of Electrical and Computer Engineering

Brigham Young University

August 2006

BRIGHAM YOUNG UNIVERSITY

GRADUATE COMMITTEE APPROVAL

of a thesis submitted by

Brandon R. Hicks

This thesis has been read by each member of the following graduate committee and by majority vote has been found to be satisfactory.

_____   _____
Date   David G. Long, Chair

_____   _____
Date   Karl F. Warnick

_____   _____
Date   Michael A. Jensen

ABSTRACT

MELT DETECTION AND ESTIMATION IN GREENLAND

USING TANDEM SEAWINDS AND QUIKSCAT SCATTEROMETERS

Brandon R. Hicks

Department of Electrical and Computer Engineering

Master of Science

Ku-band dual-polarization radar backscatter measurements from the SeaWinds on QuikScat (QuikScat) and SeaWinds on ADEOS-2 (SeaWinds) scatterometers are used to classify the melt state and estimate melt severity in Greenland. Backscatter measurements are organized into high temporal and high spatial resolution images created using the Scatterometer Image Reconstruction (SIR) algorithm and a new temporal data segmentation technique. Melt detection is performed using a layered electromagnetic model combined with a Markov chain model. The new melt detection method allows classification of the snow-pack into three states: melt, refreeze, and frozen. Melt severity and refreeze severity indexes are also developed.

The melt detection methods developed in this thesis are verified by using a one-dimensional geophysical/electromagnetic model simulation of the snow-pack under melting conditions and by comparison with *in situ* weather station data at the ETH Camp in western Greenland. The diurnal cycle of backscatter measurements is also analyzed at this location. The melt detection and estimation method is applied to the entire Greenland ice-sheet. The resulting melt classifications and melt severity indexes are used to generate a number of maps outlining the features of the 2003 melt season. Good agreement of the melt severity and a 1978 SASS Greenland ice facies map is observed.

ACKNOWLEDGMENTS

Contents

List of Tables

List of Figures

xi

Chapter 1

Introduction

The Greenland ice-sheet profoundly influences Earth's climate. Greenland, the largest island on the planet, is approximately 81% covered by ice. Greenland's ice-sheet accounts for approximately 8% of Earth's ice volume, and 11% of the Earth's fresh water. Many of our planet's climatic elements, including the radiation budget and sea level, are strongly influenced by changes in this island's ice-sheet.

Recent global trends have raised concerns of global warming and climate change. Global warming is threatening to raise ocean levels and change climates world-wide. Understanding changes in Greenland's ice-sheet is critical to understanding these climatic trends. An estimated 7% of the current rise in sea level can be attributed to increased ablation of the Greenland ice-sheet [1]. The planet's solar radiation budget is also directly affected by the Greenland ice-sheet. Because the surface albedo of the Greenland ice-sheet is strongly affected by the liquid water content in the snow—nearly 45% more incoming solar radiation is absorbed by wet snow than dry snow [2]—understanding the processes that drive melt in Greenland is becoming increasingly important. Higher temperatures in Greenland cause increased duration and areal extent of the melt season, increasing the amount of the Sun's radiation that is absorbed, which in turn increases temperatures and melt. This positive feedback mechanism makes Greenland sensitive to subtle climate changes and an early indicator of greater global climate change.

Unfortunately, Greenland's harsh environment and remote location make reliable measurements of Greenland's ice-sheet difficult. Even as interest in understanding Greenland's ice-sheet increases, the ability to collect data remains limited. Only

several weather stations are in operation, and the data they collect is limited, leaving a vast expanse of ice and snow where there is no consistent reliable information. Indeed, many areas of Greenland have never been physically visited, let alone measured for factors influencing local and global climates.

Until the past few decades, the only way to collect the valuable information needed to detect climate change in Greenland was to directly record the weather and collect samples of the ice-sheet. Fortunately, the launching of the first satellites ushered in a new era where the remote measuring of physical parameters from space is possible. Particularly, microwave-sensor bearing satellites in polar orbits have made possible the measuring of important parameters affecting the climate of the Greenland ice-sheet.

Microwave sensors, with wavelengths much longer than their optical and infrared counterparts, are capable of penetrating cloud, rain, and snow. These sensors observe the Earth's surface, without regard for time of day or prevailing atmospheric weather conditions. Moreover, these longer microwave sensor wavelengths facilitate the detection of minute amounts of liquid water in snow, making these sensors crucial to the measurement of Greenland's ice-sheet and other facets of Earth's climate.

There are two primary types of microwave sensors: scatterometers and radiometers. Scatterometers, active radar systems, send energy pulses to desired targets and measure the reflected power. Radiometers are passive systems that measure the microwave emissions detected by the sensor. Both active and passive sensors provide information about the surface, although the mechanism by which they measure is quite different. Both microwave radiometers [3, 4, 5] and scatterometers [6, 7, 8, 9], have been widely used in studies of the Greenland ice-sheet. Areas studied using microwave instruments include accumulation [4, 8, 9] and melt detection [3, 10, 11, 12, 13] among others.

While many melt detection studies of Greenland's ice sheet have used active and passive microwave sensors, these studies have focused on limited aspects of melt detection. Previous studies have focused on whether or not liquid water is present as the primary melt detection methodology. Other melt factors, e.g. the amount or

2

vertical distribution of melt, have not been considered. For the first time, this thesis uses scatterometery to estimate melt severity and melt refreeze, adding significantly to the understanding of melt processes in Greenland.

This thesis studies a new method of using active microwave scatterometer data to classify the snow-pack in three possible states: frozen, melting and refreezing. The method described in this thesis combines a parameterized layered melt model with a one-step Markov state detection model to classify the ice in these three possible states. This method also estimates the severity of melt and refreeze by estimating the parameters that are used to discern each state. Data collected by the tandem mission of QuikSCAT and SeaWinds are utilized in this new melt detection and estimation method.

The new melt detection and estimation method is made possible by the development of a new method of processing the tandem mission data into images. While polar images with temporal sampling frequencies higher than one sample per day have been previously attempted, the resulting ascending/descending imageset suffers from poor temporal resolution due to complications arising from the measurement geometry of these satellites. The new processing method uses the time-of-day of individual measurements to separate the backscatter data into images, greatly improving the temporal sampling of the polar regions. The processing of backscatter data into images is performed using the Scatterometer Image Reconstruction (SIR) algorithm, resulting in an imageset with high temporal as well as high spatial resolution. This new processing method results in three nearly uniformly spaced temporal samples per day when applied to tandem SeaWinds and QuikSCAT mission data, providing the ability to resolve the diurnal cycle.

The new melt detection and estimation method is tested using a one-dimensional model of the snow-pack and verified using *in situ* automatic weather station (AWS) data. Validated at the location of AWS data, the melt detection and estimation method provides seasonal estimates of melt onset, refreeze onset, melt season length, and seasonal melt severity across the ice sheet.

3

The organization of this thesis is as follows. Chapter 2 provides background information concerning the study of Greenland's ice-sheet and the theory of radiation transfer and scatterometery as it is applied to the ice sheet. Chapter 3 discusses the new processing method and the temporal sampling of the QuikSCAT and SeaWinds in the polar regions. This chapter also includes background on the QuikSCAT and SeaWinds satellites and the SIR algorithm. Chapter 4 describes the theory and application of the new melt detection and estimation method. Chapter 5 analyzes the application of this new melt detection and estimation method on the Greenland ice-sheet. Chapter 6 concludes, giving summary of the results obtained, contributions made, and directions for further research. Finally, the Appendix contains some extended information regarding the application of the methods described in this thesis.

Chapter 2

Background

This chapter contains background information useful for understanding the research described by this thesis. First, this chapter provides background information concerning the Greenland ice sheet. Then, this chapter gives a brief introduction to scatterometery and remote sensing. Last, this chapter discusses radiation transfer theory. Chapter 3 provides additional background on the tandem QuikSCAT/SeaWinds mission and the data obtained by these satellites.

2.1   Greenland Ice Sheet

The Greenland ice sheet is the second largest glacier on the planet, covering 1,755,637 km^2. With an average depth of over 1.5 km, the Greenland ice sheet constitutes a massive volume of glacial ice. Though the ice-sheet varies in thickness from the outer edge to the interior, Greenland's ice-sheet is relatively flat—most of the ice sheet surface is between 2000m and 3000m in elevation. The highest point of the ice sheet, located in Eastern Greenland, reaches 3278 m above sea level. A separate summit of 2850 m is located in the Southern part of the island. The gently increasing slope causes average air temperatures to drop toward the interior of the island; however, the temperatures drop very gradually. The gradual change in temperature with the slope makes the ice sheet very sensitive to changing melt conditions.

While sensitivity of Greenland to changing climatic conditions makes the study of this island's glacial ice sheet of utmost importance, the cost and difficulty of collecting *in situ* data makes this type of data scarce compared to the size of the ice

sheet. Though further exploration of Greenland is possible with the help of modern technology, extensive measurements of the ice sheet are still economically and logistically infeasible. Fortunately, the sensitivity of microwave sensors to parameters related to the growth and ablation of the ice sheet makes remote sensing of the island an attractive way to study the large scale climatic changes that affect this ice sheet.

Perhaps the most extensive study of the Greenland ice sheet was performed from 1952 to 1955 by the United States SIPRE project [15]. This study includes extensive snow pit data, giving insight into the accumulation and melt processes that occur in the ice sheet. The data is still commonly used today to further understand the ice sheet's properties. In Benson's report [15] for the SIPRE project, a number of different ice facies are identified. Benson described four ice facies critical to the understanding Greenland's ice-sheet, including ablation facies, soaked or wet snow facies, percolation facies, and dry snow facies.

Ablation facies – The area near the edge of the ice sheet where the snow accumulated during the previous year is completely melted away, exposing glacial ice beneath.

Soaked or wet snow facies – The areas further upslope from the ablation facies, where the snow accumulated during the past year is not completely melted away, but becomes completely saturated with melt water before refreezing. The wet snow facies are separated from the ablation facies by a boundary termed the *firn line.*

Percolation facies – The area where some melting occurs, but the snow accumulated during the previous year does not become completely saturated with melt water. The percolation facies are delineated from the wet snow facies by the boundary termed the *saturation line.*

Dry snow facies – The area in the interior of the ice sheet high enough that the temperatures do not allow significant summer melt to occur. The line separating the percolation facies and the dry snow facies is termed the *dry snow line.*

6

The location of the ice facies according to Benson's study is shown in Figure 2.1.

Since the SIPRE project, many other studies have been completed, which add understanding to the nature of the ice sheet, the location of the ice facies, and the amount of annual accumulation [2, 4, 6, 8, 9, 16, 17, 18, 19]. Long and Drinkwater [6] used σ^o measurements from the Seasat-A Scatterometer (SASS) satellite to map the Greenland snow zones, based on a physical scattering model. The resulting SASS map of the Greenland ice-sheet, created of data from July to October of 1978, marks the first facies map generated from remote sensing data, and is of particular interest because, like SeaWinds and QuikSCAT, SASS is a Ku-Band scatterometer. The SASS map is shown in Figure 2.2. Others have used SAR measurements to map σ^o to the ice facies [19, 20, 21]. Accumulation estimates have been made by both active [8, 9, 22] and passive [4] microwave instruments.

Ablation and melt are also commonly studied using microwave instruments. To detect melt, Abdalati and Steffen used a threshold on the normalized difference between the 37 GHz vertical channel and 37 GHz horizontal channel of brightness temperature data collected by the SSM/I radiometer [2, 3, 18]. Simple data thresholding has been widely used as a method of detecting melt using scatterometers as well [11, 13]. More complex thresholding schemes using multiple sensors have also been used with some success [25, 26]. Diurnal variation of backscatter has been shown to also correlate with melt [10]. The separation of melt from refreeze, which is important to ablation has been suggested by Ashcraft and Long [12]. This thesis adds to the work previously performed by creating a working detection model that separates melt from refreeze and estimates melt and refreeze severity using backscatter data.

2.2 Scatterometery

The basis of scatterometry is in the radar equation,

$$P_r = \frac{P_t G}{4\pi R^2} \sigma \frac{1}{4\pi R^2} \frac{\lambda^2 G}{4\pi}, \tag{2.1}$$

where $\frac{P_t G}{4\pi R^2}$ is the power density incident on the target, $\frac{1}{4\pi R^2}$ is the spreading loss to/from the target, $\frac{\lambda^2 G}{4\pi}$ is the effective area of the receiver, σ is the effective size of
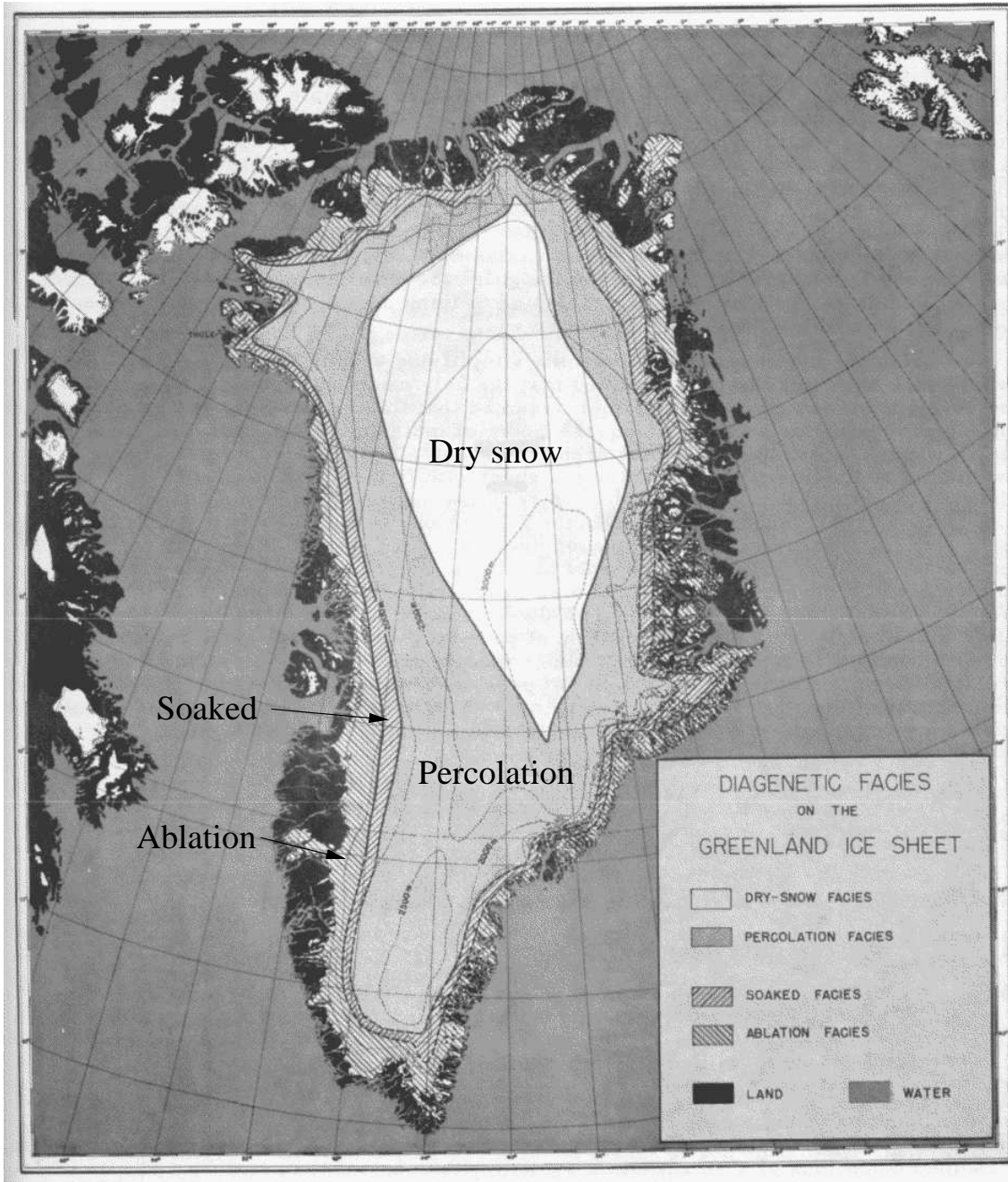
Figure 2.1: The Benson ice facie map [15].
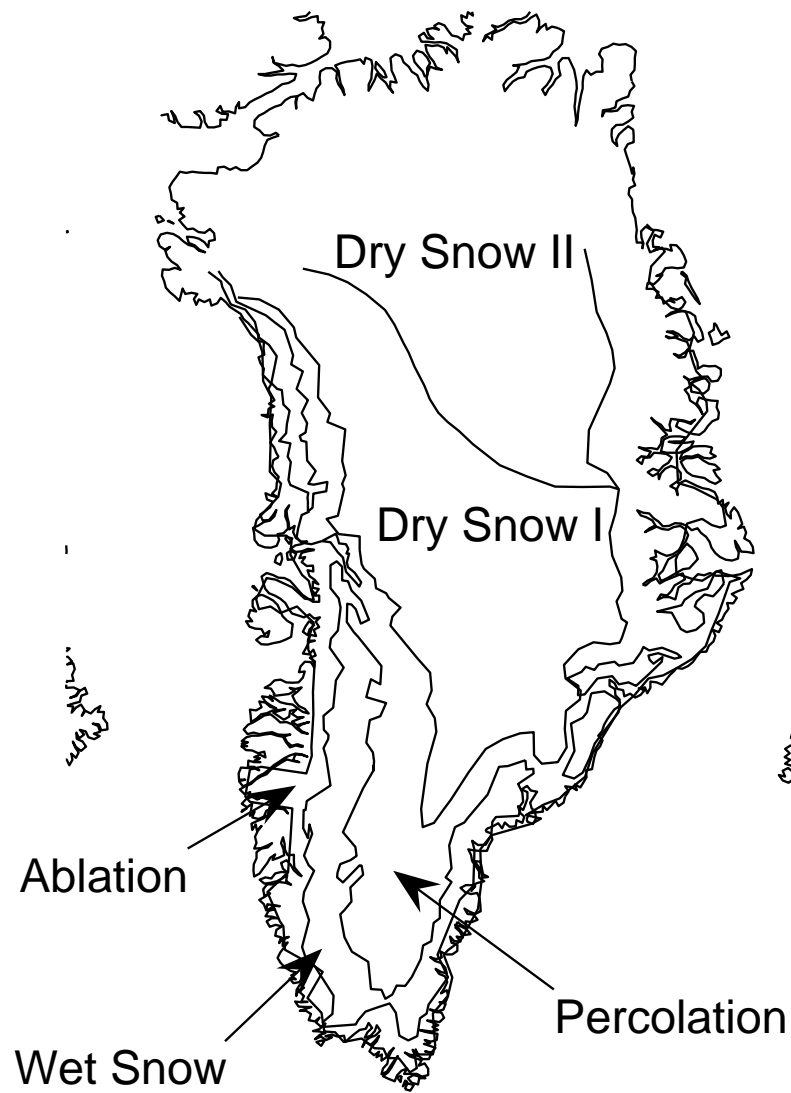
Figure 2.2: The 1978 SASS derived ice facie map (Long and Drinkwater) [6]. Two areas of dry snow are distinguished by annual accumulation. The dry snow I region receives more accumulation than the dry snow II region.

the target, G is the gain of the antenna in the direction of the target, P_t is the power transmitted, R is the distance from the transmitter/receiver to the target, and λ the wavelength of the scattered pulse. In scatterometery, all the parameters except σ are known to the receiver. A scatterometer sends a pulse to the target and measures the return power. Since all the parameters are known except the target's backscatter, the scatterometer essentially measures the effective target size, σ, called the radar cross-section. The normalized radar cross-section, σ^o, is the cross section normalized to the actual area of the target,

$$\sigma^o = \frac{\sigma}{A_t}. \tag{2.2}$$

For distributed targets, the area of the target is effectively the area of the antenna footprint. Thus in remote sensing, the power measured by the scatterometer can be translated to σ^o, telling how effectively the ground reflects the incident pulse back to the radar.

Measurements of σ^o depend on both the physical properties such as shape, roughness and orientation, as well as electrical properties such as dialectic constant and conductivity of the target. Variations in the roughness of the surface, for example, can change the amount of energy reflected back to the radar, as can changes in the dielectric constant. Because the measurements are affected by both physical and electrical target properties, the measured backscatter depends on both the incidence and azimuth angles of the scatterometer relative to the target.

Figure 2.3 illustrates the basic mechanisms that affect the backscatter return: surface scattering, volume scattering, and absorption. One way to analyze the backscatter is to look at individual scatterers. A scatterer can transmit or reflect the incident radar pulse in any number of directions depending on its orientation, as well as absorb a portion of the radar pulse. Unfortunately, when the number of scatterers becomes large the complexity of determining the backscattered return becomes intractable. The interaction of the incident pulse with all the scatterers—the coherent scattering and absorbing of the pulse—is quite complicated. Since the number of individual scatterers in the field of a scatterometer is very large, analyzing the

10

backscatter of the combined return from all the scatterers is intractable. Fortunately, there are methods of dealing with targets consisting of a large number of scatterers statistically. In conditions where volume scattering dominates the return signal, radiation transfer theory can be used.
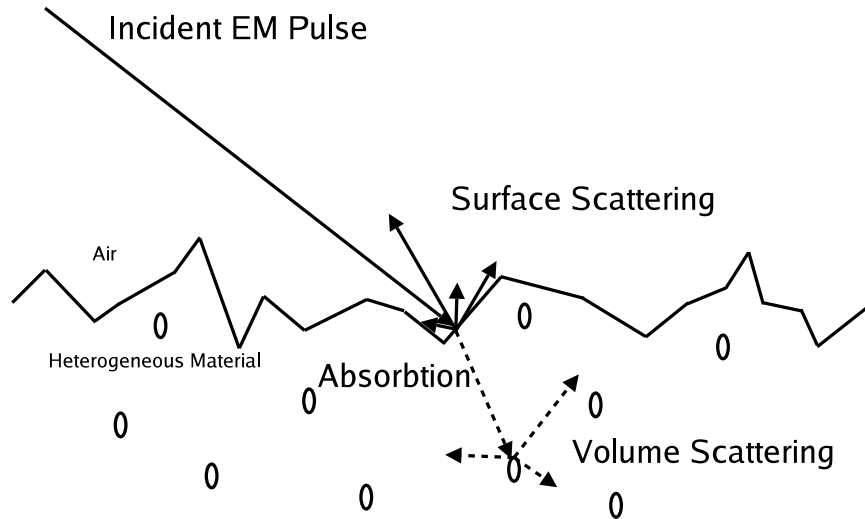
Figure 2.3: Diagram illustrating the scattering of an incident electromagnetic pulse. The scattering depends on the incidence and azimuth angles as well as the surface roughness, and material composition.

Many regions of the snow-pack in Greenland are well modeled by volume scattering, and hence by radiation transfer theory, which is explained later. Snow consists mostly of air and water in both solid and liquid forms. The effective dielectric constant of snow and firn is roughly 1.3–2.0. This low dialectic constant viewed from the incidence angles where QuikSCAT and SeaWinds measure backscatter, combined with the relative smoothness of the snow-air surface, makes the surface contribution to backscatter very small. On the other hand, the snow itself is heterogeneous—distinct snow grains are surrounded by air and/or liquid water—which results in significant volume scattering of the incident radar pulse. Thus, Greenland snow is primarily a volume scattering medium. Moreover, the addition of liquid water content as melt

occurs, increases the imaginary part of the dielectric constant dramatically, increasing absorption loss. The application of radiation transfer theory to the Greenland snow-pack is therefore a useful tool in understanding the mechanisms that affect the radar cross-section of the snow.

2.3   Radiation Transfer

In radiation transfer theory, radiation transfered through a material is continuously absorbed and scattered by the material. This attenuation is obtained by solving a simple linear differential equation, known as the equation of transfer. Consider a small cylinder (see Figure 2.4) with volume $\mathrm{d}V$. Radiated power, P, is incident normally on the face of the cylinder. The radiation lost in the process of being transfered through this infinitesimal volume is,

$$\mathrm{d}P = -\kappa_e P \mathrm{d}z, \tag{2.3}$$

where κ_e is the coefficient of extinction and z is the direction of incident radiation. The extinction coefficient, which describes the rate of radiation power loss, is the sum of absorption described by the absorption coefficient, κ_a, and scattering described by the scattering coefficient, κ_s,

$$\kappa_e = \kappa_a + \kappa_s. \tag{2.4}$$

Letting $\mathrm{d}\tau = \kappa_e \mathrm{d}z$, where τ is called the optical depth. Thus, Equation 2.3 becomes

$$\frac{\mathrm{d}P}{\mathrm{d}\tau} + P = 0, \tag{2.5}$$

which is the transfer equation. Radiation transfer theory, which is traditionally used for both extinction and emission, usually includes a source term on the right-hand side of Equation 2.5. However, for scatterometry this source term is small enough to be considered negligible. Solving Equation 2.5 for P, the power transmitted through the material from depth z_1 to z_2 becomes,

$$P(z_2) = P(z_1)e^{-\tau(z_1, z_2)}, \tag{2.6}$$

12
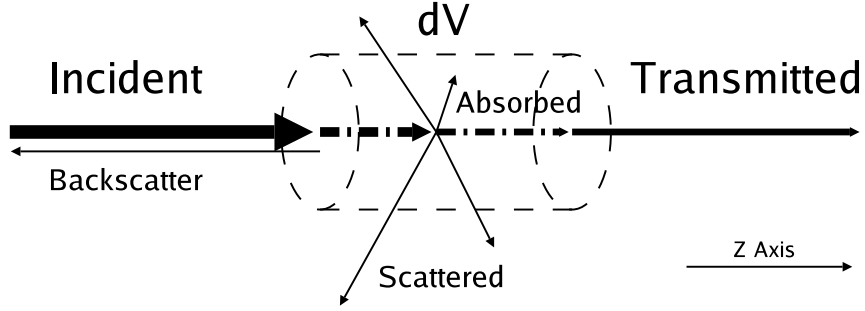
Figure 2.4: Diagram illustrating radiation transfer across an infinitesimal cylinder.

where, $\tau(z_1, z_2)$ is the optical length, $\tau(z_1, z_2) = \int_{z_1}^{z_2} \kappa_e(z)\mathrm{d}z$.

Equation 2.6 can now be applied to scatterometery. For the moment, consider a single scatterer at some depth, d, beneath the surface embedded in an absorbing material, where $\kappa_e = \kappa_a$. As an incident pulse penetrates the material, the power is attenuated due to absorption as described in Equation 2.6. Once the pulse reaches the scatterer a portion of the energy is scattered back. This backscattered pulse then travels back through the absorbing material. The apparent cross-section of the scatterer is then,

$$\sigma = \sigma' e^{-2\tau(0,d)}, \tag{2.7}$$

where σ' is the cross-section of the scatterer when not beneath the surface of the absorbing material. The volume scattering from an infinitesimal volume behaves much the same as a single scatterer. However, volume scattering typically is a result of many scatterers. The scattering coefficient, κ_s, is used to describe the effective scattering loss, and thus in volume scattering materials κ_s is non-zero. Therefore, generalizing the effects of back-scattering to volume scattering, the normalized backscatter from a single infinitesimal volume is

$$\mathrm{d}\sigma^o = \gamma(d)e^{-2\tau(0,d)}, \tag{2.8}$$

13

where $\gamma(d)$ is the total backscatter contribution from the infinitesimal volume at depth d. The total backscatter is then,

$$\sigma^o = \int_0^\infty \gamma(z)e^{-2\tau(0,z)}\mathrm{d}z. \tag{2.9}$$

This equation describes the backscatter from a distributed volume target when the number of scatterers is very large.

2.4 Summary

By applying radiation transfer to scatterometery, we can gain further insight into the mechanisms that affect backscatter in the Greenland ice-sheet. Particularly, applying scatterometery and radiation transfer to snow melt allows models to be generated and the effects of melt quantified. The foregoing discussion of these topics is only a brief outline of the material. An inquiring reader should review the vast amount of literature to gain further insight.

Chapter 3

Improving Temporal Sampling

The tandem mission of QuikSCAT and SeaWinds marks the first time in history that two identical Ku-band scatterometer instruments have been in orbit around the earth simultaneously. The combination of data from these two satellites provides an unprecedented sampling of the earth's surface, allowing the detection of short-lived and diurnal processes. Backscatter from millions of individual radar pulses are recorded in this tandem dataset daily. While individual backscatter measurements can be used, the generation of images combines measurements into a compact dataset that allows easier processing and intuitive interpretation. Moreover, by generating images from many individual measurements, information gained from overlapping measurements gives insight into the spatial response. The resulting images, while having reduced temporal sampling diversity, enjoy improved spatial resolution.

However, in generating images care must be taken to insure that temporal resolution is not unreasonably lost. This chapter describes some of the temporal shortcomings of the currently produced polar ascending and descending images, and how these shortcomings can be belayed. First, Section 3.1, provides background into the SeaWinds instrument aboard the QuikSCAT and ADEOS II satellites, as well as a discussion on the Scatterometer Image Reconstruction (SIR) algorithm, and the images currently produced. Next, Section 3.2 describes the sources of temporal resolution degradation in polar ascending and descending images. Then, Section 3.3 discusses a new method of producing images that improves the image temporal resolution in the polar regions. Lastly, Section 3.4 summarizes the results of the new processing method.

3.1 Background

This section gives background information on the SeaWinds instrument aboard the QuikSCAT and ADEOS II satellites. In addition, this section describes the SIR algorithm.

3.1.1 SeaWinds instrument

The SeaWinds instrument was designed to measure vector winds over the ocean. Transmitting electromagnetic pulses at 13.6 GHz, this instrument is sensitive to scattering on the ocean from centimeter wavelength ripples caused by shear-stress from near-surface winds. Though this instrument was designed primarily for measuring ocean wind vectors, the principles of scatterometry are also applicable to land studies. This instrument uses a conically scanning parabolic reflector with two feeds, for measurements of both horizontal- and vertical-polarized backscatter. The use of two feeds results in two pencil-beam antenna patterns at $\simeq 46°$ incidence for h-pol measurements, and $\simeq 54°$ incidence for v-pol measurements.

The SeaWinds instrument has been flown on two different satellites. The first instrument was flown on the QuikSCAT satellite, which instrument is referred to by the platform name, QuikSCAT. QuikSCAT was launched in June of 1999 and continues to be operational. The SeaWinds instrument was also launched aboard ADEOS II. This satellite and instrument together are referred to as SeaWinds. SeaWinds was launched in December of 2002. The SeaWinds mission ended prematurely due to a power system failure. During the length of the SeaWinds mission, from Julian Day (JD) 100 to JD 297 of 2003, both SeaWinds and QuikSCAT were operational. Because these two satellites carry identical sensors, the data of these missions can be combined. The combined mission of the SeaWinds and QuikSCAT missions is referred to as the tandem mission.

Although the sensors aboard SeaWinds and QuikSCAT are identical, their platforms are slightly different. Perhaps the most notable difference, especially concerning temporal sampling, is the difference in the local time-of-day when the satellites cross the equator. Both satellites fly in a sun-synchronized retrograde polar orbit.

16

Sun-synchronized orbits are unique because the orbital plane maintains a constant angle to the sun. Thus, the local time-of-day beneath a sun-synchronous satellite at the equator is always the same. QuikSCAT crosses the equator northbound, the point called the ascending node, at roughly 6:00 AM local time, whereas SeaWinds has its ascending node at roughly 10:00 PM local time. The descending node, the southbound equator crossing point, occurs for QuikSCAT at 6:00PM local time, and for SeaWinds at 10:00 AM local time. Other differences between the satellite platforms also exist. For example the orbital stability is slightly better on the QuikSCAT instrument due to it being placed in a geodetic orbit where the SeaWinds instrument is placed in a geocentric orbit. Though additional differences exist, both sensors' measurements are closely cross-calibrated, allowing their measurements to be considered essentially identical.

3.1.2   Scatterometer Image Reconstruction

Tandem SeaWinds and QuikSCAT measurements are used to make images of the polar regions. These images are processed using the Scatterometer Image Reconstruction (SIR) technique. The SIR algorithm is based on a multivariate form of block multiplicative algebraic reconstruction. By combining multiple overlapping passes, each with several measurements near the same area, this method provides enhanced resolution measurements of the surface [27]. A short description follows (more detailed discussions are found in [27, 28]).

Let $f(x, y)$ be a function describing the surface σ^o at the point (x, y). The measurements can be modeled by [27],

$$z = Hf + \text{noise}, \tag{3.1}$$

where H is an operator that describes the measurement system, i.e. the sample spacing and aperture filtering, and z is the measurement recorded by the instrument. In effect, to find an estimate of the surface $f(x, y)$, the inverse problem is solved,

$$\hat{f} = \hat{H}^{-1}z, \tag{3.2}$$

17

where $\hat{f}$ is the surface estimate, and $\hat{H}^{-1}$ is the effective inverse operator of H. The inverse operator of H, $\hat{H}^{-1}$, is exact only if H is invertible and the measurements are noise free, in which case $\hat{f} = f$. Effectively, the SIR image algorithm improves the resolution by using information contained in the sidelobes of the spatial response. The resulting images have finer resolution than the main beamwidth of the inherent aperture spatial response of the instrument. In the process of inverting the aperture response, the noise level is increased somewhat due to the noise being amplified in regions where the aperture response is near zero.

The instrument on SeaWinds and QuikSCAT has two measurement types: "eggs" and "slices". The "egg" measurement type refers to the elliptical spatial response on the ground of the pencil beam aperture which has dimensions of approximately 25 km by 36 km. "Slices" are range/doppler processed apertures that slice the elliptical footprint almost perpendicular to the semi-major axis. These "slices" have different shapes depending on their orientation, but have nearly rectangular apertures approximately 6 km by 25 km. SIR images using the full antenna aperture produce "egg" images with approximately 9 km spatial resolution, where SIR images using the range-doppler processed footprints produce "slice" images with effective resolution between 3–6 km.

In the production of SIR images, many auxiliary images are also produced. However, this chapter focuses on the image type produced by the SIR algorithm that estimate the time that each pixel was measured. This "time" image is referred to as the **p** image [29].

3.2 Temporal Resolution: Ascending and Descending Image Drawbacks

In currently available products, daily data is temporally separated into three images: daily, ascending pass-only, and descending pass-only. Ascending- and descending-only images are created to increase the temporal sampling and resolution in order to study diurnal processes and short-lived natural phenomena. Because ascending and descending images contain only half of the available data, they have reduced spatial coverage in lower latitudes. In higher latitudes however, ascending and

descending images suffer from poor temporal resolution due to inadequate temporal separation. The root causes of temporal-resolution degradation—swath overlap and day boundary effects—and their effect on the available ascending/descending images are discussed in detail in the following subsections.

3.2.1 Swath Overlap Effects

The temporal resolution shortcomings of the current ascending and descending product is, in part, a result of ascending and descending pass overlap. In order to understand the effect of ascending and descending pass overlap on the available images, the satellites' orbital and instrument geometry near the poles must be understood.

QuikSCAT and SeaWinds satellites are sun-synchronous. At lower latitudes this essentially means that the measurements of each satellite occurs at roughly the same local time of day for each ascending and descending pass. Near the poles, however, this concept of constant local time inadequately describes the sampling. The local time of ascending node (6:00 AM for QuikSCAT, 10:00 PM for SeaWinds) is 12 hours different from the local time of the descending node local time (6:00 PM for QuikSCAT, 10:00 AM for SeaWinds). In the transition from ascending to descending each satellite crosses 12 local time zones. In the polar regions, lines of longitude, and thus the local time zone boundaries, are close together. It is at these high latitudes that QuikSCAT and SeaWinds transition most of the 12 time zones. This local time transition is common to all sun-synchronous satellite orbits, and does not directly affect the temporal resolution of the images produced. However, QuikSCAT and SeaWinds images produced by separating by only ascending and descending passes suffer from a loss of temporal resolution due to the conically scanning pencil beam system employed by the SeaWinds instruments.

Figure 3.1a shows an Arctic QuikSCAT SIR image created from one day of data, and Figure 3.1b is the same image masked to exclude all but one pass of the satellite. The north pole is in the center of the image. Because the transition from ascending to descending occurs at the northern-most point in the satellites' travel, roughly half of the pass shown in Figure 3.1b is ascending and half descending. Figure
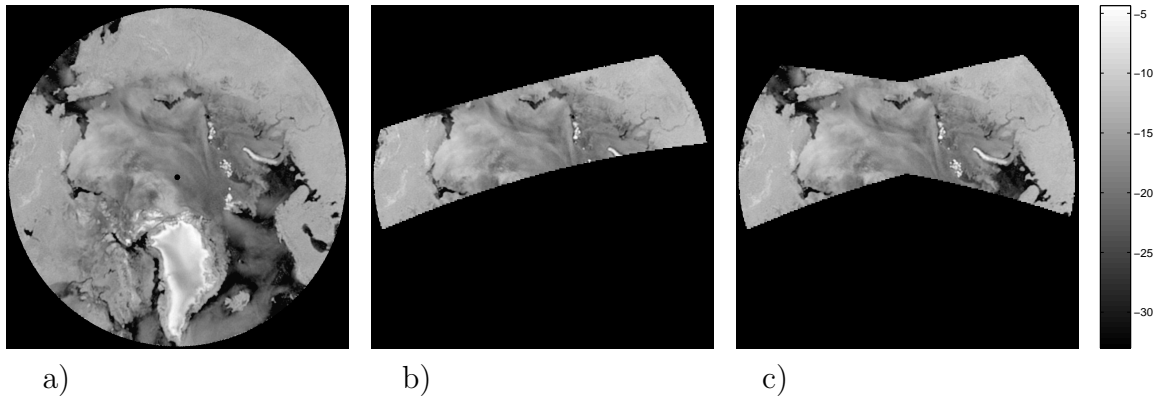
Figure 3.1: Image shows a) a typical one-day v-pol QuikSCAT SIR image of the Arctic which includes multiple passes, b) the same image masked to show the coverage of a single pass, and c) the same image masked to show the coverage of two consecutive passes.

3.1c shows the same SIR image masked to exclude all but two consecutive passes. The second pass is much like the first, but rotated about the pole by some angle due to the rotation of the Earth under the satellite.

Because QuikSCAT uses a conically scanning pencil beam, every rotation of its parabolic reflector sweeps out a circle on the earth's surface centered around the nadir point of the satellite. This circle of measurements can be divided into two groups, forward-looking and aft-looking. When the satellite reaches its most northern point, it transitions from ascending to descending. Before this occurs the satellite measures forward from that transition point, and after the transition the satellite continues to measure aft of that transition point. This causes a circular region where the forward-looking measurements are still ascending, but the aft-looking measurements are descending. Figure 3.2 contains a diagram showing how the measurements of a single pass are divided into ascending and descending passes. This region of pass overlap is a primary cause for temporal resolution loss in ascending/descending images because the data collected each pass has data in ascending images that is separated by only a few minutes from similar data in descending images.
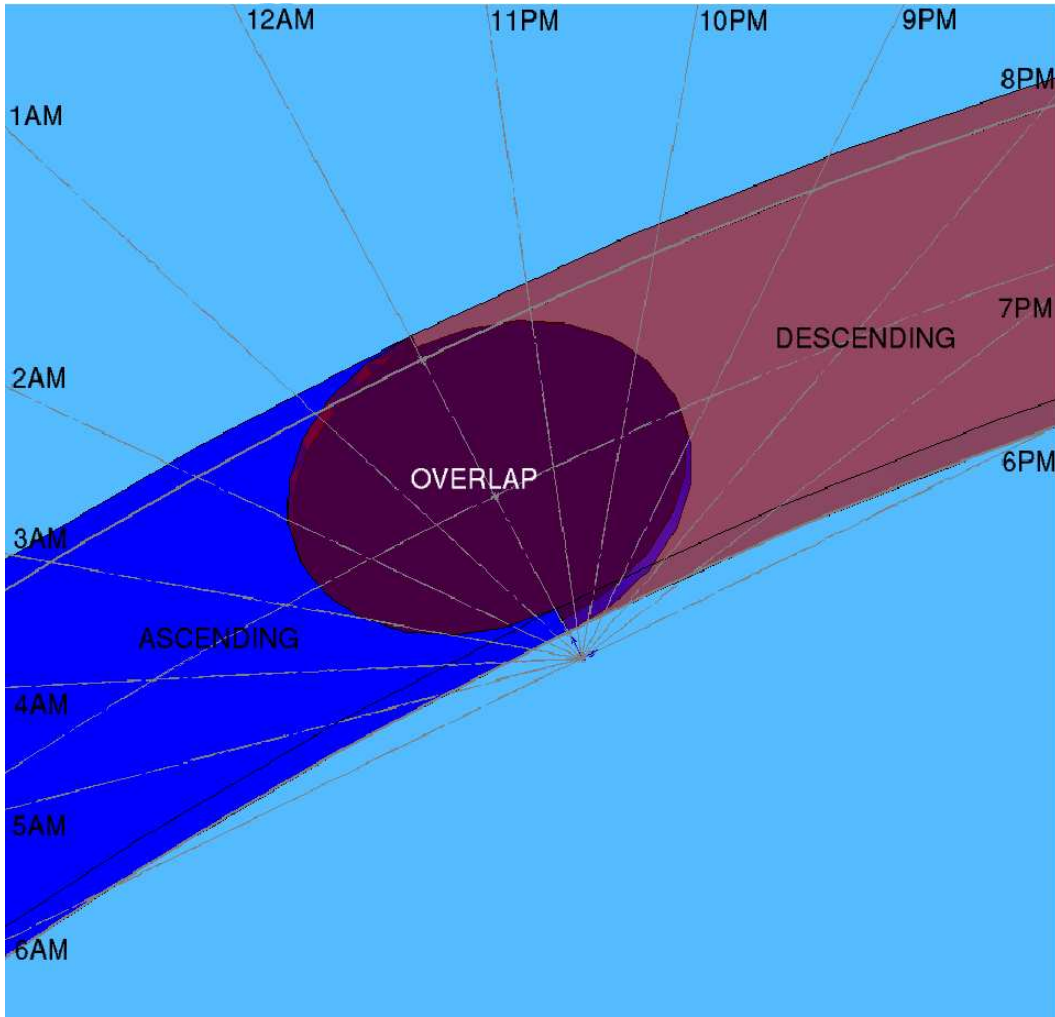
Figure 3.2: Diagram illustrating a QuikSCAT transition from ascending pass to descending pass in the Arctic. The lines radiating out from the center depict the local time zone boundaries. There is significant overlap of the ascending and descending data. The SeaWinds ascending-to-descending transition occurs at roughly 4PM local time, 8 hours before QuikSCAT.

Figure 3.2 illustrates the local time transition that occurs in the Arctic region. Note that the northern most point in the satellites travel the local time of day is 12:00 AM at nadir, halfway between 6:00 AM and 6:00 PM. Because the disk-shaped region of overlap for each pass is closely located to the poles, it covers many lines of longitude and thus many local time zones. Since each pass suffers from this overlap, and as many as 8 consecutive passes cover a particular area on the ground, the regions north of $\sim 73°$N and south of $\sim 73°$S suffer from the effects of this overlap.

Figure 3.3a shows a count of the number of observations over each pixel made by nine consecutive orbits in a typical daily SIR image. Because each satellite orbits the earth every 100 minutes, the daily averaged σ_0 SIR images include data from roughly 14.25 consecutive passes, repeating the same coverage pattern every 4 days. Figure 3.3a also shows another interesting feature: after only nine orbits the first and the last passes are already starting to overlap, seen on the right side of the image. The overlap shown is a result of the satellite passing through roughly the same location twice a day, and is what makes twice-daily full coverage images of the Arctic and Antarctic possible for each satellite in isolation.

Figures 3.3b and 3.3c are images showing the number of passes over each pixel that nine consecutive orbits make when separated into ascending and descending pass images respectively. The rounded edges on each of the ascending and descending passes are a direct result of the circular overlap region illustrated in Figure 3.2.

In the creation of **p** images, the effective pixel time is estimated using a non-linear averaging technique. The pixel time is found by weighting each sample's time by its backscatter measurement value before being averaged together. This non-linear method of averaging is used to counteract an inherent time bias due to the SIR process [29]. This weighted time average becomes the value of that pixel in the **p** image. Since each of the passes have an ascending/descending pass overlap region, the separation between the ascending and descending **p** images is much less than the ten to twelve hours desired. Figure 3.4 shows the time separation between the ascending and descending images over a small region corresponding to the region left of the north pole in Figures 3.1a, 3.3a, 3.3b, and 3.3c. As expected, the areas of high latitude where

22

a)　　　　　　　　　b)　　　　　　　　　c)
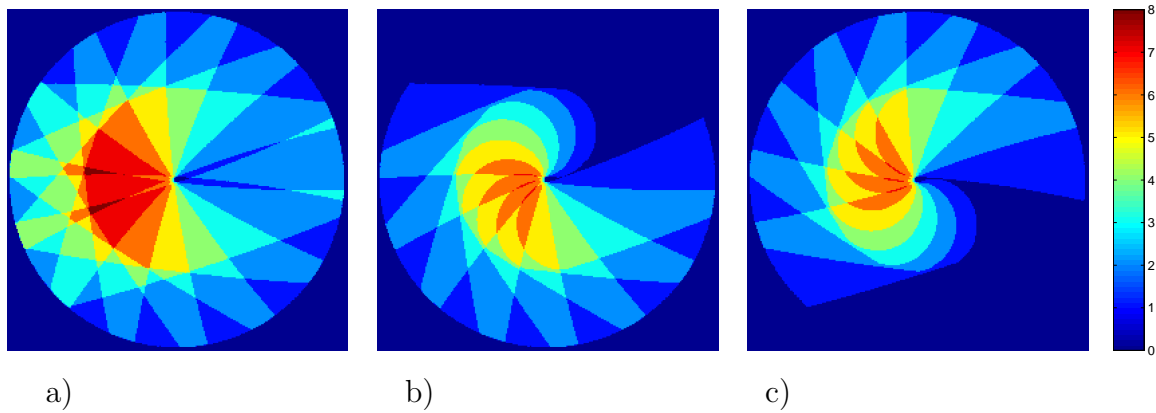
Figure 3.3: Images show how nine consecutive passes of QuikSCAT overlap in the Arctic for a) full passes (daily images), b) ascending passes, and c) descending passes. Pixel color shows the number of swaths that passed over each pixel. Note the emerging pattern on left of the center. Note that at high latitudes only one or two passes are exclusive to each ascending and descending image.

the ascending and descending images share temporally similar data have very little time separation. The small separation time between the ascending and descending images confirms the temporal resolution loss, as well as showing quantitatively the temporal limitations of these images.

In general, overlapping satellite passes tends to suppress transients, and in most cases also decreases temporal resolution. On the other hand, averaging multiple consecutive passes can lessen the effect of noise and other anomalies on the output images. Because of the factors involved, there is a compromise made when one choses temporal resolution over spatial resolution. Maximizing temporal resolution while maintaining high spatial resolution is a strong motivator for improving the current method of image separation. By eliminating the overlap between ascending and descending passes temporal resolution is significantly improved with minimal change in spatial resolution. Section 3.3 describes this method.
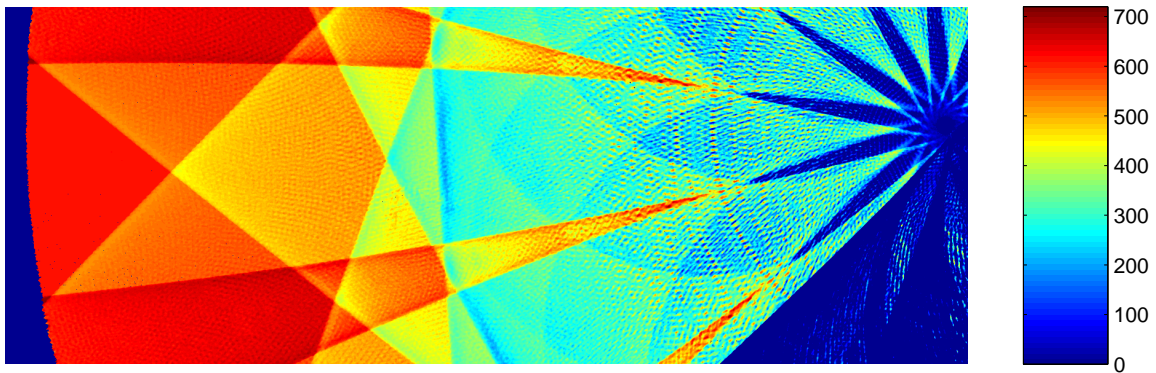
Figure 3.4: Image showing the time separation in minutes between the same-day descending and ascending pass images. Note that the north pole is located in the upper right.

3.2.2   Day Boundary Effects

Perhaps the greatest limitation of using separate ascending and descending images to provide temporal resolution in the polar regions is the effect of day boundaries. The day boundary-affected region (seen as the region between the red and blue regions where the color varies in Figures 3.5 and 3.6) is especially damaging to temporal resolution, because data separated by nearly twenty-four hours is averaged together. Current polar QuikSCAT SIR images are created from one twenty-four hour time period. All valid data taken during that twenty-four hour period is used to create the images. There are significant portions of the Arctic and Antarctic where the first several passes and the last several passes of each day cover the same area for ascending and descending images, due to the wide swath. Figures 3.5 and 3.6 are QuikSCAT and SeaWinds **p** images, respectively, from JD 258 2003. Figures 3.5a, and 3.6a are ascending images, and 3.5b, and 3.6b are descending images. These **p** images show the areas where the first and last passes overlap.

The effects of the day boundary swath overlap are even more apparent in Figure 3.7. This image shows the time between the ascending and descending images. This difference image shows both positive and negative time separation, because the ascending image precedes the descending image in some regions, while in others the
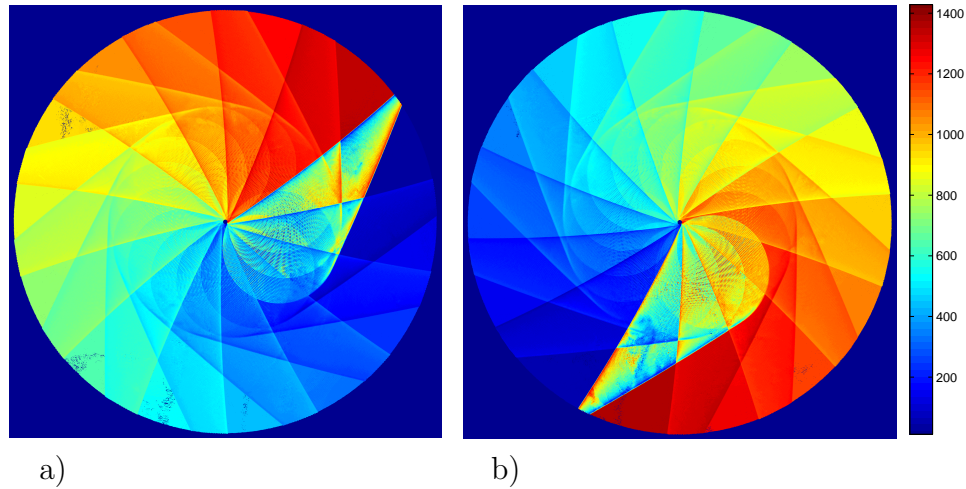
Figure 3.5: Ascending (a), and descending (b) QuikSCAT effective pixel time images (**p** images) from JD 258 2003. Note the area to the right of center in (a), and below center in (b), where the first several passes and the last several passes overlap.
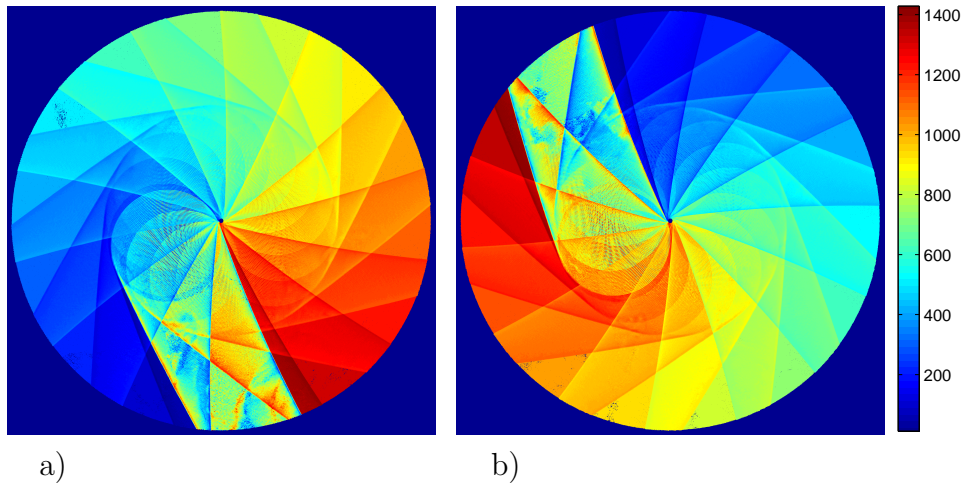
Figure 3.6: Ascending (a), and descending (b) SeaWinds **p** images from JD 258 2003. Note the area to the left of center in (a), and below center in (b), where the first several passes and the last several passes overlap.
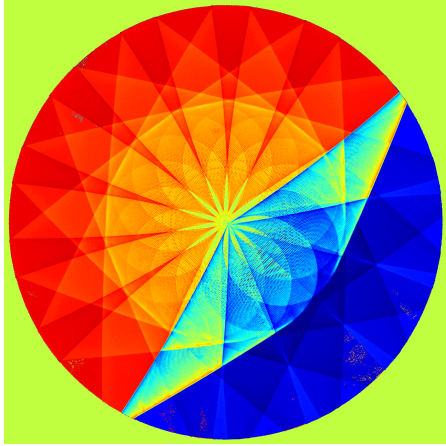
Figure 3.7: Image showing the difference in time of day of the ascending passes shown in Figure 3.5a and the descending passes shown in Figure 3.5b. Time separation in minutes – descending first is positive.
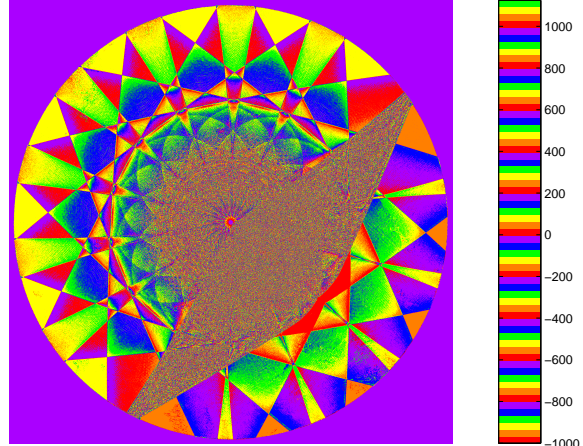
Figure 3.8: Same image as Figure 3.7 only with a different color scheme to emphasize the variance in the day boundary affected region.

descending image precedes the ascending image. The day boundary is the region of the image that separates the ascending-first region with the descending-first region. In general, the apparent (average) time separation is low across the entire day boundary affected region. In the day boundary affected region, the variance of time separation is also much larger than in the zones unaffected by day boundaries, shown in Figure 3.8. The high variance makes useful data extraction of time of day at any given location depend on the day in question. Conversely, the time of day for any given image is highly dependent on the exact pixel location.

The **p** image values in the day-boundary affected region also suffer from another problem: the reported time does not correspond to when any of the measurements are actually taken. Therefore, the **p** pixel values may be misleading when studying diurnal variations in this region. For any application of the images requiring time of day measurements or better than daily temporal resolution, using ascending and descending images in the polar regions is difficult at best.

26

a) First   b) Second   c) Third   d) Forth
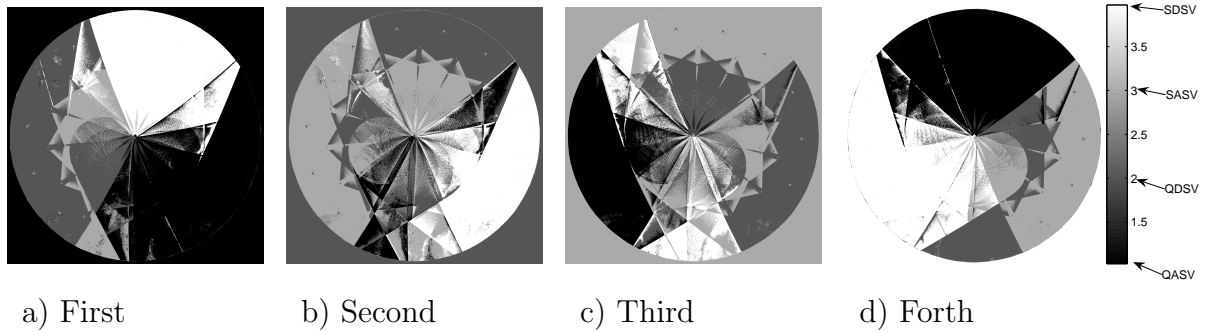
Figure 3.9: Chronological order of the four QuikSCAT/SeaWinds ascending and descending images, by pixel. Sequential order varies significantly based on the pixel, making proper chronological sequencing of the images difficult. The pixel color describes which image type is first, second, third, or fourth. The labels used include QASV – QuikSCAT Ascending Slice V-pol, QDSV – QuikSCAT Descending Slice V-pol, SASV – SeaWinds Ascending Slice V-pol, and SDSV – SeaWinds Descending Slice V-pol.

The problems associated with the day boundary effect become more poignant when the ascending/descending images from SeaWinds and QuikSCAT are used in tandem. Conceptually, the combination of the QuikSCAT and SeaWinds imageset should provide higher temporal sampling frequencies than with either one separately. In practice, however, the usefulness of these images as independent samples, and the resulting temporal resolution, is not nearly as good as would be expected for the polar regions. Because the day boundary location is different for each image type (QuikSCAT ascending, SeaWinds descending, etc.), the chronological order in which the images should be placed varies from location to location. Figure 3.9 illustrates the problem with chronological sequencing of the images. As a result of the unclear chronological sequencing, using the four images in studies over large areas of the polar regions becomes complicated.

If we restrict the area of study to a single pixel, chronological ordering of the image pixels is simplified. However, the information provided may not be very useful. Figure 3.10 shows the individual measurements of QuikSCAT and SeaWinds, and how their image values are arranged chronologically. Largely due to day boundary affects on the SeaWinds data, the image values shown in Figure 3.10b do not represent

the measured data very well. This causes all four QuikSCAT/SeaWinds images to be closely grouped temporally in Figure 3.10c—often within 4–6 hours of each other. Note from Figure 3.10c that the samples do not accurately follow the data, and do not exhibit temporal resolution better than that of each satellite separately.

The effects of a day boundary are unavoidable in images made with shorter than daily temporal resolution because the satellites' sun-synchronous near polar orbit and wide swath. In the ascending and descending images, these day boundaries affect a large portion of the Arctic and Antarctic images. Because this effect is inevitable, efforts to lessen the affected area motivates us to improve on the current images.

In conclusion, using the QuikSCAT/SeaWinds ascending and descending polar images as unique samples does not accurately portray the underlying data. Because of the effects outlined in this section, namely swath overlap and day boundary effects, the resulting images have excess temporal variability, and degraded temporal resolution, making the images too closely correlated to be used independently. Thus, a new approach is needed.

3.3   Improving Temporal Resolution: Time-of-Day Images

Because there is wide variation in local sample times across the wide swath of QuikSCAT and SeaWinds in the polar regions, a new method of separating the daily data can be accomplished by using the local times of the samples themselves rather than the direction of the spacecraft's motion. In this method, a particular local time of day is used as a decision boundary. This boundary determines whether to include any given datum into a image. Thus, a particular local time of day is used to separate the data into distinct images. By separating the data according to local time of day, all temporally similar samples are grouped into the same image.

Because QuikSCAT has a 6:00 AM ascending node and a 6:00 PM descending node, a logically intuitive approach is to set the time boundaries for QuikSCAT-only images at 12:00 AM and 12:00 PM. As shown previously in Figure 3.2, these boundaries correspond to a line perpendicular to the spacecraft's travel, almost exactly through the transition point where the spacecraft transitions from ascending

Figure 3.10: Graph showing individual measurements and image values for a particular pixel (84.0 N 135.4 W from JD 163 to JD 167 2003) for a) QuikSCAT ascending/descending, b) SeaWinds ascending/descending, and c) Combined QuikSCAT/SeaWinds. Note that at this location, SeaWinds suffers from day boundary effects, making its image values appear between groupings of data. The usefulness of the ascending/descending images at this pixel are questionable: all the samples are grouped within 6–10 hours of the day, and when chronologically ordered they do not follow the raw data well.
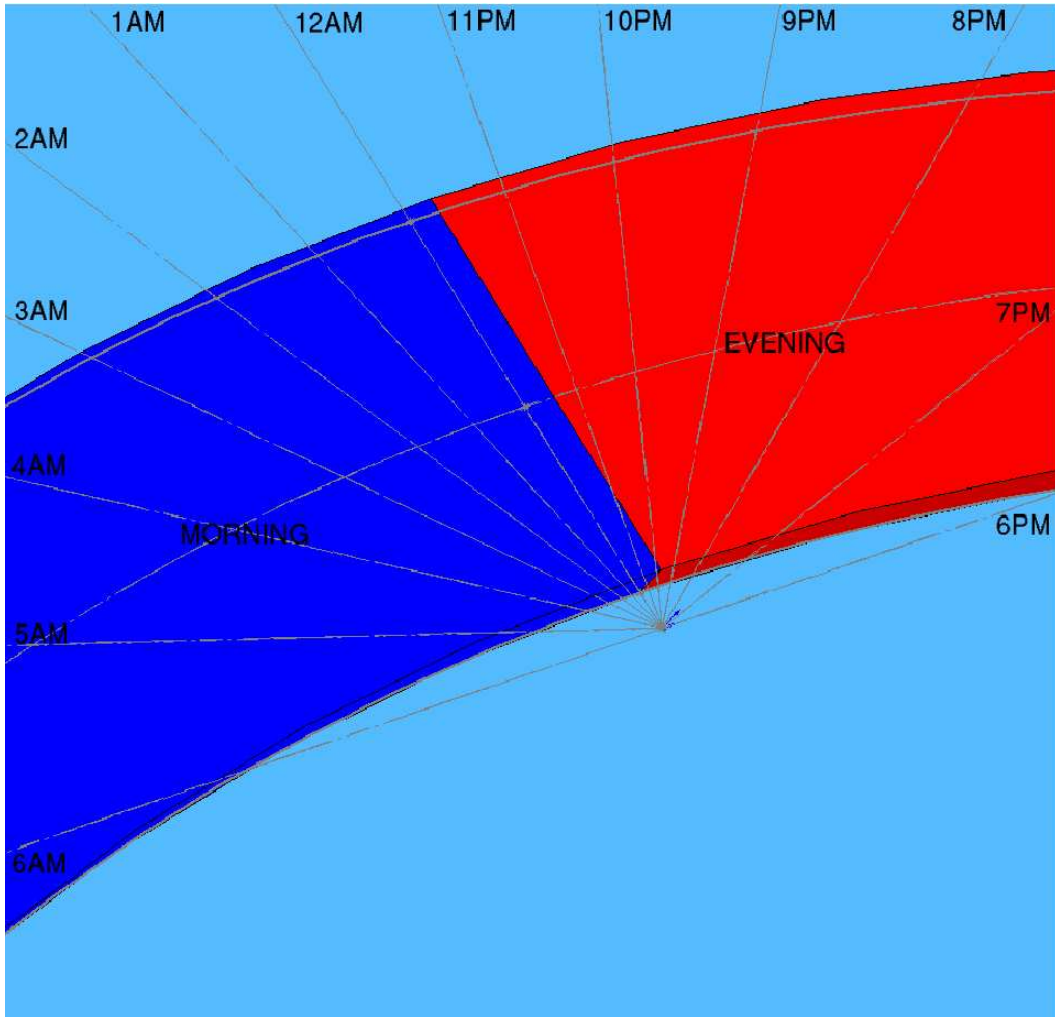
Figure 3.11: Diagram illustrating the transition from morning pass to evening pass in the Arctic. The lines radiating out from the center depict the local time zone boundaries. Note in contrast to Figure 3.2 that there is no overlap of the morning and evening data.

to descending and visa versa. Figure 3.11 shows a diagram similar to Figure 3.2 which illustrates the new time-of-day method of separating the images. Similarly for SeaWinds-only images, an intuitive time boundary that divides the swath nearly perpendicular to the spacecraft's travel is achieved at 4:00PM and 4:00AM.

Taking a similar approach for tandem images in the Arctic polar regions, time boundaries are placed at 12:00AM dividing QuikSCAT passes in half, at 4:00 PM, dividing SeaWinds passes in half, and at 8:00 AM, a time when no measurements are recorded. These time boundaries result in three 8-hour images in the Arctic: morning (12:00 AM to 8:00 AM), midday (8:00 AM to 4:00 PM), and evening (4:00 PM to 12:00 AM). Antarctic tandem images use time boundaries 12 hours different from the Arctic images to achieve the same effect, dividing the swath near the southern most point in the spacecrafts' travel. Antarctic 8-hour images, therefore are of three types: morning (4:00 AM to 12:00 PM), midday (12:00 PM to 8:00 PM), and evening (8:00 PM to 4:00 AM). Figure 3.12 shows the image time boundaries, and the chronological order of the images for a single day's worth of images. Note that the images' local time is restricted to a narrow 8-hour period. However, the universal time (UTC) of data in these images extend 12 hours before and after this 8 hour window. Because the filenames associated with the images use UTC extensions, they are labeled indicating a two day image, even though they contain only 8 hours (local time) of data. Only one of the three images (evening in the northern hemisphere and morning in the southern hemisphere) contain data from both satellites. Only three images, rather than four, are created for this reason: measurements from both satellites are taken at similar times during one 8 hour portion of the day.

The placement of the time boundaries, although apparently placed somewhat arbitrarily, have implications if they are moved from these values. Because of the way local time boundaries slice through the swath data, improper placement of the boundary may cause visible anomalies along the temporal decision boundaries of each pass. The time boundaries used here insure that the swaths are sliced in a way that minimizes the potential for such anomalies. This also reinforces the justification for creating three images a day instead of four.
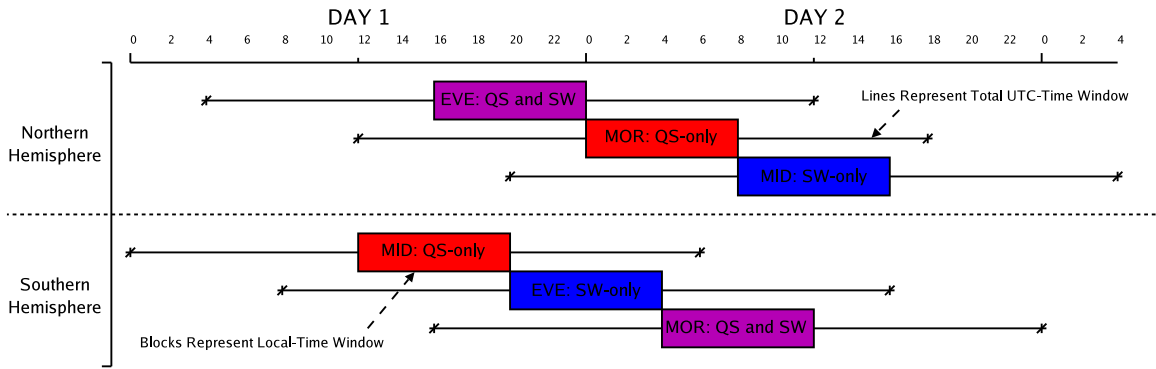
Figure 3.12: Diagram illustrating the time boundaries used in the creation of tandem morning, evening, and midday images, for both the Arctic, and Antarctic. Though the local time-of-day is restricted to an eight hour period, the UTC window extends up to 12 hours before and after the local-time window. Only one of the three images (evening in the northern hemisphere, morning in the southern hemisphere) contain data from both satellites.

The day boundary sequencing problem described previously in Section 3.2.2 and illustrated by Figure 3.9, is also eliminated by the new method. The day boundary problem is eliminated because the day boundary-affected region on the images is moved to the same small location in all the images. As a result, the image time for each pixel, regardless of its location in the image, is assured to follow a well defined chronological order.

Figure 3.13 shows three consecutive days of raw QuikSCAT and SeaWinds data samples at a particular location (84.0 N 135.4 W), and the resulting morning, midday, and evening values. Individual passes are seen as vertical columns of data because the measurements are separated at most by a few minutes. Contrast this figure with Figure 3.10, which shows the combined QuikSCAT/SeaWinds ascending and descending image dataset. This method, which uses the local time of day instead of satellite motion to define the images, exhibits dramatically improved sampling. The actual time separation between images does not deviate far from 8-hours, resulting in a near uniform sampling of the surface with three samples per day. This raises the upper bound on signal frequencies that can accurately be represented without
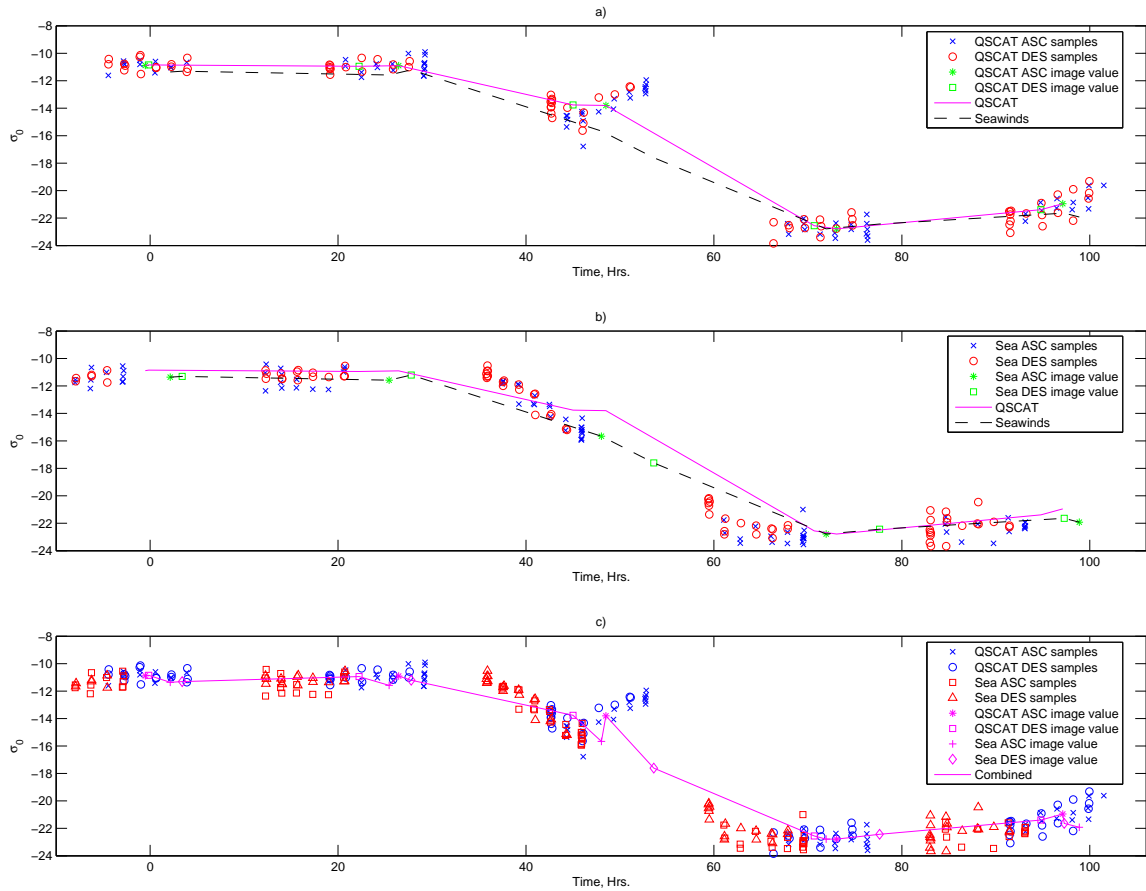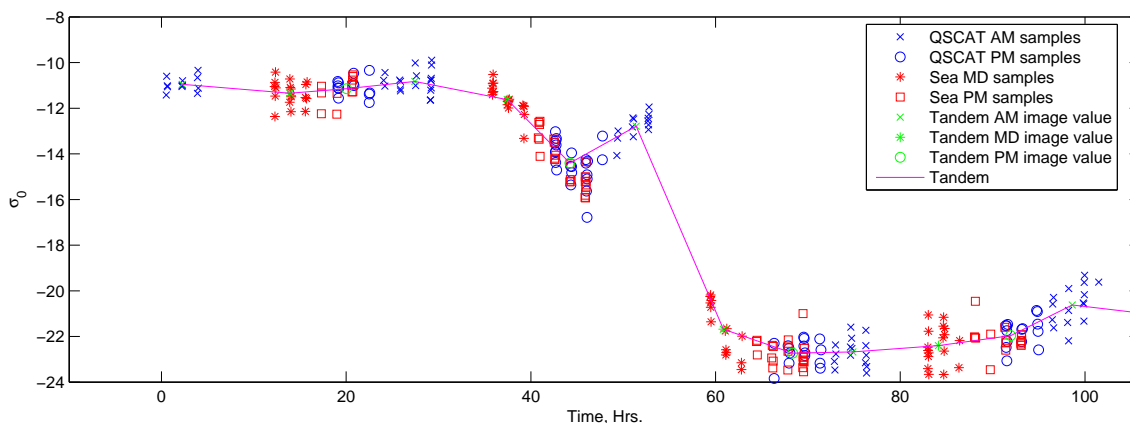
Figure 3.13: Graph showing individual measurements for a particular pixel (84.0 N 135.4 W from JD 163 to JD 167, 2003) for QuikSCAT and SeaWinds and the resulting morning, midday, and evening image values that result from applying the new time-of-day method to the tandem data. Contrast with Figure 3.10. Note the near uniform, three daily samples that this method provides.

aliasing to those with periods shorter than 24 hours, making diurnal variations of the signal much more distinguishable. Note from Figure 3.13, that only the evening image contains data from both satellites.

The resulting improvement of temporal resolution in morning/midday/evening images using the time-of-day method is due to the temporal grouping of data. As mentioned previously, Figure 3.11 shows how the swath is divided in the new method. Contrast this diagram with Figure 3.2, which shows how the swath was separated for the ascending/descending method. The sharp division in the new method results in a pattern illustrated by Figures 3.14a and 3.14b, which shows the geometry of several consecutive passes separated by local time into morning and evening images respectively. In contrast to the swath geometry shown in Figures 3.3b and 3.3c, the number of swath observations in the high latitude region is 3 to 4 for the morning and evening images, and the sum of the two images never exceeds the total swath count shown in Figure 3.3a. The temporal sampling variability of the data in the ascending and descending images has been drastically reduced, resulting in temporally distinct images with more uniformly spaced samples.
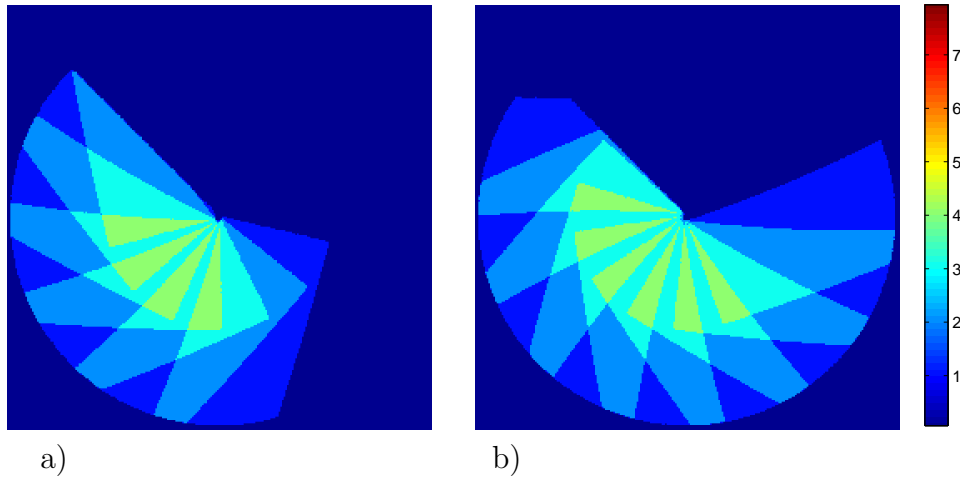
Figure 3.14: Images show how seven consecutive passes overlap in a a) morning QuikSCAT image and b) evening QuikSCAT image in the Arctic. Pixel color shows the number of swaths that passed over each pixel. Contrast with Figures 3.3b and 3.3c showing similar patterns for ascending/descending images.

Using the local time of day as the decision rule for separating the data and creating SIR images has the added benefit of controlling and relegating the day boundary affected region to a small portion of the image. Intuitively, the local time of day filter used by the time-of-day method places this region precisely over 180 degrees longitude, at or near the international date line. The day boundary affected region is only as wide as the antenna footprint coverage area, an area several pixels in width.

The morning/evening images have a clear line visible along the 180° longitude line, as a result of the day boundary affected region being concentrated at this location. This does have some negative repercussions. For one, the line clearly appears as an anomaly as the data transitions a twenty-four hour temporal discontinuity. This anomaly may negatively affect certain studies of ice movement in this portion of the world, making it more difficult to track the ice's movement across this day boundary without taking this into account.

3.4   Summary

A new time-of-day method, wherein polar images are created by separating the data according to the local time of the measurements, improves the temporal sampling of QuikSCAT and SeaWinds SIR images by forcing only temporally similar measurements from both satellites to be used in the same image. As a result the effect of swath overlap is eliminated, and the day boundary placed in the same location for each image. This drastically decreases temporal variability of pixel times in the region previously affected under the current method, increasing temporal resolution. In this new method, three images a day were chosen because of a several hour long period of time each day when both satellites swaths cover the same regions, making full coverage images possible for only three images a day. The resulting imageset provides three nearly uniform samples daily of the polar regions.

Chapter 4

Melt Detection Model

As discussed earlier, understanding the melting processes in Greenland is important to the study of the world's climate. However, direct measurement of the ice-sheet in Greenland is difficult without remote sensing. Scatterometers provide a practical and feasible means to frequently measure the ice-sheet backscatter from which melt conditions can be monitored. Hence, this chapter discusses a new, yet simple backscatter model for melting and refreezing snow and describes how the parameters of this model can be used to estimate melt. This new method is used to classify the snow-pack into three states: melting, refreezing, and frozen. The model parameters are also used to estimate the severity of both melt and refreeze. Further, this melt model is tested with a one-dimensional geophysical/electromagnetic model simulation, which verifies some of the key features of the melt model, and melt estimation technique.

This chapter is organized as follows. First, Section 4.1 discusses the theory and development of the parameterized melt model and its limitations. Section 4.2 combines the new melt model with a Markov chain model. The combined model is then used to detect and estimate melt. Section 4.3 describes a one-dimensional geophysical/electromagnetic model, to which the melt detection and estimation technique is applied and evaluated. Lastly, Section 4.4 summarizes the melt model and melt estimation technique.

4.1   Theoretical Melt Model

The ability to detect and separate melt from refreeze is important to the study of many ice-sheet parameters including ablation. Ablation occurs as liquid water leaves the ice-sheet, either by runoff, evaporation or sublimation. Ablation by runoff is expected to occur only when heat is flowing into the snow, i.e. only when it is melting. Ablation by evaporation is accelerated when liquid water is present near the surface, as the presence of liquid water near the surface increases vapor pressure which can then be removed by convection. Thus, both runoff and evaporation caused by melt near the surface have the potential to decrease the mass of the ice-sheet. Ablation is greatest when the flow of heat continues to melt water near the surface, producing more runoff, and maintaining liquid and vapor water near the surface. When melting stops, the water lost by runoff is not replenished, and less vapor is available near the surface, slowing ablation and signaling the beginning of refreeze. Runoff ablation that continues to occur after new melt has stopped is limited by the available liquid water. Ablation by evaporation further speeds the refreezing process, driving the liquid water to further depths and further decreasing in vapor pressure. Ablation, therefore, is limited during refreeze. Since ablation slows following the transition from melt to refreeze, the distinction of these two states is important to estimating ablation. The distinction of melt and refreeze is also important to other processes that are driven by the availability of liquid water near the surface.

Distinguishing melting snow from frozen snow is a difficult task due to the gradual nature of melting. Melt occurs as liquid water becomes present in the snow. As the liquid content in the snow increases, the physical and electrical properties change. However, the line distinguishing melt from frozen snow is complicated by the gradual change in these properties.

Typically, a threshold of the snow's properties is set to define the difference between melt and refreeze. The most distinguishing parameter of melting snow is the liquid water content, m_v, the percent of liquid water by volume present in the snow. This parameter has a dramatic effect on the electrical properties of the snow that makes this property change detectable by microwave sensors. Intrinsically, m_v

at any particular location is a function of depth. Thus, this section discusses the effect that m_v and other snow parameters have on the normalized backscatter, σ^o, observed by QuikSCAT and SeaWinds. From the understanding of the effects of melt on backscatter a layered model is developed, parameterizing the melt with depth.

As discussed in Chapter 2, the backscatter of snow is complex due to the combined scattering of all the snow grains mixed with melt water and air. Since radar pulses from scatterometers cover a very large area compared to the size of individual snow grains and water droplets, statistical approaches work well when the properties of the snow are well known. Unfortunately, the mapping of backscatter to the snow properties is many-to-one, as various combinations of grain sizes, liquid water content, density, and other snow parameters can result in the same backscatter. While the mapping of backscatter to the snow properties is possible with some *a priori* information about the snow, this is often not available in the Greenland snow-pack.

Though *a priori* information on the snow parameters is not available, statistical models and supporting empirical evidence are useful in predicting and understanding the effects of changing conditions on the radar response to the snow-pack. For example, we know from models and empirical evidence that when snow melts, the imaginary part of the effective dielectric constant ϵ'' increases very rapidly. With the addition of liquid water resulting in an m_v of only 0.5%, ϵ'' increases sharply—over an order magnitude of change [31]. This drastic increase makes the snow change rapidly from a strong scattering, weakly absorbing material to a material that is dominated by absorption. Because of the electrical changes of the snow, melting decreases the backscatter contribution from wet snow, and attenuates the contribution of snow beneath. The resulting wet snow backscatter is considerably less than the backscatter of dry snow.

The wetness of the snow and its effect on the backscatter depend on the concentration and depth of the melt. The effect of concentration and depth of melt can be addressed using a simple layered model originally developed by Ashcraft and Long in [11]. This simple layered model ignores surface effects (i.e. assumes perfect transmission at the surface). This is reasonable for QuikSCAT because the $\simeq 54°$ incidence

$$\sigma^o = (1-\alpha^2)\sigma^o_{wet} + \alpha^2\sigma^o_{dry}$$

Wet Snow

Dry Snow
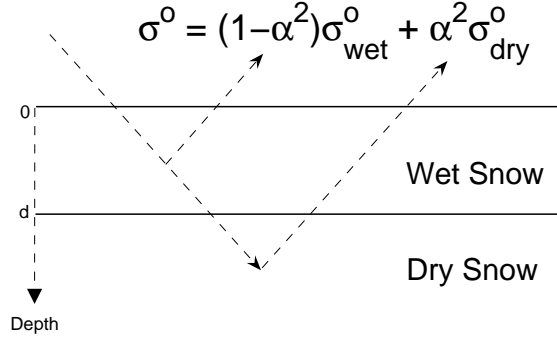
Figure 4.1: Diagram describing the backscatter from the two layer model.

angle of the 13.4 GHz vertically polarized waves are near the Brewster angle of the snow. Thus, this model assumes the snow is a volume scattering material. Therefore, radiation transfer theory can be used. Equation 2.9, which describes volume scattering using radiation transfer theory, is restated here and includes a term to handle an oblique incidence angle,

$$\sigma^o = \int_0^\infty \gamma(z)e^{-2\tau(0,z)}\sec\theta(z)\mathrm{d}z, \tag{4.1}$$

where

κ_a — absorption loss coefficient

κ_s — scattering loss coefficient

κ_e — extinction coefficient $(\kappa_a + \kappa_s)$

$\gamma(z)$ — normalized volume backscatter at depth z

$\theta(z)$ — transmission angle at depth z, and

$\tau(z_1, z_2)$ — optical length $\int_{z_1}^{z_2} \kappa_e(z)\sec(\theta(z))\mathrm{d}z$.

The loss coefficients κ_a and κ_s are functions of frequency, grain size, density, temperature, and water content, as well as other physical characteristics of the snow. The layered model used by [11] separates the snow into two layers as shown in Figure 4.1. The melting snow, the top layer in this two-layer model, has uniform properties and extends from the air-snow surface to depth d. Below the wet snow, an infinite layer of dry snow, also having uniform properties, is found. Using this model the backscatter

39

in Equation 4.1 is simplified into separate contributions from wet snow and dry snow,

$$\sigma^o = \sigma_w^o + \sigma_d^o. \tag{4.2}$$

The wet snow backscatter contribution is

$$
\begin{aligned}
\sigma_w^o &= \int_0^d \gamma_{\mathrm{wet}} e^{-2\kappa_{e,\mathrm{wet}} z \sec\theta_w} \sec\theta_w \mathrm{d}z \\
&= \frac{\gamma_{\mathrm{wet}}}{2\kappa_{e,\mathrm{wet}}} (1 - e^{-2\kappa_{e,\mathrm{wet}} \sec\theta_w d}) \\
&= (1 - \alpha^2)\sigma_{\mathrm{wet}}^o, \tag{4.3}
\end{aligned}
$$

where $\alpha = e^{-\kappa_{e,\mathrm{wet}} \sec\theta_w d}$, $\sigma_{\mathrm{wet}}^o = \frac{\gamma_{\mathrm{wet}}}{2\kappa_{e,\mathrm{wet}}}$, $\kappa_{e,\mathrm{wet}}$ is the extinction coefficient of the snow when wet, and γ_{wet} is the normalized volume backscatter of the wet snow. The remaining backscatter contribution from the dry snow is

$$
\begin{aligned}
\sigma_d^o &= \alpha^2 \int_d^\infty \gamma(z) e^{-2\tau(d,z)} \sec\theta(z) \mathrm{d}z \\
&= \alpha^2 \sigma_{\mathrm{dry}}^o. \tag{4.4}
\end{aligned}
$$

By using a layered model described by only volume scattering, the surface reflections at the air/snow boundary, as well as the reflection from the wet snow/dry snow boundary are ignored. Because the incidence angle of SeaWinds v-pol is near the Brewster angle of snow, reflectivity at these interfaces is very small. Moreover, reflections between the wet and dry snow layers are minimal due to the magnitude of the dielectric constant varying only slightly between wet and dry snow. The subsurface scattering that does exist (which may be significant due to bulk ice formations such as ice lenses, glands and pipes) is included in the bulk scattering coefficient σ_{dry}^o, the backscatter that is observed when the ice completely refreezes. [11]

This model is a very simple, but reasonable, model of the ice pack in melt conditions. While the melt concentration in real snow is not uniform, a uniform equivalent melt can be defined that results in the same attenuation. The parameters of this model are σ_{dry}^o, σ_{wet}^o, and α. By allowing these parameters to be functions of position, the model remains flexible with regard to changing snow types that exist across the ice-sheet. When σ_{dry}^o and σ_{wet}^o are known, the backscatter can be used to

40

obtain the attenuation parameter α. This parameter α is a measure of the attenuation due to melt, and a potential measure of melt severity.

Like the snow parameters during melt, the physical and electrical properties of the snow during the refreezing process are also complicated by their gradual change. The refreeze process, however, is further complicated by the thermodynamic conditions that drive the refreeze. For this reason, using the two-layer model may not accurately describe the changes in backscatter contribution during refreeze. In particular, the propagation of refreeze may occur from the surface downward, as well as beneath the wet layer upward.

Consider the thermodynamics of the snow-pack: the melt process begins as sufficient heat is added to the air-snow surface causing the liquid water concentration to increase. This heat melts the top layers of the snow causing the liquid water to percolate downward as the liquid concentration increases. Thus, heat is delivered into the snow. Deep sub-surface temperatures remain well below freezing, counteracting percolation by slowly refreezing the deeper melt water. Thus for two-layer melt, the thermodynamic behavior of the melting snow is consistent with the model: a layer of partially melted snow exists on top of dry snow.

During the refreeze process, heat continues to be drawn deeper into the snow-pack by conduction as before, refreezing the snow from beneath. At the surface however, the direction of heat flow is not defined explicitly; heat may continue to be delivered into the snow at a slower rate, may be negligible, or may be drawn out of the snow by convection and radiation. If heat is being drawn out of the snow at the surface during refreeze, a layer of refrozen snow will form at the surface. The presence of a frozen layer at the surface has a considerable effect on the backscatter. Thus, the two-layer model for the snow during refreeze may be inadequate. Accordingly, a three-layer model is proposed for refreeze.

Figure 4.2 shows a diagram of the proposed three-layer model. This model allows the refreeze of the center layer to propagate both from the surface downward and from beneath the wet-snow layer upward. The existence of subsurface wet snow is consistent with passive radiometer observations [33], and SSM/I channel ratios

$$\sigma^o = (1-\beta^2)\sigma^o_{\text{dry}} + \beta^2(1-\psi^2)\sigma^o_{\text{wet}} + \beta^2\psi^2\sigma^o_{\text{dry}}$$
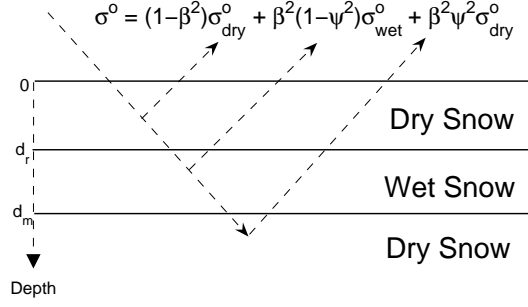
Figure 4.2: Diagram describing the backscatter from the three layer model.

[12]. Under this model, the equation for the total backscatter can be separated into contributions from each of the three layers. The total backscatter can be described by

$$\sigma^o = (1 - \beta^2)\sigma^o_{\text{dry}} + \beta^2(1 - \psi^2)\sigma^o_{\text{wet}} + \psi^2\beta^2\sigma^o_{\text{dry}}, \tag{4.5}$$

where $\beta = e^{-\kappa_{e,\text{dry}}\sec\theta_d d_r}$, $\psi = e^{-\kappa_{e,\text{wet}}\sec\theta_w(d_m - d_r)}$, $\kappa_{e,\text{dry}}$ is the extinction coefficient of dry snow, d_r is the depth of the top layer of refreeze, and $d_m - d_r$ is the thickness of the remaining wet snow layer. It is impossible to uniquely recover the depths d_m and d_r simultaneously for a single σ^o measurement. Thus, additional information is needed about either d_m or d_r. Since refreeze follows melt, more is known about d_m, the melt depth, than d_r. Because the propagation of refreeze from beneath the partially melted later is caused by a relatively constant flow of heat downward, one possible treatment is to make d_m change linearly with time. While this may be a good approximation, it adds another unknown parameter to the model, the rate of melt depth change—a parameter that is certain to be a function of position on the ice-sheet. A simpler approximation, one that does not require additional parameters, is to assume that d_m is constant. When the melt depth is large, changes in d_m have relatively little change in the backscatter due to the attenuation through the wet layer, as shown by simulation in Section 4.3.4. Therefore, holding d_m constant during refreeze is a reasonable compromise. Section 4.3.4 further addresses the validity of this assumption for the Greenland ice-sheet. Note however, that this assumption

requires that refreeze propagates from the surface downward—a good approximation given that this appears to be the dominant refreezing mechanism in the Greenland ice sheet as evidenced by the rapid increase in backscatter observations following a prolonged period of melt.

Using the theoretical framework of the two-layer melt and three-layer refreeze models it is possible to infer the depth of the melt and refreeze, and thus the severity of such events. With this framework defined, the implementation of this theory toward detecting and estimating these processes under realistic constraints can now be considered.

4.2   Melt Detection and Estimation

Classification of the melt state of the snow-pack requires that distinctive criteria be established for each state. As stated in the previous section, there is no clear distinction between melting and frozen states because the change of physical properties occurs gradually. Even less clear is the distinction between melting and refreezing. For realistic detection and classification of the melt state, a threshold of the snow parameters must be set which allows proper identification. The threshold needs to be chosen with the limitations of the model and the sensor systems in mind to reduce the potential for classification error.

The threshold for determining the states must depend on measurable parameters. Most past studies have focused solely on the presence of liquid water, and have labeled such as melt. The presence of liquid water is clearly seen as a drop in the backscatter. The distinction of melting from refreezing has received little attention. While a simple drop in the backscatter from a normal "dry" value is adequate for the distinction of melt from frozen states, it does not directly handle refreezing. However, by following the change in backscatter with time, and using the previously discussed time-of-day processing method, which increases temporal sampling of images created from tandem QuikSCAT/SeaWinds data, distinguishing melt from refreeze becomes possible. Thus, the change in backscatter over a short time period can be used to separate melt from refreeze. When the surface heat flows into the snow-pack, the
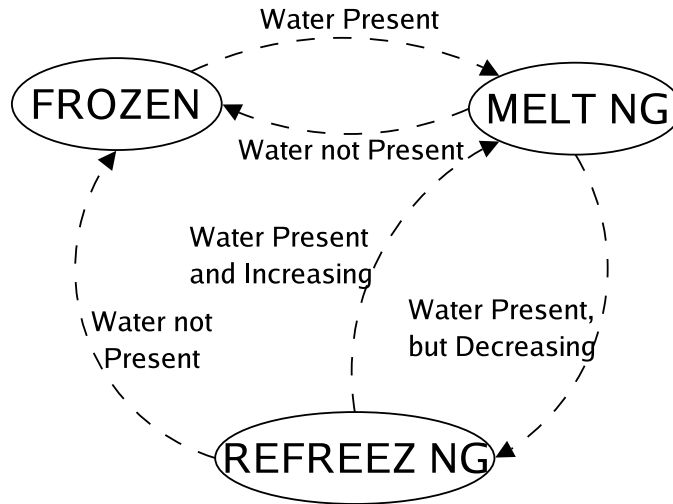
Figure 4.3: Diagram illustrating the three states for an area of snow-pack, and the transitions that can occur.

snow melts, increasing the amount of liquid water present. The increase of liquid water decreases the backscatter of the snow. Likewise, when the surface heat flows out of the snow-pack, the snow refreezes, and the amount liquid water present decreases. Provided the wet snow layer is close enough to the surface to be detected, the backscatter from the snow notably increases. When insufficient liquid water is detected to classify the snow as either melting or refreezing, the snow-pack is frozen.

With the melt, refreeze and frozen states defined, specific criteria for distinguishing between them is needed. A constrained one-step Markov chain model is proposed. The constrained model allows current state knowledge to influence the decision rule used rather than assuming independent samples as is typical for melt detection. Clearly, refreeze cannot be considered unless melt is previously detected. Thus, a Markov chain model, combined with the high sampling frequency make refreeze detection possible. Figure 4.3 shows a diagram expressing the three states and transitions between them. The remainder of this section discusses the decision rules used to determine the ice state and the estimation of melt and refreeze during their respective states.

4.2.1 Frozen State

First, consider the frozen state. There is only one possible transition from this state, from frozen to melting. A threshold is set that is a function of σ^o allowing the separation of the frozen state from melt state. Let $S(t_n)$ represent the state of the ice at time t_n, i.e.

$$
S(t_n) = \begin{cases} 0 & : & \text{frozen} \\ 1 & : & \text{melting} \\ 2 & : & \text{refreezing} \end{cases} . \tag{4.6}
$$

Each state has its own decision rule for determining the next state. The decision rule for determining the state at the next time step, t_{n+1}, is $S_i(t_{n+1})$, where $i = 0, 1, 2$ is the current state: frozen, melting and refreezing respectively. The decision rule when the current state is frozen is

$$
S_0(t_{n+1}) = \begin{cases} 0 & : & q(t) < q_0 \\ 1 & : & q(t) \geq q_0 \end{cases} , \tag{4.7}
$$

where $q(t)$, and q_0 are the metric and threshold, respectively, and have yet to be defined.

In the previous section we outlined the two-layer model, from which the metric and threshold are determined. The method is a modified form of the Q-α method developed by [11]. Melt detection from the frozen state is treated exactly as was done previously by [11], where this method was analyzed and compared to other known melt detection methods. Though there are differences in the dataset between the tandem time-of-day filtered SIR images, and the non-parametric estimate of backscatter using QuikSCAT-only L1B data, similar ability to detect melt is expected. A brief comparison of the new method using tandem data to the Q-α method is given in Section ??. An overview of the derivation follows.

The two-layer model described in the previous section is used to produce a function $q(t)$ and threshold q_0 that are related to σ^o. Combining Equations 4.2, 4.3, and 4.4,

$$
\sigma^o = \alpha^2 \sigma^o_{\text{dry}} + (1 - \alpha^2)\sigma^o_{\text{wet}}. \tag{4.8}
$$

45
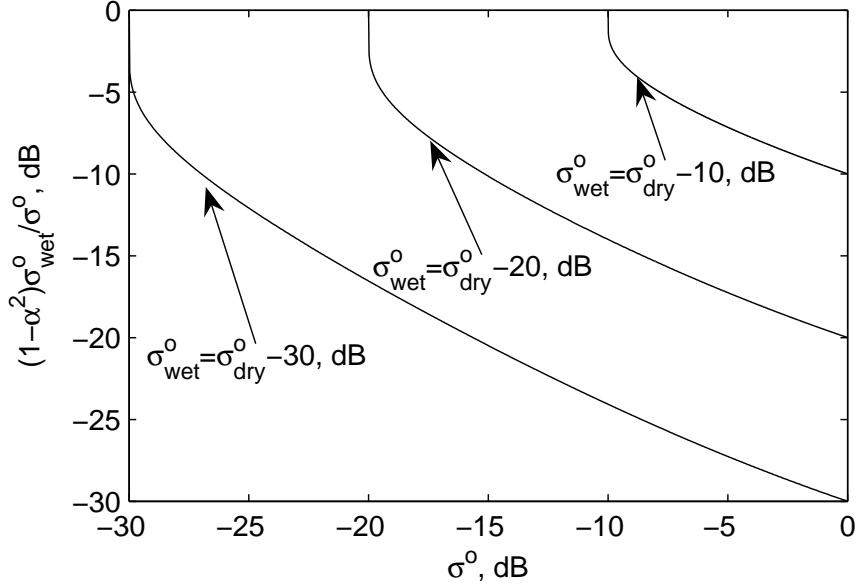
Figure 4.4: The ratio of $(1-\alpha^2)\sigma^o_{\text{wet}}$ to the total backscatter. For small σ^o_{wet} the effect of assuming $\sigma^o_{\text{wet}} = 0$ is negligible.

Because the wet snow is weakly scattering and the backscatter is known to drop by more than 10dB for melting snow, σ^o_{wet} can be considered negligible. Figure 4.4 shows the relative percentage of total backscatter due to $\sigma^o_{\text{wet}} \neq 0$, giving the relative error induced in σ^o by this assumption for three values of σ^o_{wet}. For small σ^o_{wet}, the induced error is very small. Using this assumption, Equation 4.8 is reduced to $\sigma^o = \alpha^2 \sigma^o_{\text{dry}}$, which in dB is written,

$$\sigma^o = 20 \log_{10}(\alpha) + \sigma^o_{\text{dry}}. \tag{4.9}$$

Rearranging gives $-20 \log_{10}(\alpha) = \sigma^o_{\text{dry}} - \sigma^o$. By setting a threshold value for α, the metric, $q(t) = \sigma^o_{\text{dry}} - \sigma^o$ and threshold, $q_0 = -20 \log_{10}(\alpha_0)$, is obtained. The threshold, $q_0 = 3$ dB is used, as used by [11], which corresponds to a depth of 2.4 cm for snow with a m_v of 1.0%, grain size of 0.75 mm, $\rho_s = 0.4$ g/cm^3—snow properties that are consistent with observations of Greenland snow [15].

46

4.2.2 Melt State

The melt state has two transitions: one to the refreeze state, the other to the frozen state. While transition directly from melt to frozen is not strictly necessary, the roughly eight hours of time elapsed between samples in the tandem image data time series makes complete refreeze plausible, especially for short melt events. The decision rule for the melt state is,

$$S_1(t_{n+1}) = \begin{cases} 0 & : & q(t) < q_1 \\ 1 & : & r(t) \leq r_0, q(t) \geq q_1 \\ 2 & : & r(t) > r_0, q(t) \geq q_1 \end{cases} \tag{4.10}$$

where $q(t)$ is as defined previously, q_1 is a threshold of this metric, and $r(t)$ and r_0 are a second metric and threshold that are used to distinguish between melt and refreeze. Since the transition from melt to frozen is a special case of the refreeze to frozen transition, q_1 is determined in the next subsection, where the transition to frozen is covered in greater detail.

For the melt state, $r(t)$ and r_0 need to be determined. The difference between the melt and refreeze states is defined by the change of liquid water in the snow. Melt is characterized by increasing liquid water, while refreeze is characterized by decreasing liquid. Since the attenuation in σ^o is related to the amount of liquid water in the snow, the change in backscatter, the sign of $\frac{\partial \sigma^o}{\partial t}$, can be used to determine if melt or refreeze is occurring. Hence, changes in σ^o from sample to sample are used to determine $r(t)$ and r_0. $r(t_n) = \sigma^o(t_n) - \sigma^o(t_{n-1})$ is used as the melt-to-refreeze metric. Were noise not an issue, the simple threshold, $r_0 = 0$ would perfectly distinguish between these two states according to their definitions. In practice, however, noise is a concern. For example, consider a melt event that has reached an equilibrium, i.e. melt concentration and percolation depth is constant. According to the model definition, backscatter in this case is also constant. Noise corrupted σ^o, whether due to noise in the receiver or by unmodeled physical processes, causes the backscatter to vary from sample to sample, introducing possible misidentification. As shown in the next subsection, the formation of frozen snow at the surface occurring during refreeze

causes a rapid increase in backscatter. Since refreeze is more readily apparent than melt in this case, letting $r_0 = k$ where k is some positive constant, increases the probability that continued melt is detected and less likely that refreeze is identified. Therefore, some small k is used to balance the difference in sensitivity between refreeze and continued melt. This constant is chosen in the next subsection where the sensitivity to refreeze is discussed in greater detail.

In Section 4.1, the two layer electromagnetic model for melt is defined by three parameters: σ^o_{wet}, σ^o_{dry}, and α. The first two of these parameters, σ^o_{wet} and σ^o_{dry}, are defined by the properties of the snow when completely wet and dry, respectively. The parameter α is a variable that depends on the depth of the wet snow. This parameter can theoretically be used to infer melt severity. Returning to Equation 4.8, we solve for α^2,

$$\alpha^2 = \frac{\sigma^o - \sigma^o_{\text{wet}}}{\sigma^o_{\text{dry}} - \sigma^o_{\text{wet}}}. \tag{4.11}$$

Expressed in dB, this becomes

$$20 \log_{10}(\alpha) = [\sigma^o - \sigma^o_{\text{wet}}]_{\text{dB}} - [\sigma^o_{\text{dry}} - \sigma^o_{\text{wet}}]_{\text{dB}}. \tag{4.12}$$

Since $\alpha = e^{-\kappa_{e,\text{wet}} \sec \theta_w d}$, $20 \log_{10}(\alpha) = -20 \, \kappa_{e,\text{wet}} d \, (\log_{10} e) \sec \theta_w$, Equation 4.12 becomes,

$$\kappa_{e,\text{wet}} d = \frac{\cos \theta_w}{20 \log_{10} e} \left([\sigma^o_{\text{dry}} - \sigma^o_{\text{wet}}]_{\text{dB}} - [\sigma^o - \sigma^o_{\text{wet}}]_{\text{dB}} \right). \tag{4.13}$$

Let $\chi = \kappa_{e,\text{wet}} d$, which has units of neper (Np). No attempt is made to infer the actual melt depth d, because the extinction coefficient for the wet snow $\kappa_{e,\text{wet}}$ is an unknown parameter that depends on the physical properties, especially m_v, a parameter which depends on the spatial location and on the severity of melt itself. Together, $\kappa_{e,\text{wet}} d$, and thus χ, capture all the parameters of the two-layer model that are affected by the severity of melt, except perhaps σ^o_{wet}. Because of the relationship of χ to the severity of melt, χ is referred to as the melt severity index (MSI). This index depends only on the relationship of σ^o to σ^o_{dry} and σ^o_{wet}.

Since σ^o_{wet} is unknown and σ^o is corrupted by noise, σ^o_{wet} is assumed equal to zero in the computation of χ.
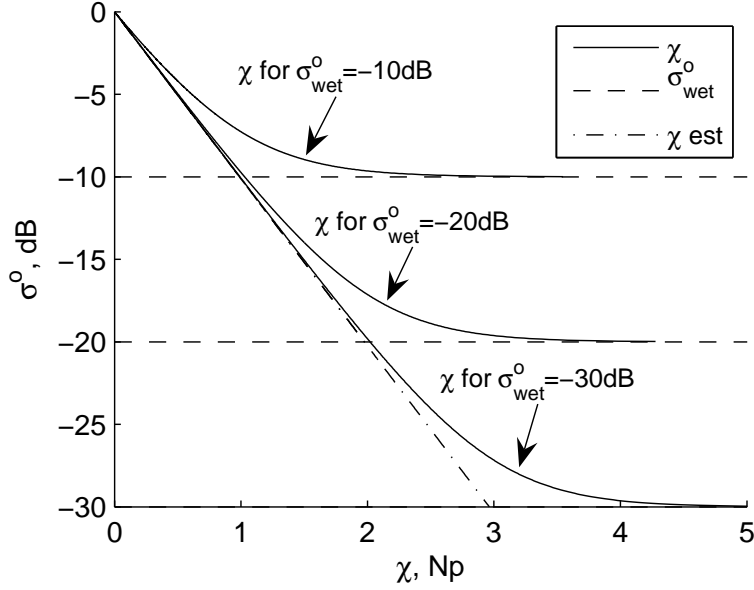
Figure 4.5: The relationship between the MSI, χ, and σ^o, when the value of σ^o_{wet} is modeled, as well as the MSI when $\sigma^o_{wet} = 0$. Note that χ when $\sigma^o_{wet} = 0$ is underestimated, especially for small σ^o.

From Equation 4.13, it is noted that for $\sigma^o = \sigma^o_{wet}$ results in a division by zero. This causes several problems. First, σ^o_{wet} limits the minimum backscatter, and increases the sensitivity of χ to noise as $\sigma^o \to \sigma^o_{wet}$. Second, σ^o_{wet} depends on unknown snow parameters. Lastly, σ^o_{wet} has some dependence on the melt concentration m_v, and therefore is dependent on melt severity. Rather than attempt to model this parameter, σ^o_{wet} can be assumed equal to zero. This makes χ saturate as $\sigma^o \to \sigma^o_{wet}$. Thus for heavy melt, χ depends on the unmodeled σ^o_{wet}. This limits and compresses the MSI at high melt, though MSI still follows changes in the snow parameters that are indicative of melt severity. Setting $\sigma^o_{wet} = 0$, Equation 4.13 becomes

$$\chi(t) = \frac{\cos \theta_w}{20 \log_{10} e} \left(\sigma^o_{\text{dry}} - \sigma^o(t) \right). \tag{4.14}$$

Several issues exist that make the MSI imperfect. First, noise corrupts σ^o and thus χ. Second, the model does not account for snow stratification, lumping the backscatter contribution from all these layers into a single parameter σ^o_{dry}. This parameter may vary during the course of the season, because the stratified layers of

49

snow are altered most significantly during the melt season. Many layers are completely changed or disappear as melt and vapor transport occurs. Heterogeneity of the snow may therefore introduce a bias. Third, choosing to not model σ^o_{wet}, clearly makes χ non-linear with respect to melt severity, as well as variable across snow types. MSI, however, represents a good indicator of melt severity, without requiring *a priori* information about the snow and melt. Of course, improvements can be made to the MSI if further information about the snow can be obtained, especially if σ^o_{wet} can be better modeled.

4.2.3 Refreeze State

Next, the refreeze state is considered. This state is perhaps the most complicated of the three states, since the three layer model is used. The decision rule is

$$
S_2(t_{n+1}) = \begin{cases} 0 & : \quad q(t) < q_1 \\ 1 & : \quad r(t) \leq r_0, q(t) \geq q_1 \\ 2 & : \quad r(t) > r_0, q(t) \geq q_1 \end{cases} \quad . \tag{4.15}
$$

Since $r(t)$ and $q(t)$ are already defined, all that is left to do is determine q_1 and r_0. Before these parameters are defined, how the parameters of the three-layer model are affected by σ^o need to be discussed, from which both metrics $q(t)$ and $r(t)$ are defined.

The equation for backscatter in the three-layer model using the assumption that $\sigma^o_{\text{wet}} = 0$ is

$$
\sigma^o = \left[1 - \beta^2 (1 - \psi^2) \right] \sigma^o_{\text{dry}}. \tag{4.16}
$$

Using $\chi = \kappa_{e,\text{wet}} d_m$, $\xi = \kappa_{e,\text{wet}} d_r$, $\gamma = \kappa_{e,\text{dry}}/\kappa_{e,\text{wet}}$ and $\sec \theta_d = \sec \theta_w = \nu$, we can write β and ψ as functions of χ, ξ, γ and ν:

$$
\beta = e^{-\gamma\nu\xi}, \tag{4.17}
$$

$$
\psi = e^{-\nu(\chi-\xi)}, \tag{4.18}
$$

where χ is the MSI estimated during the last melt state, ξ is a parameter similar to χ, and a theoretical measure of the thickness of frozen snow above the wet subsurface

layer, while γ, and ν are constants. The parameter, ξ, is referred to as the refreeze severity index (RSI).

Like the MSI, the RSI suffers from several problems that make it difficult to obtain. First, when γ, χ, and ν are held constant, both β and ψ are dependent on ξ; thus, this index is not explicitly invertible. It is one-to-one, however, and can easily be inverted numerically, using the well-known Newton-Raphson method, which is known to converge quadratically, when it converges. Although a more sophisticated technique could be used, adequate results are obtained when a near-zero $\chi/2$ is used, as long as γ is sufficiently greater than zero. For realistic values of γ, i.e. $\gamma > 10^{-8}$ and a near-zero of $\chi/2$, no convergence problems are observed.

Second, the RSI depends on the knowledge of γ and ν. While ν is practically constant regardless of the type of snow, γ depends on the snow parameters. Figure 4.6 shows the refreeze index ξ vs $\sigma^o - \sigma^o_{\mathrm{dry}}$ for various initial values of χ_{melt}. As the initial melt increases ξ becomes increasingly non-linear, particularly for large χ_{melt} and small ξ where large changes in σ^o drive small changes in ξ. The degree of non-linearity is largely dictated by the extinction ratio γ. For small γ, the nonlinear effect appears only for large χ_{melt}, and the onset of this non-linear behavior is less severe. Large γ causes the nonlinearity to be much more severe, and appear at smaller initial melt values. Since the extinction coefficients are dependent on the parameters of the snow, explicitly setting γ makes this model suffer from additional error over snow types where γ is different than the model.

Despite the inconsistency of non-linear effects in ξ across varying snow types, the RSI is not overly sensitive to the exact snow parameters. Figures 4.7, 4.8, and 4.9 show how grain-size, r, water concentration, m_v, and snow density, ρ_s, affect the response of ξ with respect to the observed σ^o. Snow grain size has the largest effect, followed by moisture concentration and snow density respectively. Since snow grain size is quite variable across the snow-pack, the exact response of ξ to refreeze suffers from modeling error. However, qualitative behavior between σ^o and ξ is similar regardless of the exact choice for γ. In warmer, more frequently melting regions the snow has larger grains, larger γ, and thus more non-linearity in the refreeze index.

51
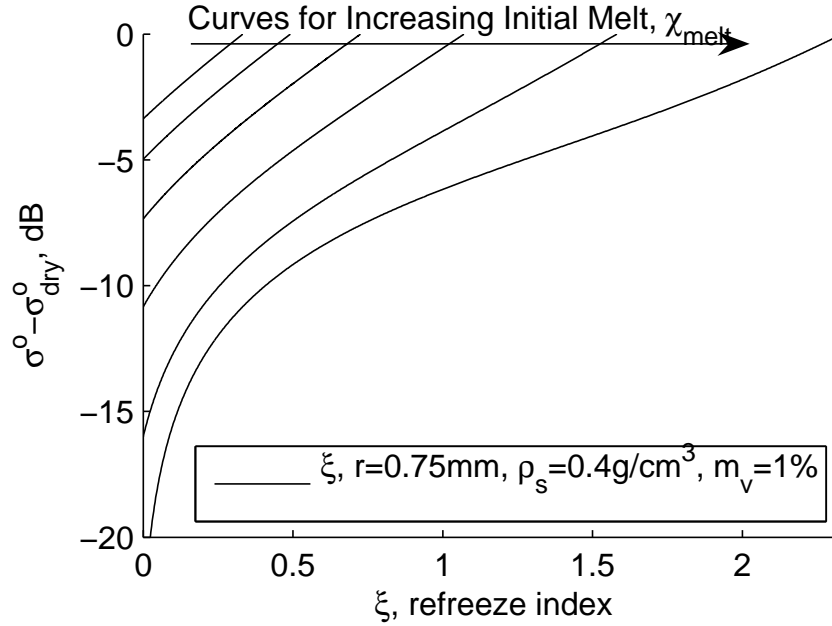
Figure 4.6: The relationship between RSI, ξ, and $\sigma^o - \sigma^o_{\mathrm{dry}}$ for various initial values of χ_{melt}. The dry snow has a grain size, $r = 0.75\mathrm{mm}$, density $\rho_s = 0.4$ g/cm^3, resulting in a relative permittivity of $\epsilon_{r,\mathrm{dry}} = 1.53$, and extinction coefficient of $\kappa_{e,\mathrm{dry}} = 1.20$. The wet snow has the same grain size, and density with moisture content, $m_v = 1\%$, resulting in $\epsilon_{r,\mathrm{wet}} = 1.57 - j3.35 \times 10^{-2}$, and $\kappa_{e,\mathrm{wet}} = 12.12$. Permittivity is estimated using a modified Debye-like model [32]. Scattering coefficients are estimated using a method involving spherical ice inclusions in an air/water background where permittivity is determined by the Polder-Van Santen mixing formula [32]. Note that as the initial melt depth, χ_{melt}, increases, ξ becomes increasingly non-linear.

In these regions the effective refreeze depth is likely overestimated. In drier, cooler regions, the grain size is smaller, causing the refreeze index to be underestimated. However, cooler regions are also less likely to experience severe melt; thus, melt in these regions remains within the more linear region of the response curves.

With the effect of the three-layer model on backscatter described, the threshold values of q_1 and r_0 can be defined. A second threshold for the metric measuring water content, q_1, is used for the transition back to the frozen state, rater than reusing q_0. The second threshold, q_1 is used because continuation of melt or beginning of refreeze is probable following the detection of melt. Allowing q_1 to be less than q_0 takes the

Figure 4.7: The RSI, ξ, verses $\sigma^o - \sigma^o_{\text{dry}}$ with initial values of $\chi_{\text{melt}} = 0.33, 1.33$, and 2.33, and with changing grain sizes at 20% increments. Grain size has a considerable effect on $\kappa_{e,\text{dry}}$ most significantly increasing γ as r becomes larger.

increased probability of these occurring into account. Moreover, from the behavior shown in Figures 4.6, 4.7, 4.8, and 4.9, setting $q_1 = q_0$ would significantly limit the maximum observable ξ. Thus, the model sets $q_1 = 1\text{dB}$ to insure that most of the refreeze process is accounted for, while also keeping the threshold far enough away from σ^o_{dry} to keep misclassification due to noise under control. Figure 4.10 shows the maximum percent of total refreeze that is observable using $q_1 = 1\text{dB}$ with the various grain sizes. Naturally, the maximum observable ξ depends on other snow parameters, such as moisture content in the wet layer, and density; however, the small effect that grain size has on the maximum observable ξ suggests that these have negligible impact. None of the snow parameters has much effect on the maximum observable ξ for small initial χ, where the percent of observable melt is at a minimum.

The value of r_0 is chosen with several aspects in mind. As mentioned in Section 4.2.2, making $r_0 = k$ where k is some positive constant, increases the probability that continued melt is detected and less likely that refreeze is identified. For long periods
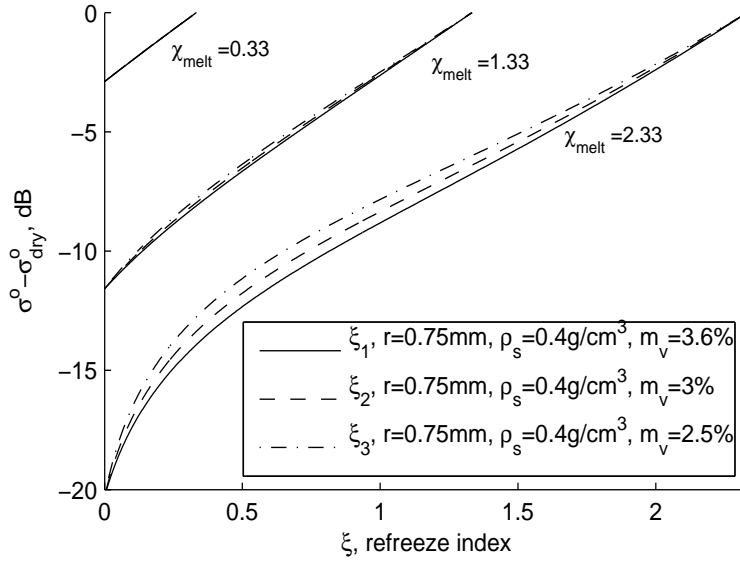
Figure 4.8: The RSI, ξ, vs. $\sigma^o - \sigma^o_{\text{dry}}$ with initial values of $\chi_{\text{melt}} = 0.33, 1.33$, and 2.33, and with changing melt concentrations at 20% increments. Melt concentration has a small effect on $\kappa_{e,\text{dry}}$ decreasing γ as m_v becomes larger.
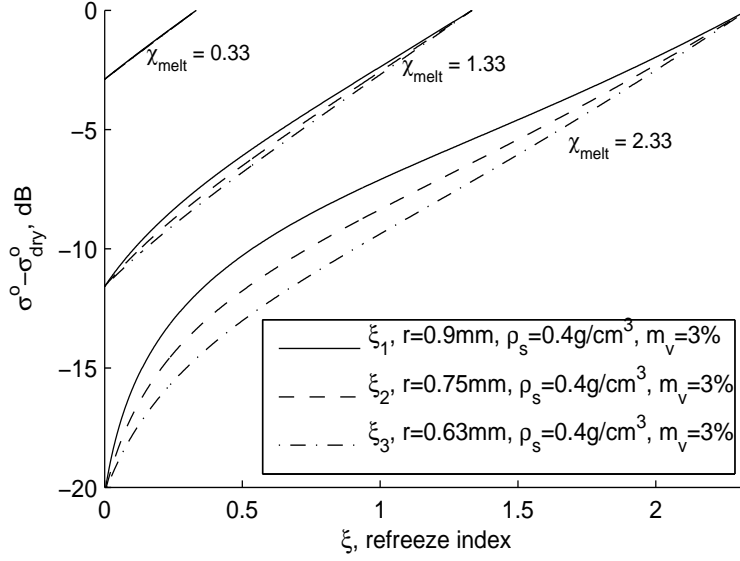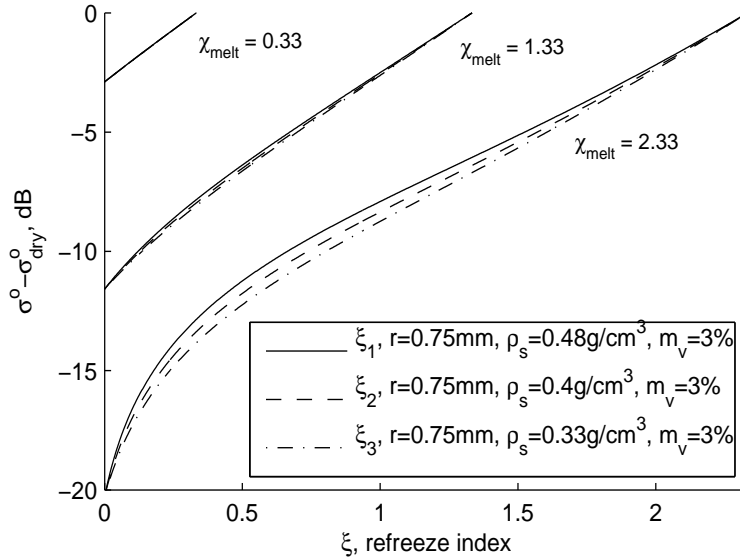

Figure 4.9: The RSI, ξ, vs. $\sigma^o - \sigma^o_{\text{dry}}$ with initial values of $\chi_{\text{melt}} = 0.33, 1.33$, and 2.33, and with changing snow densities at 20% increments. Snow density has a small effect on $\kappa_{e,\text{dry}}$ increasing γ as ρ_s becomes larger.
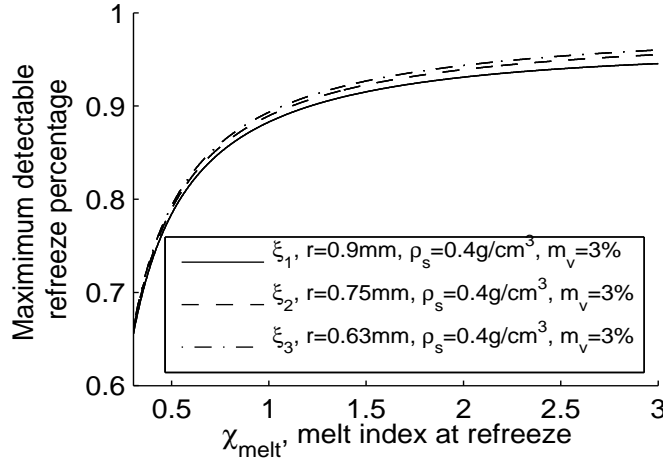
Figure 4.10: The maximum percent of refreeze observable with a refreeze threshold q_1=1dB for various χ_{melt}, and for grain sizes at 20% increments. Grain size has a small effect on the maximum percent of observable refreeze. Melt concentration and snow density changes have negligible effect on observable refreeze.

of nearly constant melt, the liquid water in the snow reaches an equilibrium, and as a result, σ^o does as well. Thus in periods of constant melt, the change in σ^o will be entirely due to noise. Making $r_0 = 0$ would cause frequent identification of refreeze when melt should have been detected. As shown in the behavior of ξ with σ^o in Figures 4.6, 4.7, 4.8, and 4.9, small changes in the RSI at the onset of refreeze require large increases in σ^o. Because σ^o is very sensitive to refreeze onset, changing $k > 0$ allows improved identification of melt during periods of continual melt without significant adverse effect on the ability to properly identify refreeze when it occurs. Figure 4.11 shows the minimum percentage of refreeze that can be observed for various values of k and χ_{melt}. This percentage is greatest for small χ, and is practically independent of the snow parameters. We let $k = 0.5$dB, which appears to be an acceptable threshold in the simulation experiments described in Section 4.3.

To summarize, the final decision rule for governing state change is shown in Table 4.2.3.

Table 4.1: The decision rule for state change, from current state $S(t_n)$ to next state $S(t_{n+1})$, written in terms of $\sigma^o(t_n)$, and $\sigma^o(t_{n+1})$.

$S(t_n)$ / $S(t_{n+1})$	Frozen	Melting	Refreezing
Frozen	$\sigma^o(t_{n+1}) > \sigma^o_{\mathrm{dry}} - 3\mathrm{dB}$	$\sigma^o(t_{n+1}) > \sigma^o_{\mathrm{dry}} - 1\mathrm{dB}$	$\sigma^o(t_{n+1}) > \sigma^o_{\mathrm{dry}} - 1\mathrm{dB}$
Melting	$\sigma^o(t_{n+1}) \leq \sigma^o_{\mathrm{dry}} - 3\mathrm{dB}$	$\sigma^o(t_{n+1}) \leq \sigma^o_{\mathrm{dry}} - 1\mathrm{dB}$ $\sigma^o(t_{n+1}) < \sigma^o(t_n) + 0.5\mathrm{dB}$	$\sigma^o(t_{n+1}) \leq \sigma^o_{\mathrm{dry}} - 1\mathrm{dB}$ $\sigma^o(t_{n+1}) < \sigma^o(t_n) + 0.5\mathrm{dB}$
Refreezing	—	$\sigma^o(t_{n+1}) \leq \sigma^o_{\mathrm{dry}} - 1\mathrm{dB}$ $\sigma^o(t_{n+1}) \geq \sigma^o(t_n) + 0.5\mathrm{dB}$	$\sigma^o(t_{n+1}) \leq \sigma^o_{\mathrm{dry}} - 1\mathrm{dB}$ $\sigma^o(t_{n+1}) \geq \sigma^o(t_n) + 0.5\mathrm{dB}$

4.3 Geophysical/Electromagnetic Model Simulation

In order to illustrate the use of the proposed detection and estimation method, a simple geophysical/electromagnetic model is developed next. There are many examples of geophysical models in the literature [34, 35, 36, 37]. These models vary in their purpose: energy and mass balance are typical applications. In this section, a simplified geophysical model is developed based on these previous works, to which a model for electromagnetic backscatter is added. This geophysical model is initialized using typical snow parameters, and driven with a realistic heat input to determine the effect of melt on backscatter. The resulting backscatter model supports testing and verification of the new melt detection and estimation method.

4.3.1 Geophysical Model

The geophysical snow-ice model is a multi-layered one-dimensional model that handles the thermodynamic properties, water percolation, and to a limited extent the metamorphism and settling of the snow-pack. A one-dimensional equivalent model is considered reasonable in this application because the area footprint of a single pixel
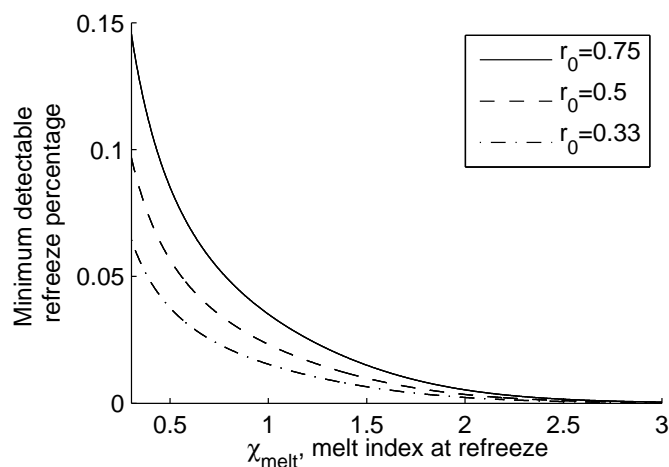
Figure 4.11: The minimum percent of refreeze that is observable with various amounts of r_0, plotted against χ_{melt}.

is very large compared to the vertical extent of the model. The layers of the model, which are control volumes with constant properties, are illustrated in Figure 4.12. The physical properties of the control volumes obey the law of conservation of energy and mass, which governs the temperature as well as the formation and flow of liquid water. For each time step in the model, the model algorithm has several steps. A block diagram of the algorithm is shown in Figure 4.13. Each step consists of,

1. Thermodynamic diffusion governed by the heat diffusion equation and driven by a surface heat source,

2. Melt determined by the energy required to heat each control layer above 0 C,

3. Settling,

4. Percolation,

5. Combining small control volumes, and creating new volumes to maintain model depth,

6. Re-evaluation of snow properties such as thermal conductivity, fluid permeability, etc., and

57

7. Application of the electromagnetic model.

The thermodynamic portion of the model is governed by the heat diffusion equation[1]

$$\frac{\partial T(z,t)}{\partial t} = -\frac{1}{\rho(z)C_p}\frac{\partial}{\partial z}\left(\lambda(z)\frac{\partial T(z,t)}{\partial z}\right), \tag{4.19}$$

where $T(z,t)$ is temperature at depth z and time t, $C_p = 0.21$ J/g K, is the specific heat of snow, and $\lambda(z), \rho(z)$ are, respectively, the thermal conductivity of snow and the snow density at depth z. This equation is discretized and solved iteratively using the widely known Crank-Nicholson implicit method[2]. A Dirichlet boundary is used on the bottom layer, holding the temperature at that node constant. A time-varying heat source is applied at the surface. This heat source is a combination of all the heat transport to and from the atmosphere: convection, radiation, sensible and latent heat flux. While this is an oversimplification—significant heat leaves by vapor transport and forced convection from beneath the surface—this has little effect on backscatter as long as all heat is accounted for.

Next, melt and refreeze are determined. Temperatures greater than 0 C are reduced to 0 C, and the excess heat is used to convert the snow to liquid water. The temperature in excess of 0 C has energy density, $Q_e = \rho C_P(T - T_{0C})$. This energy density results in an increase in the fraction of liquid water. The density of newly melted liquid water is $M_l = Q_e/L_f$ where L_f is the latent heat of fusion, which for water is 334 J/g. For refreeze, layers that have liquid water where the heat diffusion computes temperatures below 0 C, like melt, return the temperature to zero until the layers' water is refrozen.

Percolation is computed by assuming that percolation does not occur until a certain fraction of the snow has melted [38]. Above this saturation concentration, water begins to percolate downward. Percolation obeys conservation of mass, requiring

$$\frac{\partial(\rho\, dV\, m_v)}{\partial t} = -[U_l]_i^{i+1} + M_{li}, \tag{4.20}$$

---

[1]This equation is derived in the Appendix, Section A.1
[2]This method, as it is used to solve the heat diffusion equation, Equation 4.19, is described in detail in the Appendix, Section A.2.
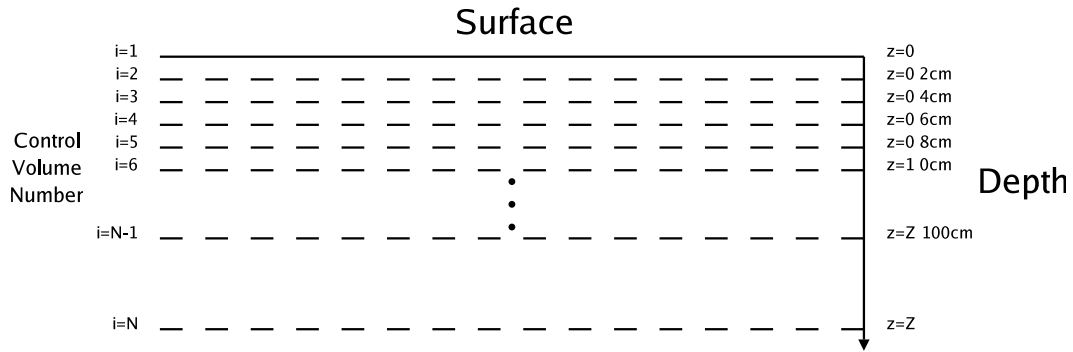
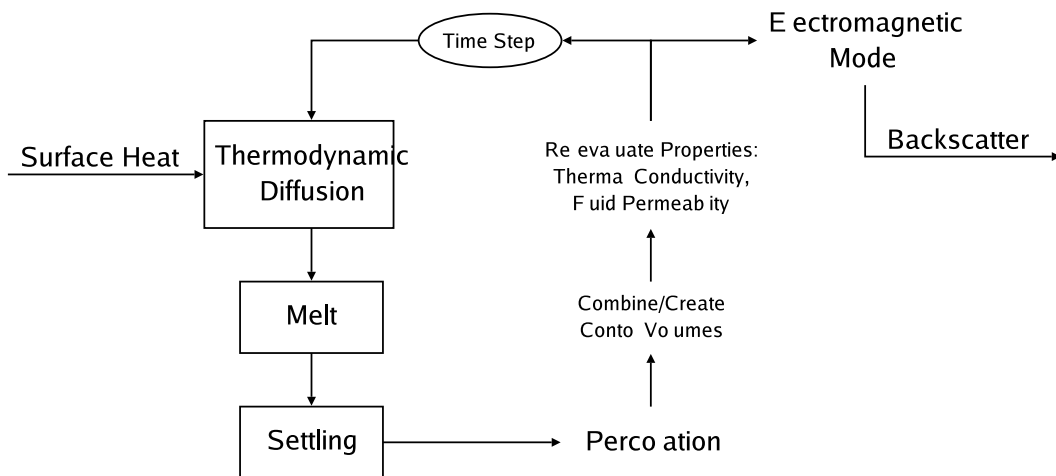Figure 4.12: Diagram of the geophysical/electromagnetic model layers.

Figure 4.13: Diagram showing the geophysical/electromagnetic model algorithm.

where $-[U_l]_i^{i+1}$ is the vertical water flux evaluated at the control volume surfaces, M_{li} is the liquid-to-ice flux, with

$$U_l = \frac{\rho_w}{\mu_w} g K_{\max} \left[\frac{s - s_r}{1 - s_r} \right]^3, \qquad (4.21)$$

where $\rho_w = 1.0\text{g/cm}^3$ is the density of pure water; $\mu_w = 10^{-6}$ m^2/s is the kinematic viscosity of water, g is the gravity acceleration; $K_{\max} = 0.077d^2 \exp\left(-7.8\frac{\rho_s}{\rho_w}\right)$ is the intrinsic snow permeability; d is the grain size; $s = \frac{v_l}{1-v_s}$ is the water saturation; $v_l = \rho_l/\rho_w$ is the specific volume of liquid water; $v_s = \rho_s/\rho_i$ is the specific volume of ice; $\rho_i = .917$ g/cm^3 is the density of pure ice; and s_r is the residual water saturation [38].

The downward flow of water in this model is spatially uniform, which for the purpose of bulk modeling is adequate. It is noted, however, that the actual flow pattern is quite irregular, forming fingers and channels which cause the leading edge of melt to disperse. It is also conceivable that variable densities typical in a realistic snow pack may lead to horizontal flow. A model would be drastically more complicated to handle such behavior and requires more *a priori* information than is available, thus fingering is ignored. Because of the scale of the measurement footprint, a statistical equivalent model is used; thus, the percolation and resulting effect on σ^o is considered in the average sense.

The residual water saturation, s_r, is a critical parameter which determines the minimum water saturation that must be present for percolation to occur. Different values are found throughout the literature, generally between 0.02 and 0.1 [34, 36, 37]. The model sets $s_r = 0.065$—though other values are considered—which results in a m_v between 3–5% for typical melt conditions and firn densities. The residual water saturation and thereby the liquid water content of the snow, has a profound effect on the absorption coefficient, κ_a, during melting conditions. The effect of s_r parameter on the backscatter is discussed further in section 4.3.3.

The algorithm used for settling, densification, and snow metamorphism is very simple. When a portion of the snow melts in a control volume, the layer thickness is decreased so the snow fraction density stays the same. Thus, melting causes the

snow to settle. Densification occurs as the melt refreezes, where the liquid fraction is added to the snow fraction. This is the only mechanism for densification. Grain size is held constant. Choosing to not model grain growth because of the complexity of current state-of-the-art models, simplifies the model. While grain size has an effect on the backscatter, during a short melt event this effect is only expected to increase the final backscatter by some several tenths of a dB. While the exact backscatter will be somewhat different than what the model predicts due to this simplification, the overall behavior of the backscatter given by the model is relatively unaffected.

Layers that have become too thin due to melt, are combined. The three nearest layers including the thin layer being deleted are combined into two equal layers, each taking half of the thin layer. The combination of three layers into two is done because the sensitivity of the backscatter model to the combination of these layers. Small discontinuities in the backscatter are seen before and after the combination of these layers. However, the discontinuity of combining three layers into two is much less than combining two into one. Layers near the surface—within the top 30 cm—are initially 0.2 cm thick. When a layer becomes thinner than 0.1 cm thick, layers are combined. These layers are much thinner than typically used in one-dimensional snow models [36, 37]; however, σ^o is very sensitive to the electrical properties in the top several centimeters of wet snow, requiring thin layers be used. Layers below 30 cm increase in thickness at each step. The bottom-most layer is 1 m thick. When the model depth decreases 0.5 m, a new 1 m layer is added to the bottom.

4.3.2   Model Simulation Initialization

Before the model can be used, a number of initial conditions are needed. The thermodynamic diffusion portion of the model requires specification of the snow density, $\rho_s(z)$, the temperature, $T(z,0)$, the thermal conductivity, $\lambda(z)$, and the surface heat flux. Typical snow-pack densities are known to increase with depth due to over-burden densification [15]. An initial density at the surface of 0.36 g/cm^3 is assumed and the density increases with depth [15]. Figure 4.14a shows the initial density as a function of depth. Thermal conductivity of snow depends on a number of physical

Figure 4.14: Initial geophysical model parameters

(a) Density

(b) Thermal Conductivity
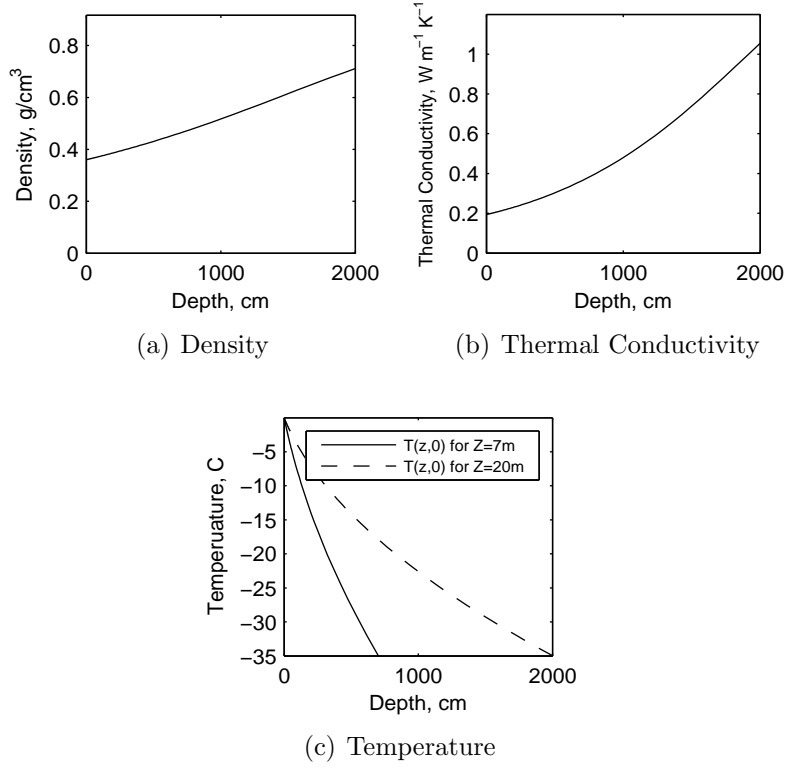
(c) Temperature

properties of the snow. For simplicity, a quadratic regression model derived by [39] is used where, $\lambda = 0.138 - 1.010\rho_s + 3.233\rho_s^2$ W/mK. Using the snow density shown in Figure 4.14a, the thermal conductivity is computed and shown in Figure 4.14b. The temperature profile is initialized according to,

$$T(z,0) = T_\infty + (T_\infty - T')\sqrt{\frac{z + z'}{Z + z'}}, \qquad (4.22)$$

where $T_\infty = -35$ C is the temperature at ultimate model depth Z, T' is chosen so the top layer is 0 C, and $z' = 1$ m is used to insure that the gradient $\frac{\partial T}{\partial z}$ is bounded at $z = 0$ and the solution remains smooth for $t > 0$. Figure 4.14c shows the initial temperature profile as a function of depth. All model parameters are constant across each control volume.

The thermal model requires a heat input to drive the melting process. This model uses a single heat source applied at the upper surface of the model. This

source is a combined heat source representing all the heat flux exchanged with the atmosphere (e.g. solar, IR, sensible and latent heat flux, etc.). In the experiments that follow two heat sources are used, a constant heat flux, and an offset sinusoidally varying heat flux. The sinusoidally varying heat flux is $\Phi_Q = 0.75 + 5\sin\frac{\pi}{7}t + 7\sin 2\pi t$, W/m^2, where t is in days. The offset is needed to maintain the average temperature of the snow near the surface. Without the 0.75 W/m^2 offset, heat transfer to the depths of the model would cause the surface temperature to drift away from 0 C. Thus, the offset helps maintain the model near melting conditions. The sinusoidal input of heat flux consists of two sinusoids with different periods, a high amplitude sinusoid with a period of one day representing diurnal heat fluxes, and a medium amplitude sinusoid with a period of 14 days representing change in heat flux due to large scale weather patterns. This simulates a 14 day long period with diurnal variation and a major storm front in the summer months similar to that seen in tandem QuikSCAT/Seawinds and AWS data from JD 152 to JD 170, 2003 at the ETH Swiss camp shown later in Figures 5.1 and 5.4.

4.3.3   Electromagnetic Model

The electromagnetic backscatter model uses the snow state to estimate the vertically-polarized normalized radar cross-section of the snow viewed at or near the Brewster angle, as assumed in Section 4.1. This is done so surface and inter-layer reflections are negligible. The model attempts to estimate the backscatter using Equation 4.1, restated here for convenience,

$$\sigma^o = \int_0^\infty \gamma(z)e^{-2\tau(0,z)}\sec\theta(z)\mathrm{d}z. \tag{4.23}$$

Since the magnitude of the permeability is relatively constant with depth, the term $\sec\theta(z) = \sec\theta \approx 1.1656$ can be moved out of the integral. This leaves two unknowns, the volume contribution $\gamma(z)$ and the attenuation $e^{-2\tau(0,z)}$.

Attenuation is estimated using a radiative transfer model. Using a radiative transfer model, the optical depth of the snow-pack is

$$\tau(0,z) = \sec(\theta)\int_0^z \kappa_e(z')\mathrm{d}z'. \tag{4.24}$$

63

The extinction coefficient κ_e is a function of the physical parameters of the snow. The extinction coefficient is the sum of the scattering coefficient and the absorption coefficient, $\kappa_e = \kappa_s + \kappa_a$. Absorption coefficients are estimated using a modified Debye-like model [32] to obtain the complex permittivity of the snow, ϵ_r. Thus, absorption is related to permittivity by

$$\kappa_a = 2\frac{2\pi f}{c}\Im\{\sqrt{\epsilon_r}\}, \tag{4.25}$$

where f is the frequency, c the speed of light in a vacuum, and $\Im\{\cdot\}$ denotes the imaginary part. The scattering coefficient is found by modeling the snow grains using independent mie-scattering of spherical ice inclusions in an air background. While better scattering models, which incorporate the interaction of scattered waves between scatterers, exist, these models require additional information such as surface correlation length, which is unknown at most locations. The scattering coefficient is assumed constant with water content. The snow density ρ_s, the grain size r, and the liquid concentration m_v are inputs to the model. The extinction coefficient for various snow densities and grain sizes are plotted against m_v in Figure 4.15. Since the extinction is dominated by the absorption as m_v gets large, the other snow parameters affect the optical depth at only small m_v. Once the extinction coefficient is known for each control volume, the integral of the equation is estimated using the extended Simpson's rule for each depth. Once τ is determined, the attenuation follows.

The remaining unknown in Equation 4.23 is the volume backscatter contribution, $\gamma(z)$. For dry snow, the volume contribution is assumed to be proportional to the scattering coefficient κ_s. The volume contribution to backscatter is much more difficult to determine when the volume contains liquid water. For the sake of simplicity, wet snow volume backscatter is assumed independent of water content. While water concentration has an effect on the overall scattering efficiency, absorption is assumed to dominate the backscatter, thus the liquid water fraction is modeled as an absorbing medium in an otherwise unchanged scattering medium. The effect on the grain shape that adding liquid water has on the backscatter is ignored, treating it negligible.
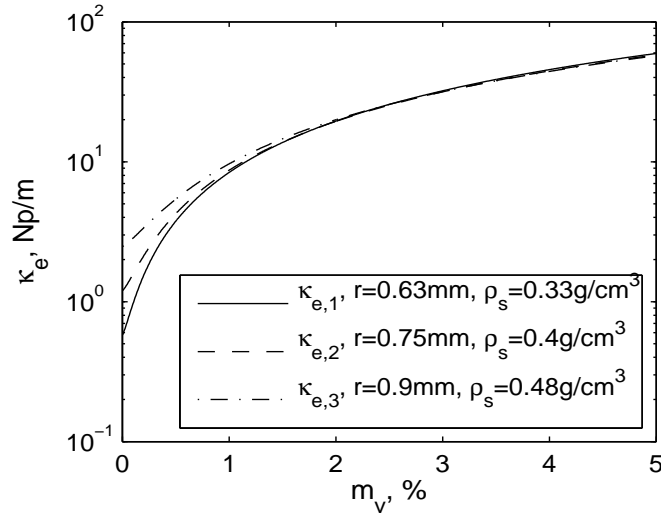
Figure 4.15: Extinction coefficient κ_e as a function of m_v for various snow parameters.

In Section 4.2 the backscatter contribution from the wet snow is modeled as zero, i.e. $\sigma^o_{\text{wet}} = 0$. In this geophysical model, the volume scattering contribution, $\gamma(z)$, is assumed to be the same for wet as for dry snow. This clearly contradicts the $\sigma^o_{\text{wet}} = 0$ assumption used for the melt and refreeze severity indexes. However, in Section 4.2 the contribution from the wet snow is ignored because this parameter is unknown. Since σ^o_{wet} is a function of snow parameters that change with time, ignoring σ^o_{wet} in the two and three layer models was a compromise to make computation of the MSI and RSI parameters tractable. Since the simulation controls many of the snow parameters that affect σ^o_{wet}, this simplification is unnecessary here.

While this geophysical/electromagnetic model is very simple, it produces reasonable results. The experiments explained in the next subsection show good agreement with tandem QuikSCAT/SeaWinds backscatter measurements taken at the ETH Swiss Camp shown later in Figures 5.1 and 5.4, and seen in σ^o images across the ice-sheet. While clearly the exact results—backscatter, moisture content, melt depth, heat flux, etc.—are inexact due to the simplifications employed, the qualitative behavior of the model follows the observed measurements quite well.

4.3.4 Simulation Results

With groundwork for the simulation model complete, two experiments are conducted and their results discussed. The goal of the first experiment is to test the assumption stated in Section 4.1 that the melt depth d_m during the refreeze has only a relatively small effect on the backscatter, and thus χ can be assumed constant during refreeze. The second experiment is conducted to see how the MSI and RSI, using the model setup described, follow the melt through a simulated melt event in the percolation zone in Greenland.

The first model experiment tests the assumption that χ changes slowly for large melt events. To conduct this experiment, a constant heat flux of 5 W/m^2 into the surface is imposed on the model with initial parameters stated above, using an ultimate depth of the model $Z = 20$ m. The heat is allowed to penetrate the surface for 6 days, causing melt and percolation to occur. The depth of this melt depends on the residual water saturation, s_r. Though the mass of water melted is the same, s_r determines how concentrated the water is in the wet snow layer. To evaluate the effect that the residual water saturation, s_r, has on the backscatter and the time to refreeze, two values are considered, $s_r = 6.5\%$ and 3%. After applying the constant 5 W/m^2 heat flux to the surface of the modeled snow for six days, the heat flux is changed to 0 W/m^2 and a day is allowed to permit the percolation process to complete before backscatter measurement begins. Heat flux at the surface remains at 0 W/m^2 for the duration of the backscatter measurement. By setting the heat flux at $\Phi_Q = 0$ W/m^2, the refreezing of the wet snow is forced to propagate from beneath the wet snow layer upward, with no refreeze occurring at the surface.

Figure 4.16 shows the outcome of the first experiment. The integrated amount of liquid water beneath the surface at $t = 0$ when the backscatter measurement begins is 0.49 cm w.e. Note that the water in the snow is modest, resulting in melt depths of 23.7 cm and 12.2 cm for $s_r = 0.03$ and $s_r = 0.065$, respectively, yet it takes 8 to 12 days for a measurable change in backscatter to occur when refreeze is propagating only from the beneath the wet snow. Since the time to refreeze observed in backscatter measurements of Greenland are much shorter than this, most of the refreeze must be
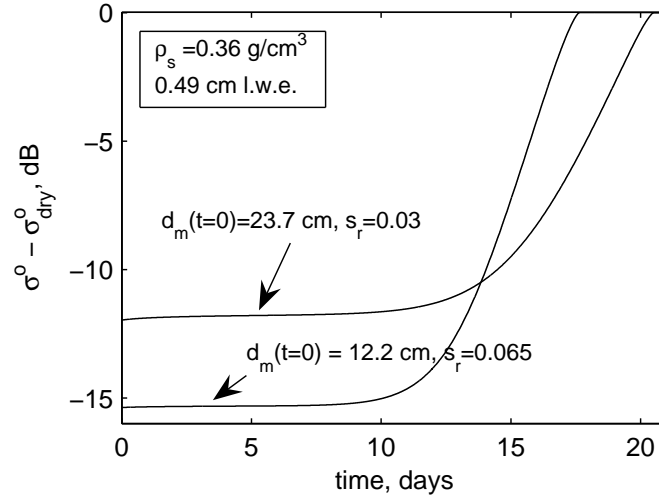
Figure 4.16: Outcome of the first experiment. The heat input at the surface is held at zero, while refreeze of the 4.90 km/m² of liquid water is refrozen by heat transfer deeper into the snow. The ultimate depth of the model is $Z = 20$m.

originating at, and propagating from, the surface. This makes the assumption that χ is constant during refreeze is quite reasonable.

The temperature profile and the melt depth and mass are chosen to be consistent with expected conditions in the percolation zone, where melt is moderate. The temperature gradient in the wet snow zone is considerably more shallow. At the location of the ETH Swiss camp where the AWS data is taken in Chapter 5, the temperature below 10m is approximately constant at -8.5 C [40], producing a temperature gradient much more shallow than the one used in the experiment. Moreover, the depth and quantity of melted water in this zone is much greater. Were this experiment repeated with melt and temperatures more consistent with those of the ETH camp, the time elapsed before a notable change in backscatter would be considerably longer than 8–12 days. This is not observed in σ^o data, therefore surface refreeze propagation must dominate.

Note a second observation made during the first experiment: σ^o, and thereby χ, saturates at relatively small melt depths. While the first experiment validates the assumption that χ is constant during refreeze by this observation, it is not clear from

this experiment if χ is a useful MSI for any more than light melt. To understand the effect that changing melt conditions have on χ, a second experiment is conducted.

The second experiment attempts to simulate a melt event using a realistic heat input. The heat input used is the offset sinusoidally varying heat flux described in Section 4.3.2. The residual water content is set to $s_r = 0.065$ and the ultimate depth of the model to $Z = 20$ m and again to $Z = 7$ m to show the effect of increasing the temperature gradient. This experiment is run for 14 days, the fundamental period of the time-varying heat flux. Figures 4.17 and 4.18 show the outcome of this experiment for $Z = 20$ m and $Z = 7$ m respectively. Figures 4.17a and 4.18a show the backscatter with time; Figures 4.17b and 4.18b show the progression of melt into the snow-pack; and Figures 4.17c and 4.18c show the melt concentration in the top 2.5cm of the snow pack.

Several observations are gained by the second experiment. First, note that σ^o saturates during the day when the melt is at its peak. However, the backscatter still varies from day to night during these days, despite the fact that the surface never completely refreezes. Second, note that σ^o closely follows changes in m_v in the top several centimeters of melt. Thus, for light melt, backscatter closely follows the melt depth; but for moderate-to-heavy melt, backscatter follows liquid concentration near the surface. In terms of the model developed in this paper, the MSI follows attenuation due to increasing melt depth for light melt, while for heavier melt is more closely follows σ^o_{wet}, which is a function of m_v and not the melt depth. As a result, the MSI follows the melt severity, though with decreasing sensitivity as the melt becomes more severe. Note also from this experiment that σ^o is very sensitive to refreeze, even for very thin surface refreeze layers.

To show how the MSI and RSI are expected to respond on the tandem QuikSCAT and SeaWinds dataset, σ^o is sampled three times a day, corresponding to the tandem observation sample times, and the new Markov melt detection technique combined with χ and ξ, the MSI and RSI, described in Section 4.2 is used. Figures 4.19 and 4.20 show the χ and ξ for the $Z = 20$ m and $Z = 7$ m respectively. As these figures show, χ increases as the snow pack melts, but saturates. As χ saturates, however,

68

Figure 4.17: Experiment 2, $Z = 20$ m. a) backscatter with time; b) mean melt concentration of the top 2.5 cm with time; c) and depth and melt concentration with time.
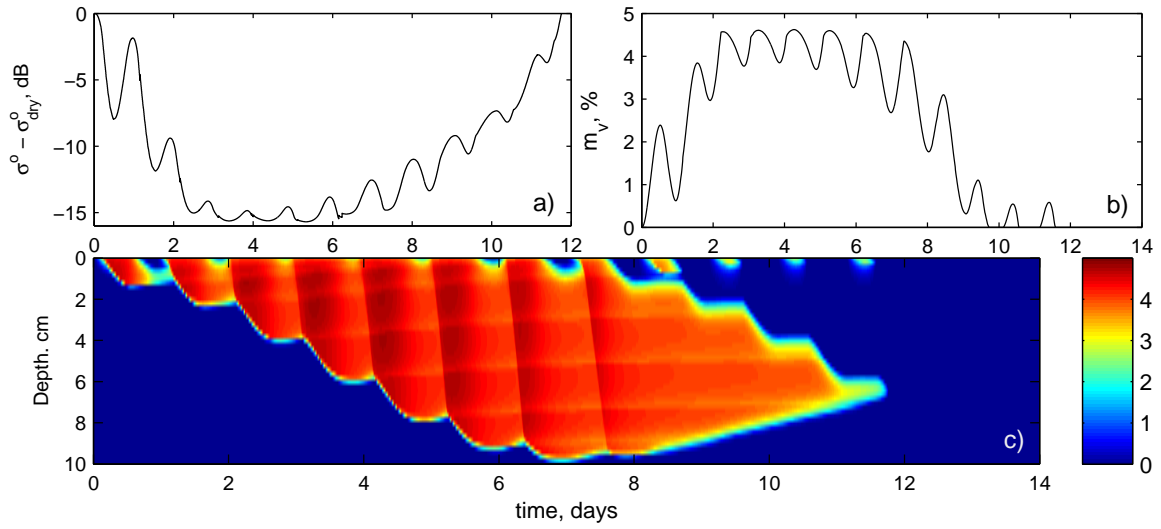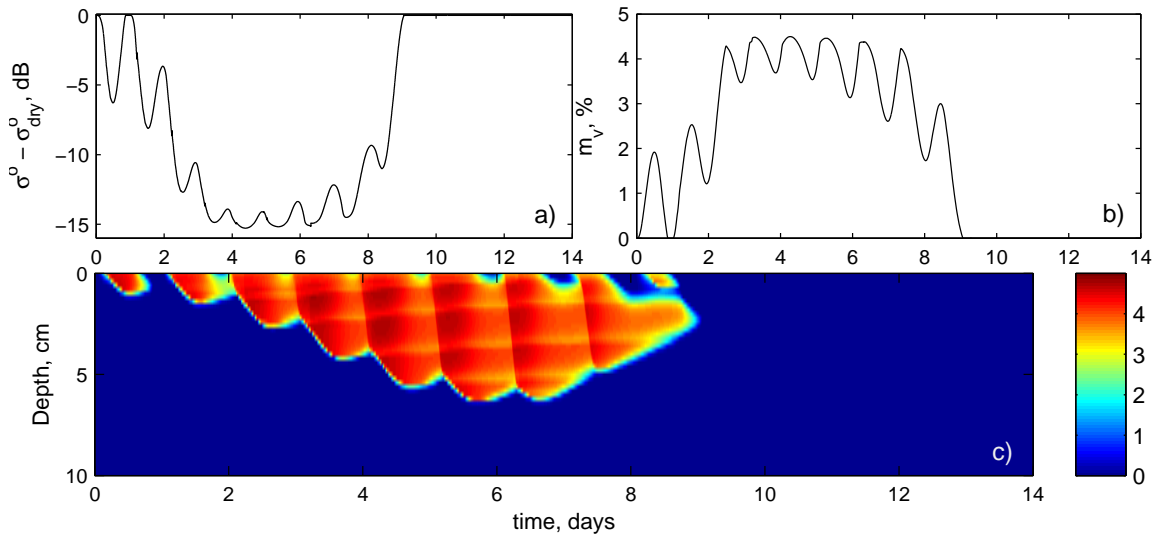

Figure 4.18: Experiment 2, $Z = 7$ m. a) backscatter with time; b) mean melt concentration of the top 2.5 cm with time; c) and depth and melt concentration with time.
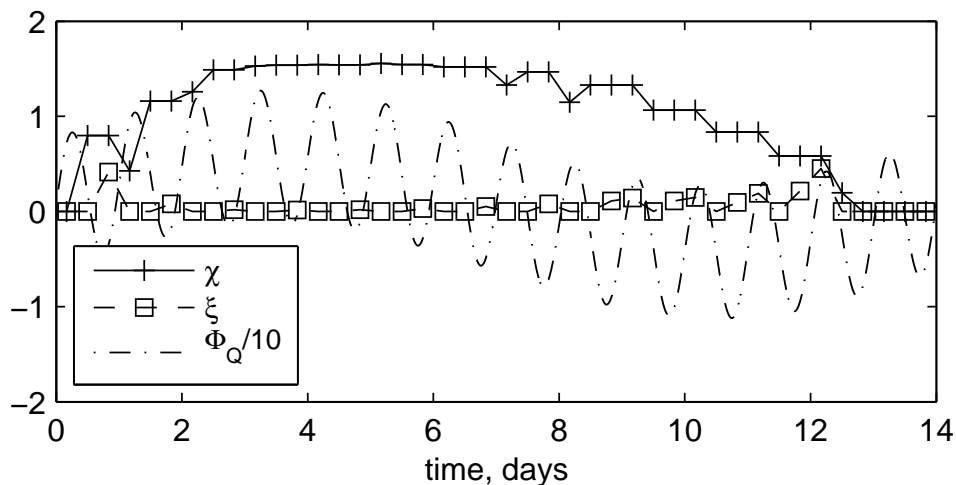
Figure 4.19: The MSI, χ, and RSI, ξ for experiment 2: $Z = 20$ m, as well as the heat flux, Φ_Q, scaled for clarity.

it follows the melt concentration in the top several centimeters, indicating that the MSI is following changes in σ^o_{wet}. Note that the difference between the peak melt and peak refreeze for each day is well correlated to the thickness of the wet snow layer.

4.4   Summary

In this chapter a new melt detection and estimation model is developed. This new model uses two layers during melt and three layers during refreeze. The new model is combined with a one-step Markov chain model and the rules of state change between the melt, refreeze, and frozen states are defined. The new melt detection and estimation method classifies snow into one of three melt states and provides two severity indexes, the melt severity index (MSI) and the refreeze severity index (RSI). These indexes are shown to follow the melting behavior of snow simulated by a one-dimensional geophysical/electromagnetic model. In the next chapter, this new melt detection and estimation technique is applied to the Greenland ice-sheet.

70

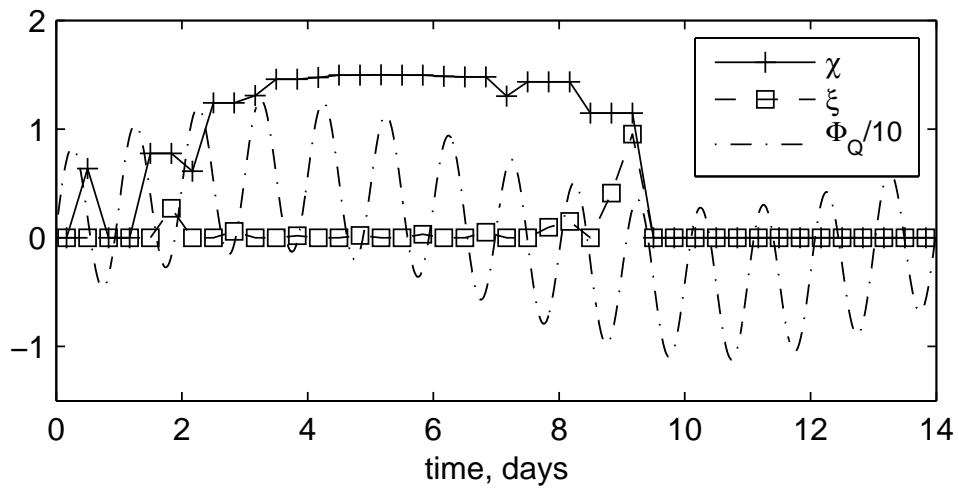Figure 4.20: The MSI, χ, and RSI, ξ for experiment 2: $Z = 7$ m, as well as the heat flux, Φ_Q, scaled for clarity.

Chapter 5

Greenland Melt Classification and Estimation

This chapter covers the application of the melt detection and estimation model described in Chapter 4 to the tandem morning/midday/evening QuikSCAT and SeaWinds imageset described in Chapter 3. To further verify the melt detection and estimation method, the tandem QuikSCAT/SeaWinds time-of-day filtered image time series is combined with automatic weather station (AWS) data collected as a part of the Greenland Climate Network (GC-NET) [41]. The AWS data is taken at the location of the ETH Swiss Camp, located at 69.57 N 49.30 W at approximately 1155 m above sea level. By comparing the tandem image set with the AWS data, the effectiveness of the melt detection method, as well as the MSI and RSI can be verified. Once verified by the AWS data, the melt detection and estimation technique is applied to the entire ice-sheet for the course of the entire tandem dataset, from JD 100 to JD 297, 2003. The resulting melt state classifications and estimates are analyzed.

This chapter is organized as follows. Section 5.1 compares the AWS data at the ETH Camp directly with the backscatter measurements from the tandem dataset, where the diurnal variation in the data is studied. Section 5.2 describes the comparison and analysis of the Markov chain-based layered model melt classification and estimation technique to the AWS data. In Section 5.3 the ice classification and estimation technique is applied to the entire ice sheet and an analysis of the resulting melt estimates is given. A summary of the results is found in the following chapter, Chapter 6.

5.1 Diurnal Variation

In this section, the time series of AWS and tandem QuikSCAT/SeaWinds data is analyzed. The Swiss Base AWS station is located in western Greenland, in the wet snow region of the ice-sheet. This region is characterized by frequent melt, making this station ideal for the application and verification of the new melt detection and estimation model described in this thesis. Figure 5.1 shows the entire tandem σ^o time series as well as the Swiss Camp AWS temperatures. Several interesting features are seen in this figure. First, the amount of diurnal variation in σ^o can be considerable; a cycle peak-to-peak amplitude of 3–6dB is seen for many days from the first major melt event at JD 153 until JD 200. Good correlation is seen between the diurnal cycle of air temperatures near the 0 C isotherm and σ^o. It is also observed that the amplitude of the diurnal cycle in both air temperature and σ^o becomes more sporadic after JD 200, and is much smaller from JD 220 on. Particularly during the heat wave from JD 236 to JD 246, σ^o remains low, with very little diurnal variation.

In order to better quantify the strength of the diurnal cycle, a matched filter is used. Match-filtering essentially measures the correlation between a signal and a reference. In this case, the reference is a sinusoidally varying complex exponential with a period of one day. By making the matched filter a complex exponential both the magnitude and phase of the diurnal cycle can be measured. Backscatter that varies daily has high correlation with the sinusoidal matched filter and thus the filter output has a high output amplitude. To allow for fast transients from melt to refreeze, a short 3 tap filter is used,

$$h[n] = \frac{1}{N}e^{-j\frac{2\pi}{3}n}, \tag{5.1}$$

where N is 3, and $n = [-1, 0, 1]$. This short filter has some tendency to smear the sharp transitions but effectively captures the transient behavior of the cycle variation. The filter output is the diurnal variation,

$$DV[n] = h[n] * \sigma^o[n]. \tag{5.2}$$

Figure 5.2 shows the magnitude of the diurnal variation, $|DV|$. Again, note the high consistent diurnal cycle for JD 153 until JD 200, and sporadic amplitude after
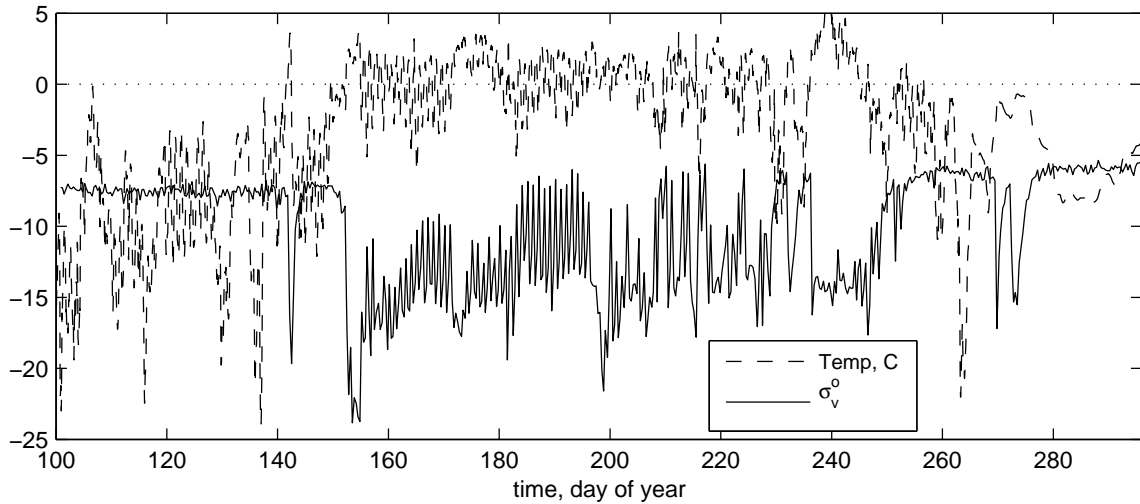
Figure 5.1: AWS Temp and σ^o time series of the entire tandem mission for the pixel at the location of Swiss Camp AWS, 69.57 N 49.30 W.

JD 200. The heat wave beginning JD 236 is characterized by low diurnal variation, as does several other periods where low σ^o are observed, e.g. JD 154, 178, and 198 among others. A scatter-plot of the σ^o and $|DV|$, shown in Figure 5.3, also identifies this interesting behavior: low diurnal cycle variation can occur for periods of intense melt, when σ^o is very low. This type of behavior is observed during intense melt across the wet snow and percolation zones of the ice-sheet.

Figure 5.4 presents a closer look a the time series from JD 145 to JD 168. A period of low backscatter, as well as other interesting features, are observed in this short time series. When the snow-pack is frozen, diurnal variation is small and σ^o high. As the temperature climbs and remains consistently above zero, σ^o remains low, with very little diurnal variation. As temperatures drop and begin cycling above and below the 0 C isotherm, the daily mean of σ^o rises slightly, and a large diurnal cycle is observed. Especially interesting is the time period from JD 163 to JD 166. During this time period the average air temperature is dropping, and the portion of the day above 0 C is also decreasing. During this period the average σ^o increases, while still maintaining a strong diurnal cycle. The σ^o peaks during this time period
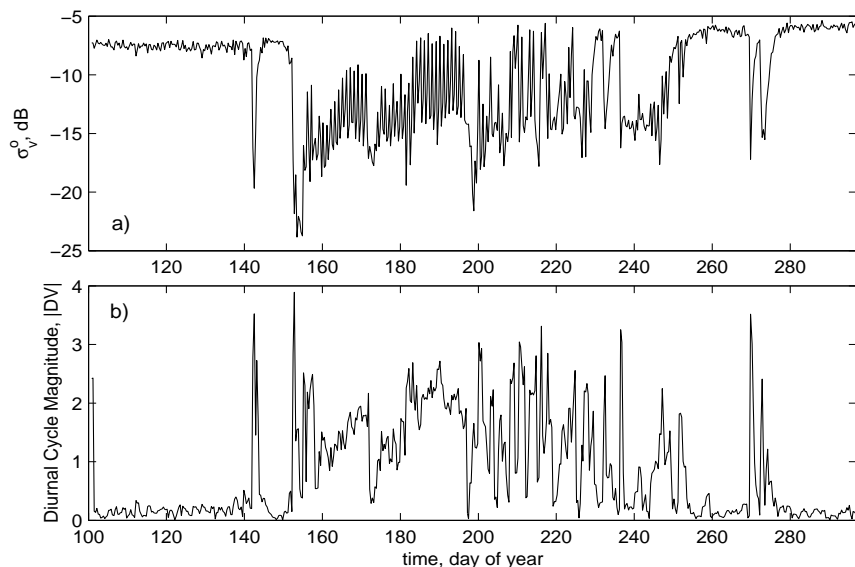
74

Figure 5.2: a) Backscatter, σ^o, and b) the diurnal cycle amplitude, $|DV|$, measured by a 3 tap complex exponential matched filter. Backscatter data is taken from the pixel at the location of Swiss Camp AWS, 69.57 N 49.30 W.

are still well below their winter value, suggesting that subsurface water is persistent, while the surface cycles from melt to freeze. Such behavior gives credence to the three-layer model developed in this thesis.

Since melt is observed in many instances where the diurnal cycle amplitude is small, it appears that the diurnal cycle amplitude alone is insufficient for identifying melt. This result may in part, explain some of the performance issues related to previous work [10]. It is conceivable that strong melt events, especially melt created by latent and specific heat input by convection from warm air masses, can continue during the night hours when solar radiation is negligible. Note also that the period of strong diurnal variation of σ^o occurs at times near the summer solstice (JD 173), when solar radiation is at its peak and the diurnal variation of solar radiation is large, suggesting that melt during this period of time is driven primarily by solar heating. Likewise, late season melt appears to be driven primarily by warm air masses, explaining the resulting decrease in diurnal cycle amplitude. The air temperature
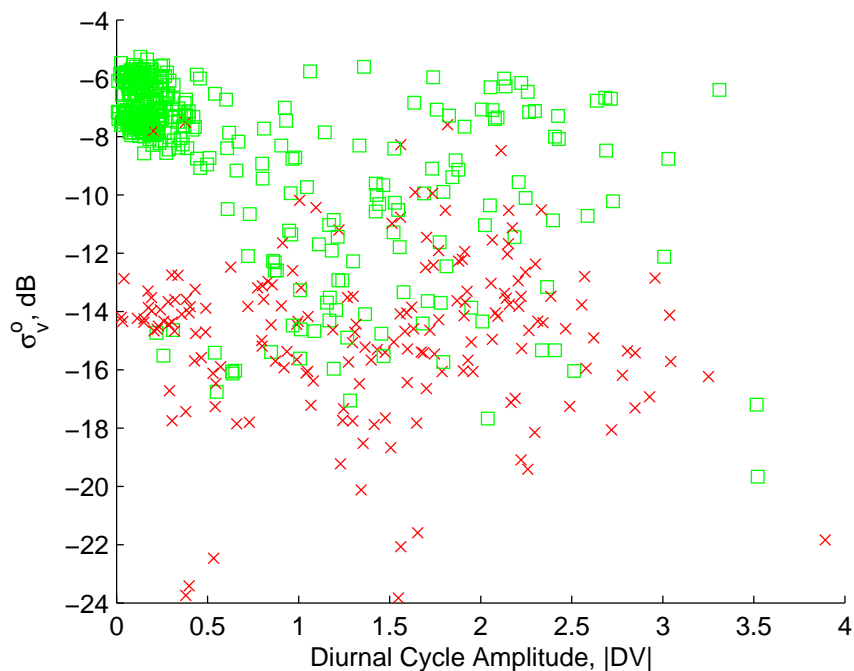
Figure 5.3: Scatter plot of σ^o vs. diurnal cycle amplitude $|DV|$, as measured by a 3 tap complex exponential matched filter. The squares show where the surrounding air temperature is less than 0 C, while the 'x's show where the air temperature is greater than 0 C. Backscatter data is taken from the pixel at the location of Swiss Camp AWS, 69.57 N 49.30 W.
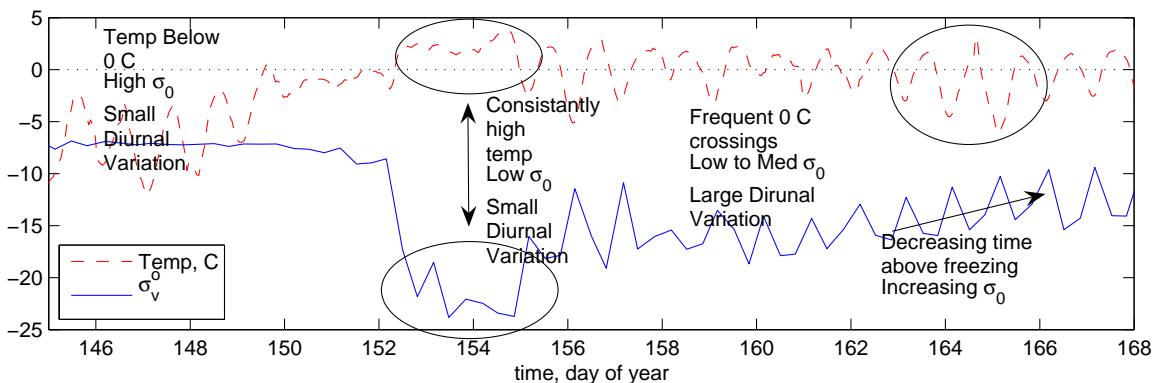
Figure 5.4: AWS Temp and σ^o time series for JD 145 to JD 168, 2003 at Swiss Camp AWS, 69.57 N 49.30 W.
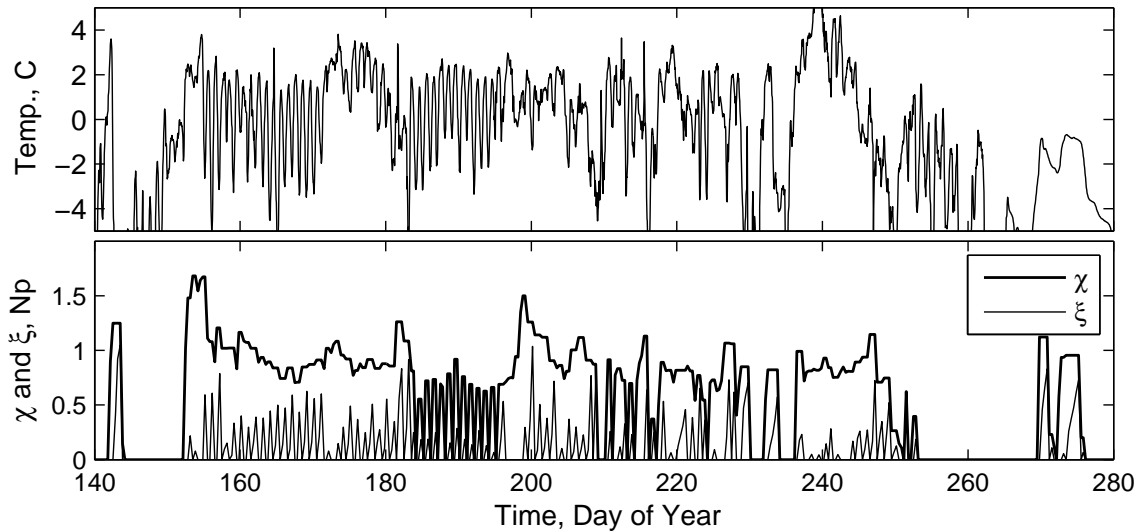
Figure 5.5: Top: AWS air temperature. Bottom: χ(thick) and ξ(thin). Estimators use backscatter data taken at pixel located at Swiss Camp AWS, 69.57 N 49.30 W.

during the late season appears to vary more slowly, suggesting perhaps, an increase in cloud cover insulating the ground from space.

5.2 ETH Camp Ice State Estimates

In this section the melt detection and estimation technique described in Chapter 4, is applied to the ETH Camp backscatter data. Figure 5.5 shows the MSI, χ, and RSI, ξ, at the ETH Swiss camp location, as well as the air temperature for reference. At first glance, the behavior of the MSI and RSI correlates well with the temperature at this location. Because this method of melt detection distinguishes separate melt events delimited by samples where the ice is frozen, a more detailed analysis of the behavior of individual melt events is possible.

The first and longest melt event during the 2003 melt season at the ETH Camp (JD 152–183) shows some interesting features and is helpful in illustrating the effectiveness of the MSI and RSI. The MSI, RSI, air temperature, and up- and down-welling shortwave radiation (SW), are shown in Figure 5.6. The beginning of the melt event on day JD 152, as identified by the Markov melt detector, is consistent
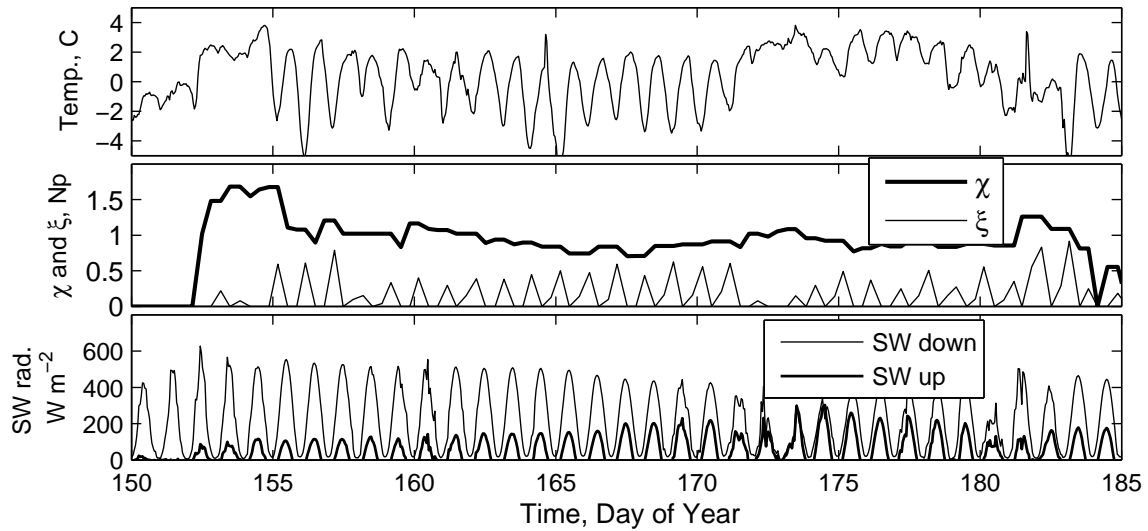
Figure 5.6: The estimators MSI and RSI of the longest melt event of 2003 at Swiss Camp AWS, 69.57 N 49.30 W. Top: AWS air temperature. Middle: χ and ξ. Bottom: Short wave radiation upwelling and downwelling.

with a peak in the net SW radiation, and a rise in air temperature above the 0 C isotherm. The beginning of melt is followed by several days (JD 152–154) where the air temperature remains above 0 C. The MSI and RSI correspondingly show heavy melt and little refreeze during this time period. During the mornings of JD 155–157, the air temperature drops well below 0 C, which should result in surface refreeze; the drop in MSI and strong cycling in the RSI clearly shows this trend. In the mornings between JD 157 and 158, and again between JD 159 and 160, the temperature drops below 0 C only for a short time. The RSI during these morning is notably less than mornings before and after, mimicking the air temperature. A trend of dropping temperature and net SW radiation is seen during JD 160–165; the MSI and RSI capture this behavior as MSI gradually decreases and RSI increases. Similar to JD 152–154, the temperature rises above 0 C during JD 172–175, though the net SW radiation is fairly low. During this time period, a constant melt is recorded by the MSI and RSI, though not nearly as strong as during JD 152–154, as expected by the high air temperature and low SW radiation. Days 175 to 180 show air temperatures

constantly above 0 C; however, the RSI continues to show significant refreeze during this time. The net SW radiation during this time period is fairly low, conceivably creating a net loss in total radiation, and leading to refreeze in the mornings despite higher air temperatures.

The analysis of the longest melt event at the ETH/CU Swiss Camp shows that the MSI and RSI reasonably follow the behavior expected from air temperature and SW radiation data. While these indexes behave as expected, they do not directly translate into physical melt quantities. However, their behavior suggests that they may be a useful tool in deriving quantitative data at some point in the future. Particularly, improvements in surface property inversion techniques [42] may provide much needed *a priori* information, making the direct inference of melt quantities possible. Therefore, the estimates provided by χ and ξ may be used as model inputs from which better melt estimates may be obtained. Despite their indirect relation to melt, some interesting behavior can be seen using these indexes. For example, the integrated melt severity index, I_χ (IMSI), defined by,

$$I_\chi = \sum_{k=1}^{N(t)} \chi_k \Delta t, \tag{5.3}$$

where $N(t)$ is the number of samples where melt is detected and $\Delta t = 8$ hours, is useful for looking at seasonal melt strength (see Figure 5.7). The difference between the MSI and RSI, refered to as the melt envelope (ME) $\psi = \chi - \xi$, is a useful indication of the thickness of wet snow, especially the daily minimum ME, defined as

$$\psi_j^d = \min_{i=\{1,2,3\}} (\chi_{j,i} - \xi_{j,i}), \tag{5.4}$$

where j is the day of the year, and i is the ith sample of the day (shown in Figure 5.8). The integrated melt envelope (IME), defined by

$$I_{\chi-\xi} = \sum_{k=1}^{M(t)} (\chi_k - \xi_k) \Delta t, \tag{5.5}$$

where $M(t)$ is the number of samples where liquid water is present, is shown in Figure 5.7. Since the amount of liquid water—and its proximity to the surface—drives vapor transport, grain growth, and other parameters that affect mass balance, the ME and

related indexes may prove useful. Table 5.1 summarizes the statistics for the pixel located at the ETH camp.

Table 5.1: 2003 Melt statistics for the ETH/CU Swiss Camp AWS located at 69.57 N 49.30 W.

Statistic	Value	Description
T_b	142.1775	Beginning time of first melt, decimal JD
T_e	275.8400	Ending time of last melt event, decimal JD
T_{length}	133.6625	Melt season length, days
T_M	1202.6	Total time melting, h
T_L	2307.8	Total time wet snow is present, h
$t_{l,\text{longest}}$	760.2	Longest melt event, h
$\bar{t}_l$	85.4753	Mean melt event length, h
$\text{median}(t_l)$	16.4167	Median melt event length, h
$\text{std}\, t_l$	183.676	Standard Deviation of melt event length, h
N_l	27	Number of melt events
$\max \chi$	1.6821	Maximum melt severity, Np
$\bar{\chi}_{\text{melt}}$	0.8474	Mean melt severity during melt, Np
$I_{\chi_{\text{melt}}}$	1020.3	Integrated melt severity, Np·h
$I_{\chi-\xi}$	1652.0	Integrated melt envelope, Np·h

The new method performs similar to the Q-α method employed in [11]. This is expected, as the two-layer model and the 3 dB threshold is the same as that used by Ashcraft and Long. For comparison, Figure 5.9 shows the metric function $q(t)$ for both the new method used in this paper and the standard $q(t)$ described in [11]. The metric function used by the new method employs data from both SeaWinds and QuikSCAT, which yields better temporal sampling than QuikSCAT alone. Melt detection using the Q-α method estimates the first day of melt occurs on JD 142, as does the new melt detection method. The last day of melt detected by the Q-α method is on JD 275. The last day of melt detected by the new melt occurs one day earlier on JD 274; however, refreeze is detected until JD 275, producing identical season lengths at this location. There are some differences in the number of days
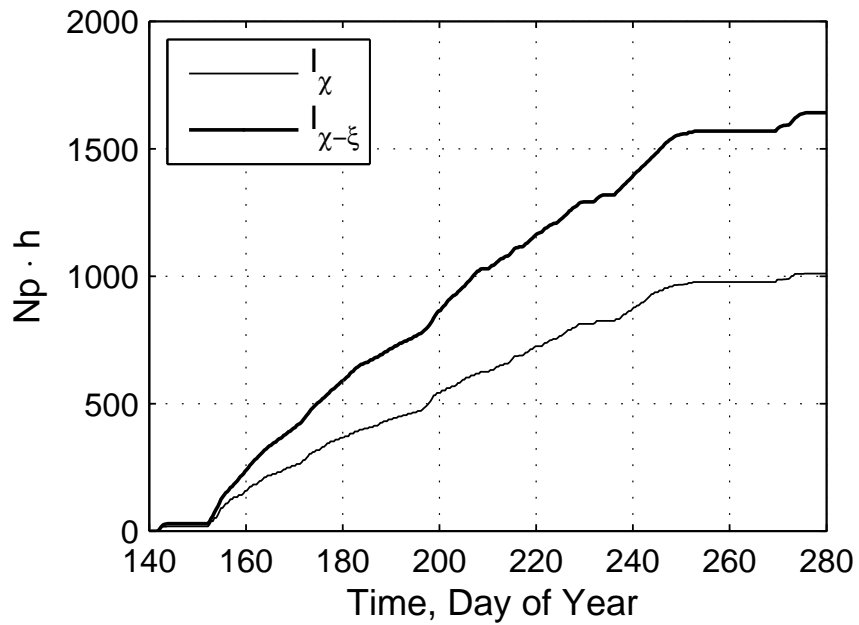
Figure 5.7: The IMSI and the IME. Data is for 2003, Swiss Camp AWS, 69.57 N 49.30 W.
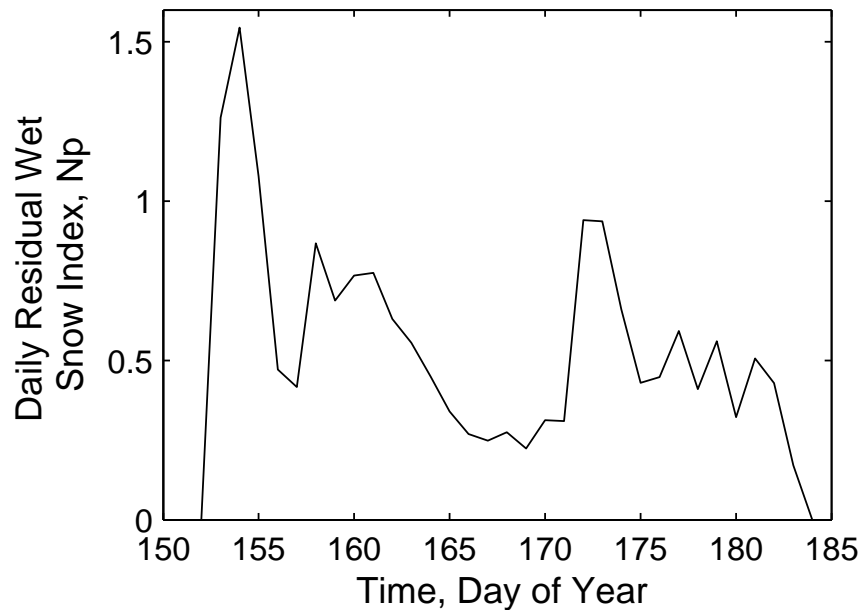
Figure 5.8: Daily ME at Swiss Camp AWS, 69.57 N 49.30 W. The time period coincides with the longest melt event, JD 150-185 2003, shown in Figure 5.6.

81
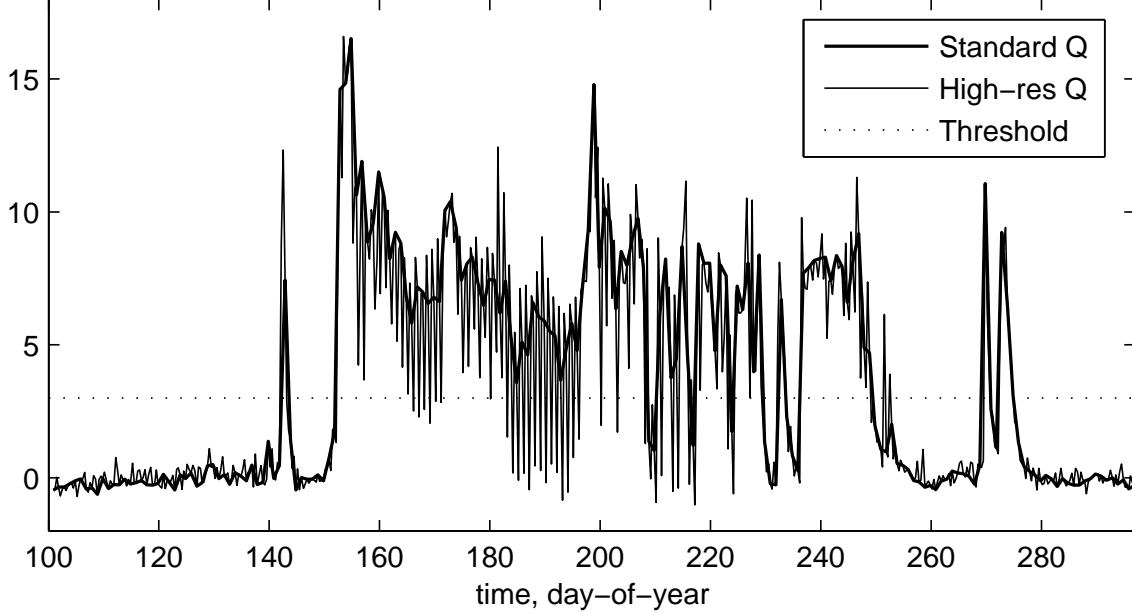
Figure 5.9: Comparison of the metric $q(t) = \sigma^o_{\text{dry}} - \sigma^o$ using the High-res data employed in this thesis and using the standard data used by the Q-α method described in [11].

where melt is detected—the new method detects melt at least once a day for 100 days of 2003, where the Q-α method detects melt for only 92 days. The differences in the melt classifications are mostly due to the new method using SeaWinds data, which measures earlier in the day when melting is more likely to occur. The ability of the new method to use the high temporal sampling to distinguish melt from refreeze and the ability to estimate the melt severity are the primary improvements the new method adds.

5.3 Ice-sheet Melt Estimation

Next, the new melt detection and estimation model is used to obtain a melt estimate of the entire ice sheet. The melt model scales very easily to the entire ice sheet because the dataset itself is comprised of images. First, the model is limited to include only glaciated regions of Greenland using an image mask, shown in Figure

5.10. Second, σ_{dry}^o is determined using a least squares estimator and images of the winter months before and after the melt season. A least squares estimator is used to compensate for the slow variation in σ_{dry}^o that occurs from season to season. Since the dataset is short, consisting of mainly summer months, the daily winter QuikSCAT-only images of Greenland from JD 001–061 and 305–365 are used to estimate σ_{dry}^o. The resulting least squares estimate provides σ_{dry}^o at JD 001 and the slope of σ_{dry}^o with time. Figures 5.11 and 5.12 show images for σ_{dry}^o on JD 001 and the slope of σ_{dry}^o over the year 2003, respectively. The estimation of the ice-sheet melt produces a number of images of the ice state, the MSI, RSI, and other indexes.

Using the Markov melt detector, the melt season of 2003 is characterized. Figure 5.13 shows the first day of seasonal melt, the last day that liquid water was detected in the snow-pack, and the length of the melt season. Small melt artifacts are seen in the dry snow zone, a result of additional noise introduced by SeaWinds images on JD 226 and 262, which contain regions of missing data.

First, the beginning of the melt season (Figure 5.13a) is considered. Most of the melt season is captured by this dataset; however, there are several patches along the south-eastern coast near 65.0 N 42.0 W and 65.5 N 40.5 W, as well as slightly inland near 62.5 N 44 W, where melt is detected during the first day. These regions may actually be melting sooner than the start of the dataset. Progression of the melt season across the island appears to occur regionally, and in discrete increments. For example, most of the snow-pack near the western coast begins its melt season on JD 140 and reaches far inland on the following day JD 141, bridging the west and east sides of the southern tip of the island near the saddle separating the summit from South-Dome. The northern and north-eastern coastal areas begin melt slightly later, near JD 155. Melt progresses up-slope in western Greenland into the percolation zone in several increments, JD 177, 197, 219, and 236–238. The progression of melt across South-Dome in southern Greenland occurs in two increments: JD 151 and 197. Several pockets of melt along the eastern coast begin early, on JD 135, and progress up-slope incrementally on JD 141, 143, 159, and 173.
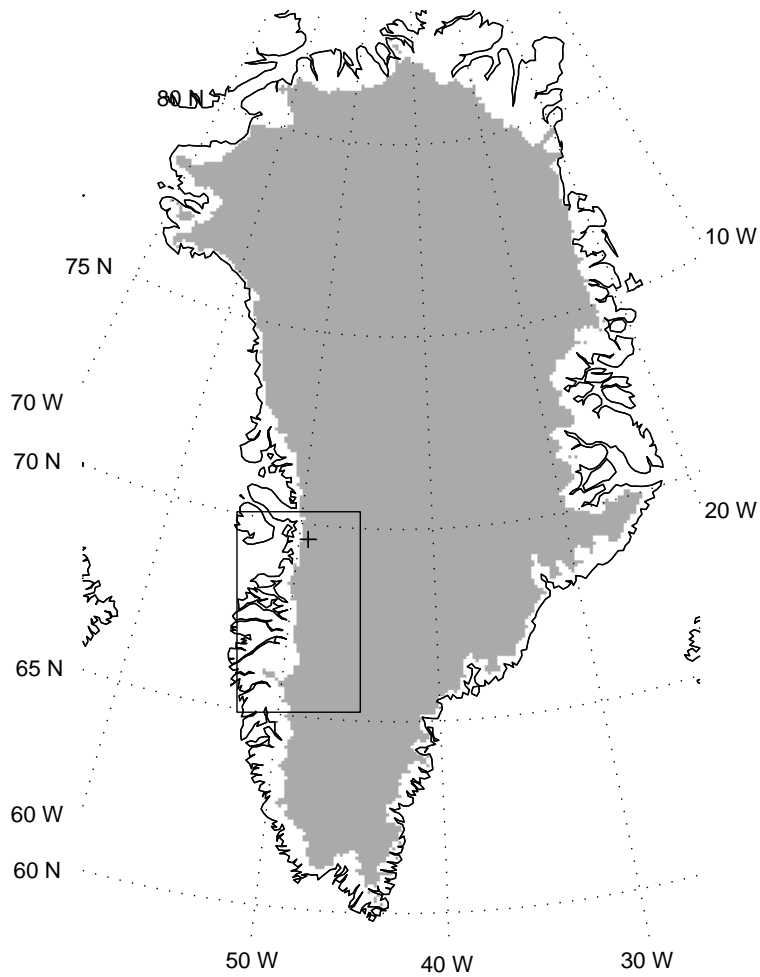
Figure 5.10: Image mask for the ice-sheet used in melt estimator. The cross in this and subsequent images shows the location of the ETH/CU Swiss Camp. The box is the region is used to present the time series in Figures 5.16 and 5.17.
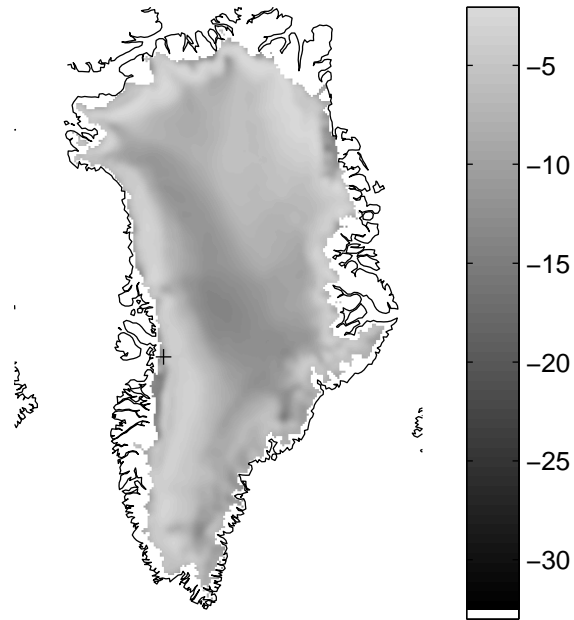
Figure 5.11: Image of σ_{dry}^o at JD 001 found using the linear least squares of the daily backscatter over JD 001 to 061 and JD 305 to 365 of 2003. σ_{dry}^o is shown in dB.
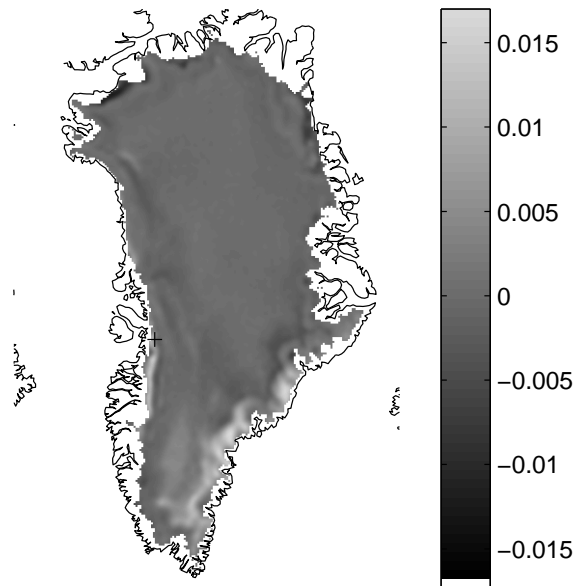
Figure 5.12: Image of the slope of σ_{dry}^o verses time found using the linear least squares of the daily backscatter over JD 001 to 061 and JD 305 to 365 of 2003. The slope is shown in dB/day.
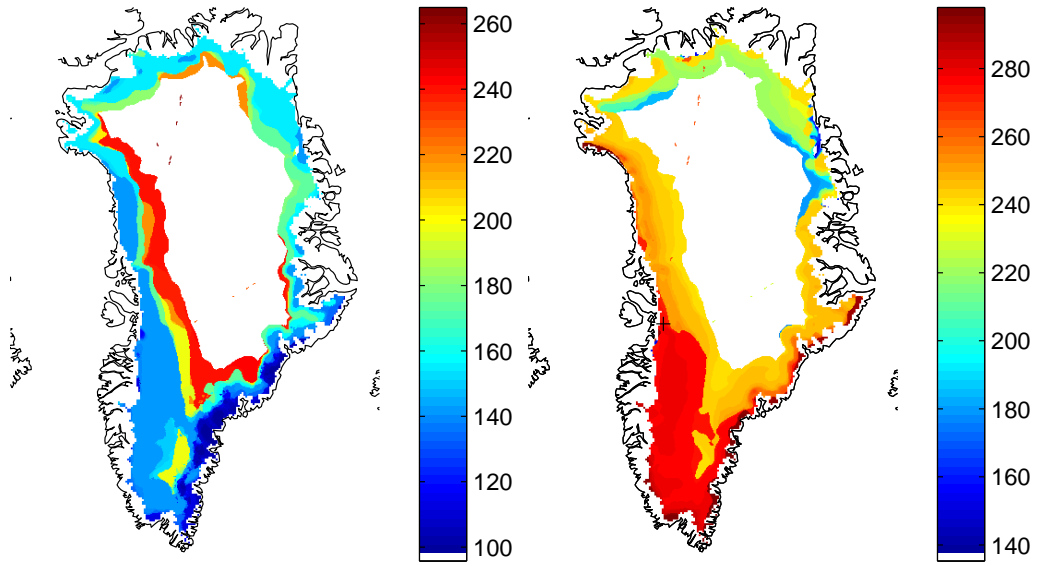
(a) First Day of Melt, JD

(b) Last Day of Liquid Water, JD
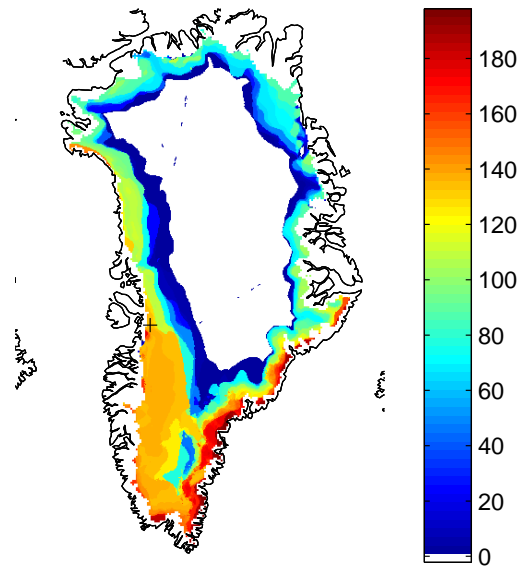
(c) Melt Season Length, Days

Figure 5.13: From left to right: the first day of the year 2003 melt is detected, the last day of the year 2003 liquid water is detected (melt or refreeze) and the length of the melt season. The length of the season is in days.

Like melt, seasonal refreeze shown in Figure 5.13b occurs regionally and in discrete increments; however, refreeze spreads much more quickly and uniformly than melt. The higher elevation percolation regions of southern and western Greenland finish refreezing on JD 239. Refreeze progresses nearly to the edge of the ice sheet along the western coast by JD 250. A late season melt event caused by the remnants of Hurricane Juan leaves the snow pack wet in southern Greenland until JD 276–278. Northern and northeastern Greenland refreeze much sooner, beginning along the coastal region near 76.5 N 23.5 W on JD 157. Refreeze occurs in the north and northeastern percolation zones starting JD 180 and progresses completely to the edge of the ice-sheet by JD 222. A very small region near the southern tip of the island shows continued melt up to the last day in the dataset, JD 297. Thus, the last day of melt may be later than shown at this location.

The season length shown in Figure 5.13c shows how season length is regionally correlated and how it varies from region to region. The longest melt season occurs where the first melt is detected in pockets along the southeastern coast and the southern tip of the island. Because of the limited number of days in the dataset, some of these areas have longer seasons than indicated since melting starts before the beginning of the dataset. Besides these pockets along the southeastern coast, the snow-pack east of Jakobshavn (roughly 69.2 N 50.0 W) has the longest melt season of 179 days, followed by a strip of snow along the northern end of the Melville Bugt (around 76 N 65 W) with a season of 144 days. The vast majority of the southern and western parts of Greenland have a melt season 135–136 days long. Further north along the western coast, the season becomes shorter: 108 days. Northern and Northeastern Greenland have relatively short melt seasons ranging from 60–90 days. Naturally, the shortest seasons are located at higher elevations, as short as a single day near the dry snow line separating the percolation and dry snow zones.

The IMSI and IME for the ice sheet are shown in Figure 5.14 and 5.15, respectively. It is clear from these figures that the dynamic range of melt severity is quite large—over three orders of magnitude from the edge of dry snow to the edge of the wet-snow zones. Melt is greatest along the southeastern coast, in the same

region where the melt season is longest. The southern and western sides of the island experience greater melt than the northern and northeastern sides—typically the IMSI is three to five times higher in southern Greenland than northern Greenland. It is interesting to note, however, that there is much greater contrast between the percolation and wet-snow regions than the melt along the edge of the ice-sheet from region-to-region across the island.

While melt state detection using the Markov detector appears to work well across the entire ice sheet, the MSI and RSI and other severity indexes are only applicable in regions where the snow-pack resembles the layered melt model. In the lower edges of ablation zone, snow from the previous year's accumulation completely melts away, exposing the dense glacial ice beneath. Exposed glacial ice behaves markedly different in melting conditions than iced-firn or snow. Melting glacial ice results in water pools at first; however, these water pools eventually percolate deep into the ice. The remaining nearly liquid-free ice is nearly impermeable to water, except along channels where the liquid may be quickly removed beyond the reach of the radar signal. Melt quantity in these regions, though significant, is quickly removed from view, and thus may not attenuate the backscatter as much as it would have in iced-firn.

The change in behavior of snow is seen in the IMSI shown in Figure 5.14. In western Greenland there is a ridge of maximum melt severity that occurs well within the edge of the ice-sheet. This peaked region likely occurs near the equilibrium line, where the previous season's melt is entirely melted away, showing a stark change in the structure of the snow-pack, from iced-firn to glacial ice. The ridge of high IMSI appears to be near the equilibrium line due to its position relative to the ETH/CU Swiss camp, which is near this line (see Figures 5.14 and 5.15). A change in the snow characteristics, evidence for the IMSI ridge, is also seen in the backscatter at the ETH Camp shown in Figure 5.2; past JD 200, the backscatter is never as low as before JD 200, even during the heat wave starting on JD 235, when the highest temperatures of the season are observed.
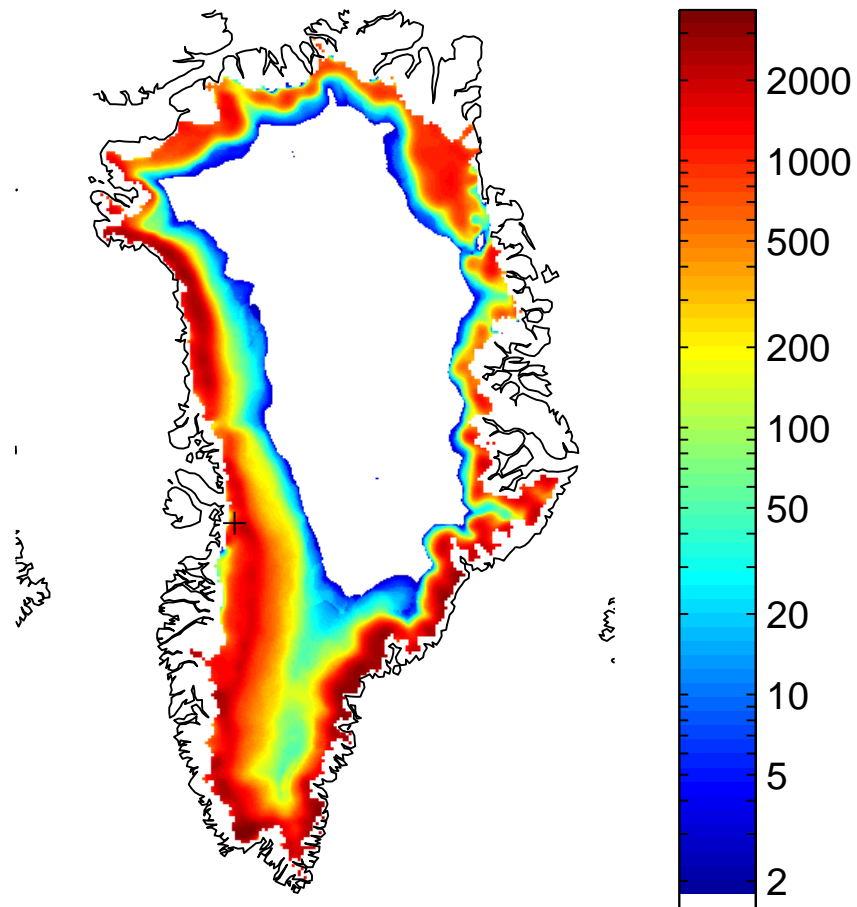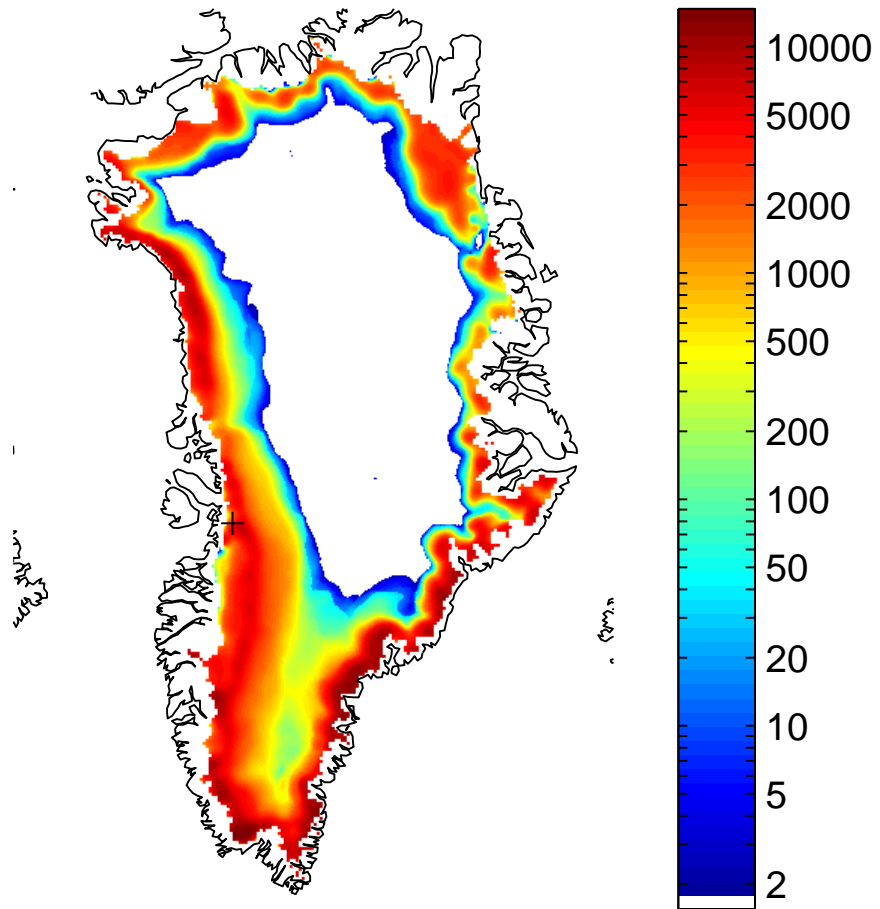
Figure 5.14: Seasonal IMSI, I_χ Np·h

Figure 5.15: Seasonal IME, $I_{\chi-\xi}$ Np·h

To gain further insight into the ridge of maximum IMSI observed in western Greenland seen in Figures 5.14 and 5.15, the MSI and RSI time series are analyzed. Figures 5.16 and 5.17 show a series of morning ME, $\chi - \xi$, images of a section of Greenland. Only morning images are shown for reasons of brevity. Days not shown in these figures do not have significant persistent melt and are omitted. The morning images, which observe persistent melt, show some interesting behavior. A strip of persistent melt appears in these image some distance from the western edge of the ice-sheet. Moreover, this strip slowly moves eastward as the melt season progresses. From this it can be postulated that this persistent melt strip identifies saturated wet snow. Furthermore, the western edge of this strip identifies where the wet snow ends and the exposed glacial ice begins.

In order to properly deal with the change from firn to glacial ice a different model needs to be developed and applied to the glacial ice. A new model is needed primarily due to differences in the percolation mechanism. However, dealing with rapid percolation of water along small channels in the glacial ice, rather than the more diffuse percolation assumed by the two and three layer models, is not easy. The problem is due to the nature of localized flow, and the lack of information of its effects on backscatter. On the other hand, the identification of glacial ice, and other snow types, may be improved by using information gained by the MSI and RSI developed in this thesis.

The classification of the snow types in Greenland may be aided by the MSI and RSI. It has been shown that the identification of exposed glacial ice may be possible. The identification of snow types in other regions of Greenland may also be possible. Figure 5.18 shows the IMSI with a Long-Drinkwater facies map overlay on the image, which shows the boundary of the snow zones in the fall of 1978 [6]. This map was created by identifying differences in the backscatter across the various regions of Greenland using fall SASS data. First, it is clear that there is strong correlation between the map and the IMSI. While the metric used to distinguish the snow zones in the 1978 map is very different from the method used to create the IMSI image, the similarities suggest that the IMSI could reasonably be used to classify the ice facies.

91

Order
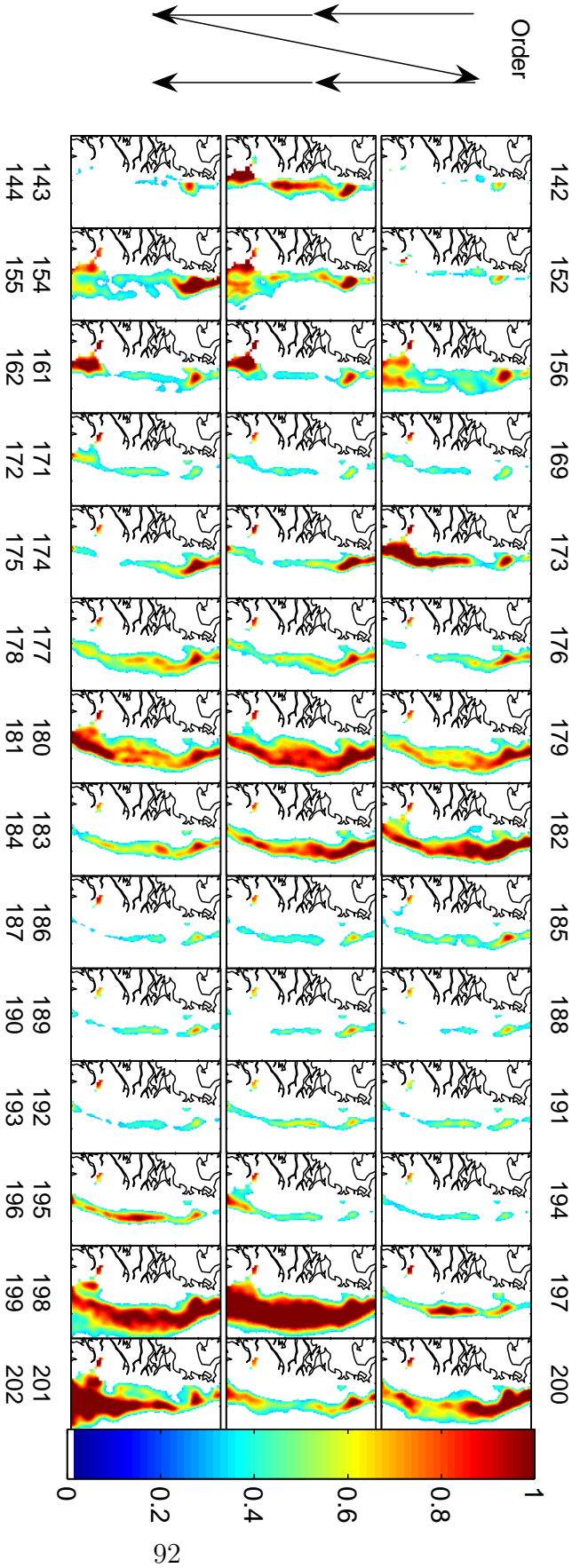
Figure 5.16: Time series of morning $\chi - \xi$ images over the small section of western Greenland shown in Figure 5.10. These illustrate persistent melt for many days of 2003. The region west of the melt ridge seen in Figures 5.14, 5.15, and 5.18 is seen in the time series as a vertical strip of persistent melt. The western edge of this strip moves eastward over the year, suggesting that it follows the receding snow-cover of this year's accumulation. This series of images is continued in Figure 5.17. The day of the year is specified above for the top row of images, and below for the middle and bottom rows. Chronological order proceeds top-to-bottom, and left-to-right.

92

Moreover, the IMSI is a more objective classifier of snow types since it attempts to measure melt directly rather than classifying snow types indirectly through changes in dry snow backscatter which may be affected by other factors.

The differences between the 1978 map and the IMSI image shown in Figure 5.18 are also interesting and noteworthy. The most apparent difference is the line separating the percolation zone and dry snow in the 1978 map, and the location of no-melt line in the IMSI image. Differences in the metric used to create these two maps may explain some of the differences; however, the IMSI along the 1978 dry snow line is typically 100 Np·h, a considerable amount. This amount cannot be observed by a solitary melt event, most of boundary pixels experienced 5–20 days of melt. Since so many days of melt are observed, it is apparent that the dry-snow is further up-slope. The moving of the dry-snow line further up-slope is consistent with local warming of the climate in western Greenland.
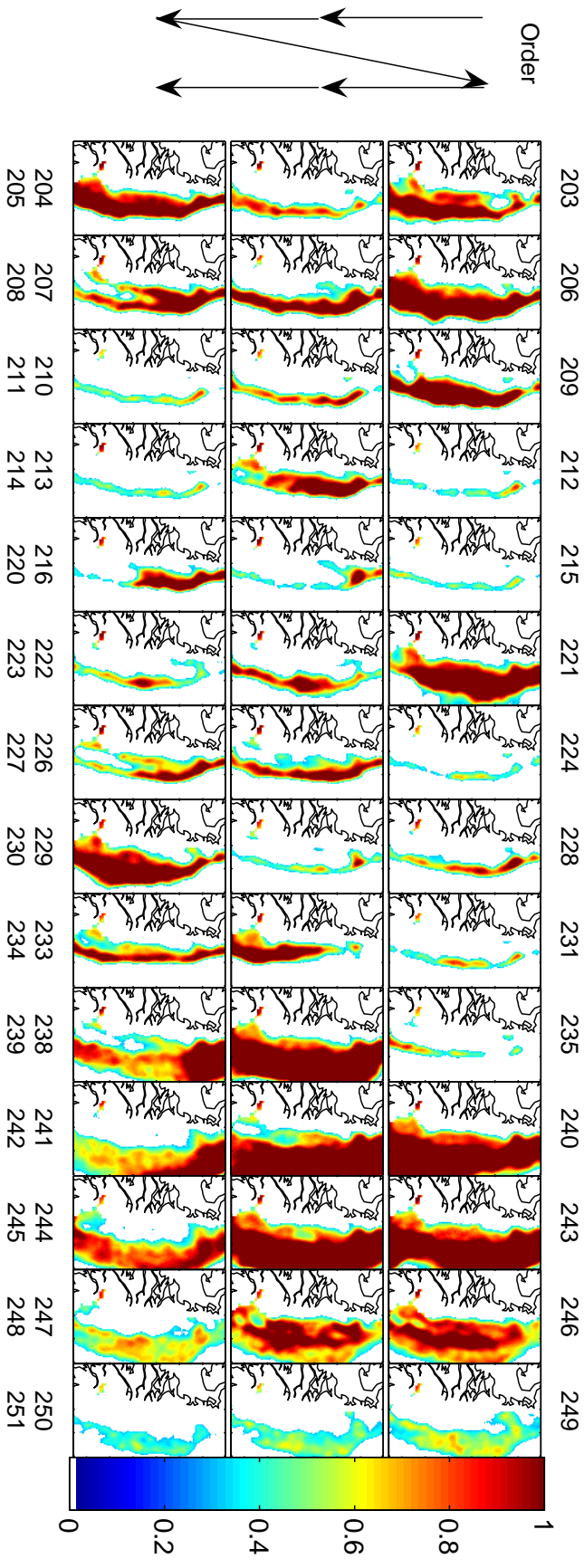
Figure 5.17: Continuation of the series of morning $\chi - \xi$ images described in Figure 5.16. The day of the year is specified above for the top row of images, and below for the middle and bottom rows. Chronological order proceeds top-to-bottom, and left-to-right.
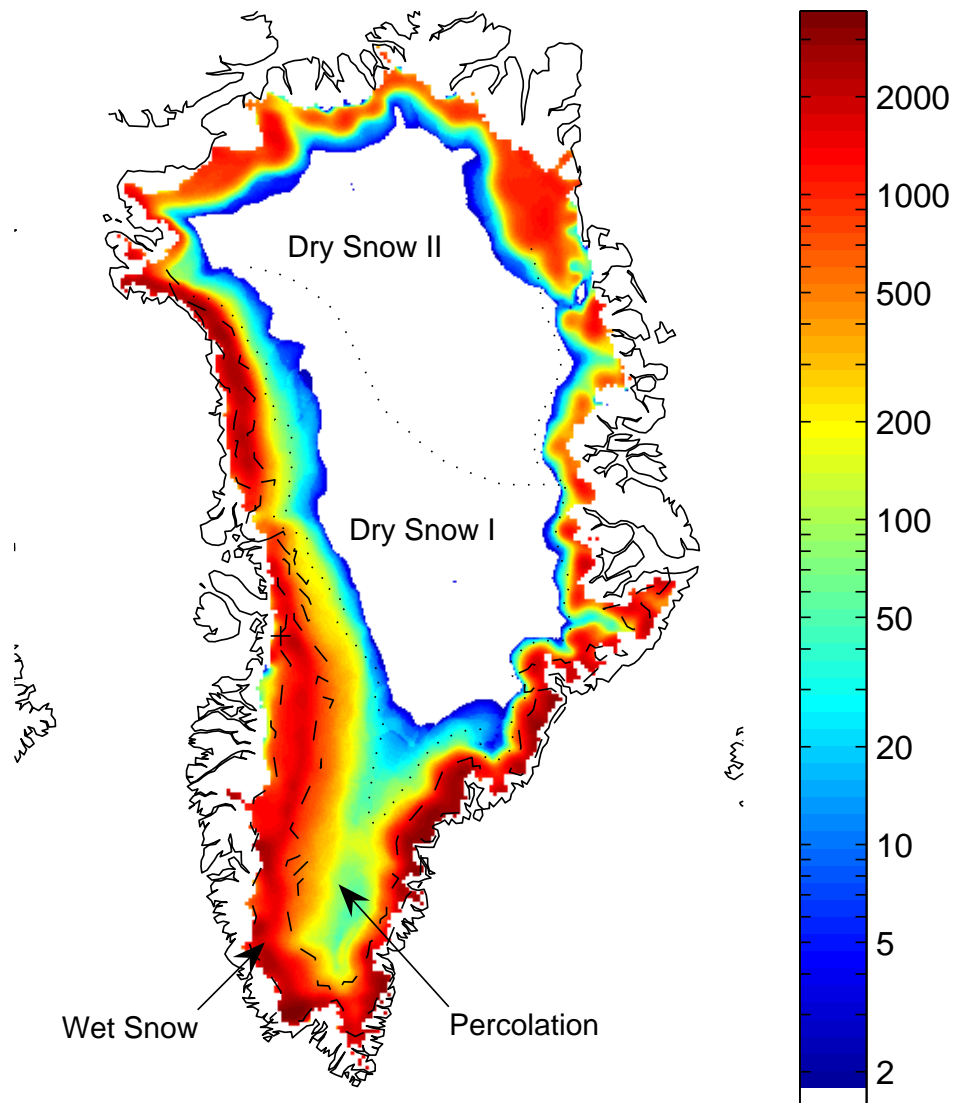
Figure 5.18: The IMSI shown in Figure 5.14, with the SASS (Long-Drinkwater) map [6] also shown.

Chapter 6

Summary and Conclusions

In this thesis a new method of melt detection and estimation is developed. This new method combines a simple layered electromagnetic model with a Markov chain detection algorithm to identify the melt state of snow. This method is used to classify the snow-pack into three states: melting, refreezing, and frozen. The parameters of the layered electromagnetic model are also used to estimate the severity of melt and refreeze. This new melt model is tested and validated by a simple geophysical/electromagnetic model simulation of the snow-pack under melting conditions and by *in situ* weather station data.

This new melt method is applied to a newly developed tandem QuikSCAT and SeaWinds image set. This new dataset is created by separating backscatter measurements by their local time-of-day, rather than the direction of the spacecraft's orbital motion. The resulting images have much greater temporal separation and resolution than those previously available. The tandem morning, midday, and evening SIR image set provides three nearly uniformly spaced temporal samples per day, allowing the resolution of the diurnal cycle.

Using the new tandem image dataset, the diurnal variation of the backscatter at the location of the ETH Camp is studied along side air temperature data from Swiss Camp AWS in western Greenland. The diurnal cycle magnitude, measured using a matched filter, is measured and analyzed. The diurnal cycle magnitude alone is not a sufficient indicator of melt—periods of intense melt may show little diurnal variation. The diurnal variation of backscatter, however, does lead to some interesting observations. First, the backscatter correlates well with air temperature crossings of

the 0 C isotherm, showing the sensitivity of backscatter to snow melt. Second, the diurnal variation is highest at the beginning of the 2003 melt season at the ETH Camp, during the time period when the sun is near its solstice and the variation of solar insolation is at its peak. Third, the daily normalized radar cross-section often does not return to its winter value, suggesting that subsurface water is often persistent between melting.

Applying the melt detection and estimation method to the backscatter of the entire ice-sheet, including the location of the ETH Camp, results in a reasonable estimate of the melt state. Seasonal melt maps are generated, which show the beginning, ending, and length of the melt season. Additionally, the melt and refreeze severity indexes, MSI and RSI, are analyzed on the ice sheet. While the melt model used is very simple, it provides reasonable estimates of relative melt severity across the ice sheet. The integrated melt severity index, IMSI, shows good agreement with the map of ice facies generated using SASS scatterometer data by [6]. Discrepancies between the dry snow line given by the SASS map and the melt estimated by the IMSI map are consistent with local warming in western Greenland indicated by an up-slope movement of the dry-snow line between 1978 and 2003.

6.1 Contributions

This thesis makes several contributions to the field of remote sensing. New models and methods are developed and used in Greenland. In particular, these contributions are important steps toward remote measuring of Greenland melt. The following list outlines these contributions.

- The temporal sampling of the SeaWinds instruments aboard the QuikSCAT and ADEOS II space craft have been carefully considered. Problems with the current ascending/descending method of SIR image generation in the polar regions have been identified.

- A new method of temporally separating QuikSCAT and SeaWinds backscatter measurements into images has been described and imagesets have been generated. These new images have been shown to exhibit much better temporal resolution than the previous ascending and descending images.

- A new dataset of QuikSCAT, SeaWinds, and tandem QuikSCAT/SeaWinds time-of-day filtered images has been generated. This new dataset is scheduled to replace the ascending/descending images as a standard image set in the polar regions.

- A new melt model is created, based on work performed by [11], which handles both melting and refreezing snow conditions.

- Melt classification is performed using a Markov chain model, allowing relative changes in σ^o to be reflected in the decision process.

- The combination of the Markov chain model with the layered melt model provides means to classify the snow-pack into three states: melting, refreezing, and frozen.

- The new melt model provides not only means of melt classification, but also the ability to estimate the melt and refreeze severity. While the resulting MSI and RSI may not directly translate to physical melt quantities, they are a first step toward obtaining such quantities from microwave measurements.

- The new melt model and melt classification and estimation technique are evaluated using a geophysical/electromagnetic model simulation of the snow-pack. This model simulation incorporates heat transfer, melt, percolation, settling and densification of the snow, in addition to modeling the backscatter using a radiation transfer model.

- This is the first time scatterometers have been used to separate melt from refreeze, and the first time scatterometers have been used to estimate melt severity.

- Melt season maps have been generated, which identify the beginning, ending, and length of the melt season in 2003.

- The IMSI is used to identify relative melt severity across the Greenland ice sheet. Notable differences and similarities are identified in the comparison of a map of the ice facies with the IMSI.

- A time series analysis is performed on MSI and RSI images in western Greenland that suggests the line demarcating the iced-firn from bare glacial ice may be inferred using the MSI and RSI developed in this thesis.

6.2 Future Work

Because the methods used in this thesis are new, many of the aspects of the work described in this thesis warrant further investigation. Future work may be broken down into two general categories: melt model improvement and sensor fusion.

The layered melt model used in this thesis is very simple, requiring very little *a priori* information. While this model is designed to work best in percolation facies where the model best describes underlying physical processes, it is clear that improvements to the model are needed in other regions. In particular, the model needs to be modified to properly estimate melt severity in regions where the glacial ice becomes bare. Additional information about the melt process and its effects on backscatter would also be useful. While the MSI and RSI do not measure the quantity of melted snow, additional work toward estimating the melted snow volume using these indicators is warranted.

The Ku-band scatterometer sensors used in this study provide only a glimpse at the processes that affect backscatter. The SeaWinds instrument only measures backscatter at two distinct incidence angles. These two incidence angles measure the backscatter using different polarizations. This limits our knowledge of the effects of the air-snow surface on backscatter. However, if multiple sensors with broader incidence angle, different frequencies, and polarizations observations could be combined, further information about the severity and depth of the melt may be obtainable. For

example, the ERS-2 C-band scatterometer, which was also in limited operation in 2003, may be used with the tandem QuikSCAT/SeaWinds data to better infer both the liquid concentration m_v, as well as the depth of melt, due to the deeper penetration depths of C-band waves. Further information may be gained by applying the layered melt model outlined in this thesis to radiometry and using data from SSM/I and other radiometers to gain insight into the severity of Greenland melt.

Bibliography

[1] W. Krabill, W. Abdalati, E. Frederick, S. Manizade, C. Martin, J. Sonntag, R. Swift, R. Thomas, W. Wright, and J. Yungel, "Greenland ice sheet: High-elevation balance and peripheral thinning", *Science*, vol. 289, no. 5478, pp. 428–430, Jul 2000.

[2] W. Abdalati and K. Steffen, "Passive microwave-derived snow melt regions on the Greenland ice sheet", *Geophysical Research Letters*, vol. 22, no. 7, pp. 787–790, April 1995.

[3] W. Abdalati and K. Steffen, "Snowmelt on the Greenland ice sheet as derived from passive microwave satellite data", *Journal of Climate*, vol. 10, pp. 165–175, February 1997.

[4] J. F. Bolzan and K. C. Jezek, "Accumulation rate changes in central Greenland from passive microwave data", *Polar Geography*, vol. 24, no. 2, pp. 98–112, 2000.

[5] T. L. Mote, M. R. Anderson, K. C. Kuininen, and C. M. Rowe, "Passive microwave-derived spatial and temporal variations of summer melt on the Greenland ice sheet", *Annals of Glaciology*, vol. 17, pp. 233–238, 1993.

[6] D. G. Long and M. R. Drinkwater, "Greenland ice-sheet surface properties observed by the Seasat-A scatterometer at enhanced resolution", *Journal of Glaciology*, vol. 40, no. 135, pp. 213–230, 1994.

[7] M. R. Drinkwater and D. G. Long, "Seasat, ERS-1/2 and NSCAT scatterometer observed changes on the large ice sheets", in *ESA SP-424*, Noordwijk, The Netherlands, November 1998, ESA Publications Div., ESTEC, pp. 91–96.

[8] R. R. Forster, K. C. Jezek, J. Bolzan, F. Baumgartner, and S. P. Gogineni, "Relationships between radar backscatter and accumulation rates on the Greenland ice sheet", *International Journal of Remote Sensing*, vol. 20, no. 15, pp. 3131–3147, Oct. 1999.

[9] M. R. Drinkwater, D. G. Long, and A. W. Bingham, "Greenland snow accumulation estimates from satellite radar scatterometer data", *Journal of Geophysical Research*, vol. 106, no. D24, pp. 33935–33950, December 2001.

[10] V. S. Nghiem, K. Steffen, R. Kwak, and W.-Y. Tsai, "Detection of snowmelt regions on the Greenland ice sheet using diurnal backscatter change", *Journal of Glaciology*, vol. 47, no. 159, pp. 539–547, 2001.

[11] I. S. Ashcraft and D. G. Long, "Comparison of methods for melt detection over greenland using active and passive microwave measurements", *International Journal of Remote Sensing*, vol. to appear, 2006.

[12] I. S. Ashcraft and D. G. Long, "Differentiation between melt and freeze stages of the melt cycle using SSM/I channel ratios", *IEEE Trans. on Geosci. and Remote Sens.*, vol. 43, no. 6, pp. 1317–1323, 2005.

[13] V. Wismann, "Monitoring of seasonal snowmelt on Greenland with ERS scatterometer data", *IEEE Transactions on Geoscience and Remote Sensing*, vol. 38, no. 4, pp. 1821–1826, 2000.

[14] C. T. Swift, P. S. Hayes, J. S. Herd, W. L. Jones, and V. E. Delnore, "Airborne microwave measurements of the Southern Greenland ice sheet", *Journal of Geophysical Research*, vol. 90, no. B2, pp. 1983–1994, February 1985.

[15] C. S. Benson, "Stratigraphic studies in the snow and firn of the Greenland ice sheet", *SIPRE Research Report*, 1962.

[16] R. C. Bales, J. R. McConnel, E. Mosley-Thompson, and B. Csatho, "Accumulation over the Greenland ice sheet from historical and recent records", *Journal of Geophysical Research*, vol. 106, no. D24, pp. 33813–33825, December 2001.

[17] A. Ohmura and N. Reeh, "New precipitation and accumulation maps for Greenland", *Journal of Glaciology*, vol. 37, no. 125, pp. 140–148, 1991.

[18] W. Abdalati and K. Steffen, "Greenland ice sheet melt extent: 1979–1999", *Journal of Geophysical Research*, vol. 106, no. D24, pp. 33983–33988, December 2001.

[19] K. C. Partington, "Discrimination of glacier facies using multi-temporal SAR data", *Journal of Glaciology*, vol. 44, no. 146, pp. 42–53, 1998.

[20] M. Fahnestock, R. Bindschadler, R. Kwok, and K. Jezek, "Greenland ice sheet surface properties and ice dynamics from ERS-1 SAR imagery", *Science*, vol. 262, pp. 1530–1534, December 1993.

[21] K. C. Jezek, M. R. Drinkwater, J. P. Crawford, R. Bindschadler, and R. Kwok, "Analysis of synthetic aperture radar data collected over the southwestern Greenland ice sheet", *Journal of Glaciology*, vol. 39, no. 131, 1993.

[22] V. Wismann, D. P. Winebrenner, K. Boehnke, and R. J. Arhern, "Snow accumulation on Greenland estimated from ERS scatterometer data", in *Proceedings of the IEEE International Geoscience and Remote Sensing Symposium*, 1997, pp. 1823–1825.

[23] M. Joshi, *Estimation of surface melt and absorbed radiation on the Greenland ice sheet using passive microwave data*, PhD thesis, Ohio State University, 1999.

[24] T. L. Mote and M. R. Anderson, "Variations in snowpack melt on the Greenland ice sheet based on passive-microwave measurements", *Journal of Glaciology*, vol. 41, no. 137, pp. 51–60, 1995.

[25] J. D. Pack and M. A. Jensen, "A multi-channel approach to Greenland snowmelt estimation", in *Proceedings of the IEEE International Geoscience and Remote Sensing Symposium*, 2001, pp. 1789–1791.

[26] J. D. Pack and M. A. Jensen, "Greenland snowmelt estimation using multi-spectral passive and active microwave observations", in *Proceedings of the IEEE International Geoscience and Remote Sensing Symposium*, 2002, pp. 2106–2108.

[27] D. S. Early and D. G. Long, "Image reconstruction and enhanced resolution imaging from irregular samples", *IEEE Transactions on Geoscience and Remote Sensing*, vol. 39, no. 2, pp. 291–302, 2001.

[28] D. G. Long, P. J. Hardin, and P. T. Whiting, "Resolution enhancement of spaceborne scatterometer data", *IEEE Transactions on Geoscience and Remote Sensing*, vol. 31, no. 3, pp. 700–715, 1993.

[29] G. Watt and D. G. Long, "Temporal average estimate algorithm for ERS-1/2", Tech. Rep. 97-07, MERS Brigham Young University, Provo, UT, 1997.

[30] F. Ulaby, R. Moore, and A. Fung, *Microwave Remote Sensing: Active and Passive*, vol. 1, Artech House, Inc., Norwood, Massachusetts, 1981.

[31] F. Ulaby, R. Moore, and A. Fung, *Microwave Remote Sensing: Active and Passive*, vol. 2, Artech House, Inc., Norwood, Massachusetts, 1986.

[32] F. Ulaby, R. Moore, and A. Fung, *Microwave Remote Sensing: Active and Passive*, vol. 3, Artech House, Inc., Norwood, Massachusetts, 1990.

[33] C. Mätzler, "Passive microwave signatures of landscapes in winter", *Meteorology and Atmospheric Physics*, vol. 54, pp. 241–260, 1994.

[34] H. Gallée and P. Duynkerke, "Air-snow interactions and the surface energy and mass balance over the melting zone of West Greenland during GIMEX", *Journal of Geophysical Research*, vol. 102, no. 13, pp. 13,813–13,824, 1997.

[35] R. Jordan, "A one-dimensional temperature model for a snow cover: Technical documentation for SNTHERM.89", *CRREL Special Report*, , no. 91-16, 1992.

[36] F. Lefebre, H. Gallée, J.-P. van Ypersele, and W. Greuell, "Modeling of snow and ice melt at ETH Camp (West Greenland): A study of surface albedo", *Journal of Geophysical Research*, vol. 108, no. D8, 4231, doi:10.1029/2001JD001160, 2003.

[37] C. M. Rowe, K. C. Kuivinen, and R. Jordan, "Simulation of summer snowmelt on the Greenland ice sheet using a one-dimensional model", *Journal of Geophysical Research*, vol. 100, no. D8, pp. 16,265–16,273, 1995.

[38] C. S. Colbeck, "Waterflow through heterogeneous snow", *Cold Region Science Technology*, , no. 1, pp. 37–45, 1979.

[39] M. Sturm, "The thermal conductivity of seasonal snow", *Journal of Glaciology*, vol. 43, no. 143, pp. 26–41, 1997.

[40] W. Greuell and T. Konzelmann, "Numerical modelling of the energy balance and the englacial temperature of the Greenland Ice Sheet. Calculations for the ETH-Camp location (Western Greenland, 1155 m a.s.l.)", *Global Planet. Change*, vol. 9, no. (1/2), pp. 91–114, 1994.

[41] K. Steffen, J. E. Box, and W. Abdalati, "Greenland Climate Network: GC-Net", *CRREL Special Report on Glaciers, Ice sheets and Volcanoes*, vol. 96-27, pp. 98–103, 1996.

[42] J. D. Flach, K. C. Partington, C. Ruiz, E. Jeansou, and M. R. Drinkwater, "Inversion of the Surface Properties of Ice Sheets from Satellite Microwave Data", *IEEE Transactions on Geoscience and Remote Sensing*, vol. 43, no. 4, pp. 743–752, April 2005.

[43] J. B. J. Fourier, *The Analytical Theory of Heat*, Dover Publishers, New York, 1955, translated, with notes, by Alexander Freeman.

[44] M. N. O. Sadiku, *Numerical Techniques in Electromagnetics: Second Edition*, CRC Press, Boca Raton, Florida, 2001.

APPENDIX

Appendix A

Additional Model Simulation Information

This section provides additional derivation and background information used in the implementation of the geophysical model simulation conducted in Section 4.3 of this thesis.

A.1 Thermal Diffusion Derivation

Heat flux is related to the gradient of the temperature according to Fourier's Law [43],

$$\Phi_Q(\bar{\mathbf{r}}, t) = -\lambda(\bar{\mathbf{r}})\nabla T(\bar{\mathbf{r}}, t), \tag{A.1}$$

where $\lambda(\bar{\mathbf{r}})$ is the thermal conductivity, $T(\bar{\mathbf{r}}, t)$ is the temperature, t is the time, and $\bar{\mathbf{r}}$ is the position vector. The rate of change of thermal energy density, Q, at any given point is proportional to how quickly heat is flowing into or out of that point. In other words the heat density rate, $\frac{\partial Q}{\partial t}$, is proportional to the divergence of the heat flux,

$$\frac{\partial Q(\bar{\mathbf{r}}, t)}{\partial t} = \nabla \cdot \Phi_Q(\bar{\mathbf{r}}, t). \tag{A.2}$$

Since $Q(\bar{\mathbf{r}}, t) = \rho C_P T(\bar{\mathbf{r}}, t)$, where ρ is the density and C_P the specific heat, the rate of temperature change is

$$\frac{\partial T(\bar{\mathbf{r}}, t)}{\partial t} = -\frac{1}{\rho C_p}\nabla \cdot \left[\lambda(\bar{\mathbf{r}})\nabla T(\bar{\mathbf{r}}, t)\right], \tag{A.3}$$

which is the general form of the thermal diffusion equation. Reducing Equation A.3 to one-dimension,

$$\frac{\partial T(z,t)}{\partial t} = -\frac{1}{\rho(z)C_p}\frac{\partial}{\partial z}\left(\lambda(z)\frac{\partial T(z,t)}{\partial z}\right),\qquad\text{(A.4)}$$

results in Equation 4.19.

A.2   The Implicit Crank-Nicholson Method Applied to Thermal Diffusion

While using an explicit finite difference method to solve parabolic PDE's like Equations 4.19 and A.4 is possible, the solution is only stable for small time steps, similar to the hyperbolic PDE FDTD solution of the wave equation used in electromagnetic simulation [44]. Unfortunately, the time step required for the time scale of the simulation experiments used in this thesis is prohibitively small, even when the solution is smooth. A simple implicit method, the Crank-Nicholson method, employs the same finite difference equations for the explicit method, but rather than simply using a forward difference in time, performs an average of the current time step with the future time step. This results in a set of linear equations that is solved at each time step. Using this method, the solution to the thermal equation remains stable regardless of the time step size. The derivation of the set of linear equations using a variable spatial discretization step size follows.

First, the outer derivative of the thermal diffusion equation, Equations 4.19 and A.4, is moved through the parenthesis,

$$\frac{\partial T(z,t)}{\partial t} \;=\; -\frac{1}{\rho C_p}\frac{\mathrm{d}\lambda}{\mathrm{d}x}\frac{\partial T(x,t)}{\partial x} - \frac{\lambda}{\rho C_p}\frac{\partial^2 T(x,t)}{\partial x^2}. \tag{A.5}$$

To approximate $\frac{\partial^2 T}{\partial x^2}$, $\frac{\partial T}{\partial x}$ is first made discrete. The step size of the ith control volume is $\Delta x_i = x_i - x_{i-1}$. Using this, $\frac{\partial T}{\partial x}$ at $i - \frac{1}{2}$ and $i + \frac{1}{2}$ is approximately,

$$\frac{\partial T_{i-\frac{1}{2}}}{\partial x} \approx \frac{T_i - T_{i-1}}{\Delta x_{i-1}}, \tag{A.6}$$

$$\frac{\partial T_{i+\frac{1}{2}}}{\partial x} \approx \frac{T_{i+1} - T_i}{\Delta x_i}. \tag{A.7}$$

The approximate second derivative is then,

$$\frac{\partial^2 T_i}{\partial x^2} \approx \frac{\frac{\partial T_{i+\frac{1}{2}}}{\partial x} - \frac{\partial T_{i-\frac{1}{2}}}{\partial x}}{\frac{\Delta x_{i-1}+\Delta x_i}{2}} \tag{A.8}$$

$$\approx \frac{\frac{T_{i+1}-T_i}{\Delta x_i} - \frac{T_i-T_{i-1}}{\Delta x_{i-1}}}{\frac{\Delta x_{i-1}+\Delta x_i}{2}} \tag{A.9}$$

$$\approx 2\frac{\frac{\Delta x_i}{\Delta x_{i-1}+\Delta x_i}T_{i-1} - T_i + \frac{\Delta x_{i-1}}{\Delta x_{i-1}+\Delta x_i}T_{i+1}}{\Delta x_{i-1}\Delta x_i}. \tag{A.10}$$

The Crank-Nicholson method centers the time around $t^{j+\frac{1}{2}}$, thus,

$$\frac{T_i^{j+1} - T_i^j}{\Delta t} \approx \frac{(\kappa_{i+1}^j - \kappa_{i-1}^j)(T_{i+1}^j - T_{i-1}^j)}{2(\Delta x_{i-1}^j + \Delta x_i^j)^2} + \kappa_i^j \frac{\frac{\Delta x_i^j}{\Delta x_{i-1}^j + \Delta x_i^j}T_{i-1}^j - T_i^j + \frac{\Delta x_{i-1}^j}{\Delta x_{i-1}^j + \Delta x_i^j}T_{i+1}^j}{\Delta x_{i-1}^j \Delta x_i^j} +$$

$$\frac{(\kappa_{i+1}^{j+1} - \kappa_{i-1}^{j+1})(T_{i+1}^{j+1} - T_{i-1}^{j+1})}{2(\Delta x_{i-1}^j + \Delta x_i^j)^2} +$$

$$\kappa_i^{j+1} \frac{\frac{\Delta x_i^{j+1}}{\Delta x_{i-1}^{j+1} + \Delta x_i^{j+1}}T_{i-1}^{j+1} - T_i^{j+1} + \frac{\Delta x_{i-1}^{j+1}}{\Delta x_{i-1}^{j+1} + \Delta x_i^{j+1}}T_{i+1}^{j+1}}{\Delta x_{i-1}^{j+1} \Delta x_i^{j+1}}, \qquad (A.11)$$

where the superscript j denotes the time-step index and $\kappa = \frac{\lambda}{\rho C_P}$. To simplify the equations it is assumed that κ_i and Δz_i change negligibly during a single time-step, i.e., $\kappa_i^{j+1} \approx \kappa_i^j$ and $\Delta z_i^{j+1} \approx \Delta z_i^j$. While this is not strictly true, the percent change per time step is very small, and has negligible effect on the heat transfer in the simulations. The following are defined:

$$k_i^j = \frac{\kappa_i^j \Delta t}{\Delta x_{i-1}^j \Delta x_i^j} \qquad (A.12)$$

$$\alpha_i^j = k_i^j \frac{\Delta x_i^j}{\Delta x_i^j + \Delta x_{i+1}^j} - \frac{\kappa_{i+2}^j - \kappa_i^j}{2(\Delta x_{i+1}^j + \Delta x_{i+2}^j)^2} \qquad (A.13)$$

$$\beta_i^j = k_i^j \frac{\Delta x_{i+1}^j}{\Delta x_i^j + \Delta x_{i+1}^j} + \frac{\kappa_{i+2}^j - \kappa_i^j}{2(\Delta x_{i+1}^j + \Delta x_{i+2}^j)^2} \qquad (A.14)$$

$$\qquad (A.15)$$

Moving all terms containing T^{j+1} to the right side and all terms containing T^j to the left side of Equation A.11, the equation becomes,

$$-\beta_{i-1}^j T_{i-1}^{j+1} + (1 + k_{i-1}^j)T_i^{j+1} - \alpha_{i-1}^j T_{i+1}^{j+1} =$$

$$\beta_{i-1}^j T_{i-1}^j + (1 - k_{i-1}^j)T_i^j + \alpha_{i-1}^j T_{i+1}^j, \qquad (A.16)$$

which forms a basis for creating a matrix of linear equations.

The boundaries, however, must be handled differently. For the boundary at the Nth node, the temperature is held constant, which eliminates the Nth equation and makes the (N-1)th equation,

$$-\beta_{N-2}^j T_{N-2}^{j+1} + (1 + k_{N-2}^j)T_{N-1}^{j+1} = \beta_{N-2}^j T_{N-2}^j + (1 - k_{N-2}^j)T_{N-1}^j + 2\alpha_{N-2}^j T_N. \text{(A.17)}$$

The temperature at the first node is influenced by heat transfer to and from the atmosphere. The rate of heat density change at this node is approximately,

$$\frac{\partial Q(0,t)}{\partial t} \approx \frac{\Phi_{Q_{\text{in}}} - \Phi_Q(x + \Delta x_1)}{\Delta x_1}. \tag{A.18}$$

Then

$$\frac{\partial^2 T_1}{\partial x^2} \approx \frac{\frac{\Phi_{Q_{\text{in}}}\Delta x_1}{\rho_1 C_P} - \kappa_1(T_1 + T_2)}{\Delta x_1^2}. \tag{A.19}$$

Replacing Equation A.19 with Equation A.10 in Equation A.11 and neglecting the gradient of λ term results in,

$$\frac{T_1^{j+1} - T_1^j}{\Delta t} \approx \kappa_1^j \frac{\frac{\Phi_{Q_{\text{in}}}^j \Delta x_1^j}{\rho_1^j C_P} - T_1^j + T_2^j}{(\Delta x_1^j)^2} +$$
$$\kappa_1^{j+1} \frac{\frac{\Phi_{Q_{\text{in}}}^{j+1}\Delta x_1^{j+1}}{\rho_1^{j+1} C_P} - T_1^{j+1} + T_2^{j+1}}{(\Delta x_1^{j+1})^2}. \tag{A.20}$$

The assumption stated above that $\kappa_i^j \approx \kappa_i^{j+1}$ and $\Delta z_i^{j+1} \approx \Delta z_i^j$ is again used. Letting $k_0^j = \frac{\Delta t \kappa_1^j}{(\Delta x_1^j)^2}$, $\alpha_0^j = \beta_0^j = k_0^j/2$, the 1st equation in the linear system becomes,

$$(1 + \frac{k_0^j}{2})T_1^{j+1} - \alpha_0^j T_2^{j+1} = \frac{k_0^j}{\lambda_1^j}\Delta x_1^j(\Phi_{Q_{\text{in}}}^j + \Phi_{Q_{\text{in}}}^{j+1}) + (1 - \frac{k_0^j}{2})T_1^j + \alpha_0^j T_2^j. \tag{A.21}$$

The resulting matrix equation that solves for the temperatures at time $j + 1$ is then,

$$\begin{bmatrix} 1+\frac{k_0^j}{2} & -\alpha_0^j & 0 & 0 & \cdots & 0 \\ -\beta_1^j & 1+k_1^j & -\alpha_1^j & 0 & \cdots & 0 \\ 0 & -\beta_2^j & 1+k_2^j & -\alpha_2^j & \ddots & \vdots \\ \vdots & \ddots & \ddots & \ddots & \ddots & 0 \\ \vdots & & & -\beta_{N-3}^j & 1+k_{N-3}^j & -\alpha_{N-3}^j \\ 0 & \cdots & & 0 & -\beta_{N-2}^j & 1+k_{N-2}^j \end{bmatrix} \begin{bmatrix} T_1^{j+1} \\ T_2^{j+1} \\ T_3^{j+1} \\ \vdots \\ T_{N-2}^{j+1} \\ T_{N-1}^{j+1} \end{bmatrix} =$$

$$\begin{bmatrix} \frac{k_0^j}{\lambda_1^j}\Delta x_1^j(\Phi_{Q_{\text{in}}}^j + \Phi_{Q_{\text{in}}}^{j+1}) + & (1-\frac{k_0^j}{2})T_1^j & + & \alpha_0^j T_2^j \\ \beta_1^j T_1^j & + & (1-k_1^j)T_2^j & + & \alpha_1^j T_3^j \\ \beta_2^j T_2^j & + & (1-k_2^j)T_3^j & + & \alpha_2^j T_4^j \\ & & \vdots & & \\ \beta_{N-3}^j T_{N-3}^j & + (1-k_{N-3}^j)T_{N-2}^j + \alpha_{N-3}^j T_{N-2}^j \\ \beta_{N-2}^j T_{N-2}^j & + (1-k_{N-2}^j)T_{N-1}^j + 2\alpha_{N-2}^j T_N \end{bmatrix}. \tag{A.22}$$